STUDY OF TITANIUM DIOXIDE NANOPARTICLES VIA MOLECULAR DYNAMICS SIMULATIONS

By

Vishal Nitinchandra Koparde

Dissertation

Submitted to the Faculty of the

Graduate School of Vanderbilt University

in partial fulfillment of the requirements

for the degree of

DOCTOR OF PHILOSOPHY

in

Chemical Engineering

August, 2006

Nashville, Tennessee

Approved:

Professor Peter T. Cummings

Professor M. Douglas LeVan

Professor Bridget R. Rogers

Professor G. Kane Jennings

Professor Sandra J. Rosenthal

Dedicated to my mother, Mrs. Shubhangi N. Koparde,

my Father, Mr. Nitinchandra D. Koparde,

and my wife, Prajakta.

ACKNOWLEDGEMENTS

I take this opportunity to express my gratitude and special thanks to my doctoral advisor, Dr. Peter T. Cummings, whose guidance and support has been very helpful during this research. His technical expertise along with his humor and enthusiasm has made working with him extremely enjoyable and memorable. I sincerely thank all my other committee members: Dr. Douglas LeVan, Dr. Bridger Rogers, Dr. Kane Jennings and Dr. Sandra Rosenthal for their support. I would like to thank Dr. Pavanandan Naicker and Dr. Jose Rivera-Rojas for their helpful conversation during the early stages of my doctoral work. I thank the current and past members of the Cummings Research Group that I may have interacted with. I thank the Chemical Engineering Department staff for all their help during my stay at the Vanderbilt University.

Most of all, I thank my parents for always encouraging me to pursue my dreams. I would like to thank my wife, Prajakta, for believing in me and filling my life with love and joy. I would also like to thank all my friends who have always been there for me and helped me get through tough times.

Finally, last but not the least, I would like to acknowledge the financial support from National Science Foundation and the following computational centers for computer time:

(a) National Energy Research Scientific Computer Center
(b) Center of Computational Sciences – Oak Ridge National Laboratory
(c) Advanced Computing Center for Research and Education – Vanderbilt University.

TABLE OF CONTENTS

Page

Chapter

Appendix

LIST OF FIGURES

Page

LIST OF TABLES

CHAPTER I

INTRODUCTION

Interest in the physics of condensed matter, which is at size scales larger than individual atoms or molecules but much smaller than bulk matter, has developed rapidly in the past three decades (Franks 1987; Dewdney 1988; Siegel 1993; Oakley and Hanna 2004). It is out of this interest that the terms of “nanoscience” and “nanotechnology” have emerged. Nanoscience and nanotechnology are defined as the sciences and technologies where dimensions and tolerances in the range of 0.1 to 100 nm play a critical role. The fact that controlling the size of matter in the nanometer range could considerably alter its physical and chemical properties when compared with bulk has been the impetus behind this curiosity. For example, the mechanical, thermal, electrical and magnetic properties of ceramics, sintered materials and composites are greatly enhanced by reducing the grain size. Other properties like strength, ductile-brittle transition, transparency, dielectric constant and permeability can also be enhanced by direct size reduction (Franks 1987).

Due to the novel and enhanced properties of nanosized materials they are quickly finding many applications in medicine (Sahoo and Labhasetwar 2003; Silva 2004), electrochemistry (Gooding 2005), electronics (Tsukagoshi, Yoneya et al. 2002) and aerospace (Laurvick and Singaraju 2003). The use of small biodegradable nanoparticles have completely changed the science of drug delivery, with more specificity and sustained drug release over days or even weeks. The discovery of single and multi-walled carbon nanotubes has been a boon to the field of electronics, where their small size, high chemical and thermal stability, high elasticity, high tensile strength and high conductivity have been largely exploited in applications, such as sensing, high speed communications and in making nanodevices like the carbon nanotube field-effect transistor.

Nanoparticles are found almost everywhere around us. Nano-size carbon black particles have been used as reinforcing additive in tires for about 100 years. Various vaccines often consist of proteins with nanoscale dimensions. Sensors for modern computer disks are made from layered inorganic materials with nanometer thickness. Nanomaterials are added to cloth in order to contribute to stain resistance. Cosmetics contain zinc oxide and TiO_2 nanoparticles as sunscreens. PPG has introduced "self-cleaning" window glass products, that have a surface layer of TiO_2 nanoparticles. Nanoscale bits of clay are added to reinforced plastics used in cars manufactured by GM. Ceramic nanoparticles with entrapped biomolecules have potential applications in drug delivery.

Thus, the applications of nanoparticles are almost unlimited. In the work described here, titanium dioxide nanoparticles, which have numerous applications in optics, sensing and as photocatalysts, are studied. The fact that these nanoparticles are extremely small and have only a few hundred to a few thousand atoms (ions) makes molecular dynamics simulations a strong candidate for studying them.

I.1 Titanium Dioxide

Titanium dioxide or titania (TiO_2) is a widely occurring transition metal-oxide semiconductor used in science and technology. Due to its opacity, it has been used over the years as a while pigment in paints (Reck and Seymour 2003) and paper (Dutt, Upadhyaya et al. 2002). However, nowadays nanosized titania is broadly used as a raw material in electronics and structural ceramics. It is used in dye-sensitized solar cells and in high temperature separation and photocatalytic applications (Ohtani, Okugawa et al. 1987; Augugliaro, Loddo et al. 1995; Martin, Lee et al. 1995). Recently, nano-titania has been used as a catalyst in many different heterogeneous reactions under ultraviolet light, such as alcohol dehydration (Fox and Dulay 1993), degradation of paint pigments (Hotsenpiller, Bolt et al. 1998), oxidation of aromatic compounds (Fujihira, Satoh et al. 1981), nitrogen oxide reduction (Gruy and Pijolat 1992) and removal of toxic contaminants from wastewater (Ohtani, Okugawa et al. 1987; Martin, Lee et al. 1995). Tetrafluorobenzoic acid modified TiO_2 nanoparticles are used as lubricant additives to improve the tribological properties of the base oil (Ye, Cheng et al. 2003).

I.1.1 Crystal Structure

It has been reported in the literature that titanium dioxide occurs in eleven different polymorphs with distinct structures (Swamy, Gale et al. 2001). Anatase, rutile and brookite are the three polymorphs that are abundantly found in nature (Banfield and Veblen 1992; Gribb and Banfield 1997; Penn and Banfield 1998). Recently, TiO_2 (B) has been added as the fourth naturally occurring TiO_2 polymorph found at very low pressures (Banfield, Veblen et al. 1991). In all polymorphs of TiO_2, titanium is in octahedral coordination, i.e., its coordination number equals six. However, the number of shared edges increases from two in rutile, to three in brookite, to four in anatase. It has been suggested (Evans 1966) that the relative stability in the bulk phase of these phases may be inversely related to the number of shared edges, i.e., rutile more stable than brookite, which in turn is more stable than anatase. The structure of anatase and rutile is tetragonal, while that of brookite is orthorhombic (Banfield, Veblen et al. 1991), and they belong to the *I41/amd, P42/mnm* and *Pbca* space groups, respectively (Kim, Enomoto et al. 1996). Their lattice parameters, a, b and c, are reported in Table I.1 (Bokhimi, Morales et al. 2001).

Table I.1 Crystal structure, lattice parameters (a,b and c) and number of atoms per cell (Z) for various TiO_2 polymorphs.

Phase	***Space group***	***A (Å)***	***B (Å)***	***c (Å)***	***Z***
Anatase	I41/amd	3.785		9.514	4
Rutile	P42/mnm	4.593		2.959	2
Brookite	Pbca	9.182	5.456	5.143	8

In the bulk form, rutile is the most stable polymorph of titania under ambient conditions, while anatase, brookite and TiO_2 (B) are considered to be metastable as they irreversibly transform to rutile upon heating (Banfield, Veblen et al. 1991; Kobata, Kusakabe et al. 1991; Zhang and Banfield 1998; Ovenstone 2001; Barnard, Zapol et al. 2005). The stability criterion has been found to be highly dependent on the particle size and temperature. It is found that the synthesis of nanocrystalline TiO_2 consistently resulted in anatase nanoparticles, which transformed to rutile upon reaching certain particle size. This implies that transition energetics are closely related to particle size and that anatase is the more stable form at the nanoscale (Barnard, Zapol et al. 2005).

I.1.2 Manufacture of nano-TiO_2

Nanosized titania is usually manufactured either by the "dry" process or by the "wet" process. In the dry process, which is also referred to as the "chloride" process vapor phase oxidation of $TiCl_4$ is carried out to produce titania (Akhtar, Yun et al. 1991; Kobata, Kusakabe et al. 1991; Pratsinis 1998-a; Pratsinis and Spicer 1998-b; Stark and Pratsinis 2002). About three million tons of TiO_2 is produced annually via this process (Pratsinis 1998-a). The temperatures in the dry process range from 973 to 1873 K. It is generally carried out in a flame reactor. The reaction involved can be represented as,

$$TiCl_4(g) + O_2(g) \rightarrow TiO_2(s) + 2Cl_2(g) \tag{I.1}$$

In the commercial process, water vapor is present in the flame reactor from the combustion of hydrocarbon gas for the flame and it plays a vital role in controlling the crystallinity and the particle size of the produced powders (Jang 1997). The temperature of the flame reactor is also an important parameter in controlling the particle size. A typical titania synthesis flame is shown in Figure I.1 (Stark and Pratsinis 2002). It has been reported that smaller particles can be obtained by running the flame reactor at higher temperatures (Jang and Jeong 1995).

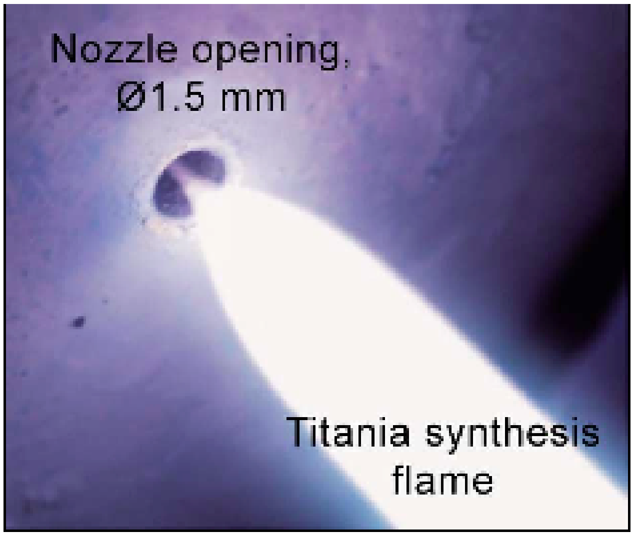

Figure I.1 Typical titania dry synthesis flame.

During the thermal annealing phase of the flame synthesis of titania, particles collide with each other leading to sintering of the formed particles. If the sintering time is greater than the time interval between consecutive collisions then larger particles are formed, otherwise large agglomerates are generated (Lehtinen and Zachariah 2002). It is important to understand the mechanism of particle sintering and the rate at which it occurs in order to successfully predict the size and phase distribution of the resultant powders.

There are two main routes for the wet syntheses (Cheng, Ma et al. 1995; Wu, Long et al. 1999; Yang, Mei et al. 2000; Yang, Mei et al. 2001; Yang, Mei et al. 2001; Yang, Mei et al. 2002; Yin, Li et al. 2002) of nano-TiO_2, namely hydrolyzation of titanium alkoxides and hydrolysis of titanium tetrachloride or titanium trichloride (Sun, Gao et al. 2003; Sun, Gao et al. 2003). This is generally a sol-gel process carried out at high temperature and pressure. The size and phase of the particles formed is greatly influenced by the solvent and the stabilizing agent used (Trung, Cho et al. 2003). The solvent used in the wet syntheses is generally hydrothermal water and the particle phase and size are relatively harder to control when compared with the dry process. Also, the dry process is solvent free and produces fewer by-products.

I.2 Overview of Dissertation

In this dissertation, we report the studies of TiO_2 nanoparticles carried out using molecular dynamics simulations. We begin by introducing the molecular dynamics simulation technique in Chapter II. Then in Chapters III and IV, we apply this methodology first to individual TiO_2 nanoparticles and then to a system of two like-phased nanoparticles undergoing sintering. The phenomenon of melting point depression is also studied using molecular dynamics technique. We find that the initial stages of sintering are very rapid and occur within the first ~50ps of the simulation. The relative orientation of the particles and the dipole-dipole interaction between the particles play a very important role in the sintering process.

Since, as noted earlier, one method of producing TiO_2 involves hydrothermal synthesis, we perform simulations of anatase and rutile nanoparticles in ambient and hydrothermal aqueous environments, and examine the structure of water in the vicinity of the nanoparticles. These simulations are reported in Chapter V. Then, in Chapter VI, we study phase transformations that take place when two or more TiO_2 nanoparticles with different structures come in contact during sintering using molecular dynamics simulations. We find that generally no phase transformations are observed at temperatures lower than the melting points. At temperatures in the vicinity of the melting points, nanoparticles we find that the nanoparticles adopt the structure that is the more stable of the nanoparticles. Finally, in Chapter VII we summarize our findings and discuss the prospects for future work.

CHAPTER II

SIMULATION METHODOLOGY

II.1 Background

Molecular dynamics simulation is one of a number of techniques falling under the road title of molecular modeling[Westmoreland, 2002 #164]. Molecular dynamics involves the numerical solution of Newton's equations of motion on an atomistic or molecular scale to obtain information about the systems time-dependent properties. In its early days, the method of molecular dynamics gained popularity in the field of materials science. But since the 1970s, molecular dynamics has also been successfully used in chemistry, biochemistry, biophysics and many engineering disciplines. For example, in biochemistry, molecular dynamics serves as an important tool for determining protein structure and refining it. In physics, molecular dynamics is used to study atomic-level phenomenon such as thin film growth, which cannot be observed directly. It is also used to examine the physical properties of nanostructured hard and soft materials, often before they have been synthesized.

The extent of the success of the molecular dynamics technique is subject to the availability of computational power. The size of the simulation system and the time of simulation should be selected such that the calculation is completed within a reasonable time period. The timestep of the simulation should be chosen small enough to avoid any numerical errors associated with integrating the equations of motion, and the number of timesteps, that is, the total simulation time, should be chosen large enough to capture the phenomenon begin modeled. The simulated system is sometimes replicated in one or more of the three coordinate directions in order to model an infinite medium. This is referred to as periodic boundary condition. When periodic boundary conditions are applied, care should be taken to choose a large enough simulation box size to avoid interaction between a species in the simulation box and its image in the neighboring box.

II.2 Newton's equations of motion

For every molecule i considered, Cartesian coordinates $\bar{r}_i$ and momenta $\bar{p}_i$ are computed over time and can then be used to calculate various thermodynamic and transport data by applying statistical mechanics methods.

In molecular dynamics simulations we assume that the molecules move according to the Newton's equations of motion, given by

$$\frac{d\bar{r}_i}{dt} = \frac{\bar{p}_i}{m_i} \tag{II.1}$$

$$\frac{d\bar{p}_i}{dt} = \bar{F}_i \tag{II.2}$$

where m_i and $\bar{F}_i$ are the mass and the force experienced by the molecule i, respectively. The force can also be expressed as

$$\bar{F}_i = -\frac{\partial U}{\partial \bar{r}_i} \tag{II.3}$$

U represents the potential energy and is given by the sum of all intra and intermolecular interactions. The interaction energy between molecules is usually defined semi-empirically by forcefields also known as interaction potentials. The forcefields are modeled by using data from experiments and other *ab initio* methods.

I.2.1 Forcefield for TiO_2

In this work, we need to model the interactions between Ti and O ions. When choosing a model to describe atomic interactions, we should consider the attractiveness of conceptual and computational simplicity. At the same time, it is vital that the potential model is reliable in terms of its transferability across various polymorphic phases of the material under consideration. An interatomic potential that not only reproduces the crystallographic structures of the polymorphs, but also various physical properties across a range of conditions is generally preferred for atomistic simulations. A survey of the recent literature shows that several forcefields have been published for TiO_2 (Catlow and James 1982; Sawatari, Iguchi et al. 1982; Catlow, Freeman et al. 1985; Mostoller and Wang 1985; Post and Burnham 1986; Matsui and Akaogi 1991; Kim, Enomoto et al. 1996; Oliver, Watson et al. 1997; Roux and Glasser 1997; Swamy and Gale 2000) Collins and coworkers (Collins and Smith 1996-b) have carried out a detailed in-depth assessment of nine forcefields for TiO_2. Their report concludes that the forcefield developed by Matsui and Akaogi (Matsui and Akaogi 1991) is the most suitable of the available forcefields for use in classical molecular dynamics simulations of bulk titania. The Matsui-Akaogi forcefield has been shown to give results comparable to a more complex and computationally demanding variable charge forcefield (Swamy and Gale 2000) for TiO_2. The Matsui-Akaogi forcefield (Matsui and Akaogi 1991) also predicts within acceptable limits the lattice energies, elastic constants, dielectric constant of rutile and the relative surface energies of rutile (100), (110) and (001) surfaces. It has been reported that the structures of TiO_2 polymorphs and their relative bulk stabilities predicted by the Matsui-Akaogi forcefield are within experimental limits when compared with the limited experimental data (Collins, Smith et al. 1996-a; Collins and Smith 1996-b; Collins, Smith et al. 1997). Clearly, surface effects are extremely important when studying nanoparticles. Bandura and Kubicki (Bandura and Kubicki 2003) have verified the suitability of using Matsui-Akaogi forcefield to study rutile surfaces, using various quantum mechanical methods. Hence, the Matsui-Akaogi forcefield has been used to model TiO_2 nanoparticles in this work. In this forcefield, the interactions between the Ti and O ions can be represented as

$$U_{ij}(r) = A_{ij} \exp\left(-\frac{r}{\rho_{ij}}\right) - \frac{C_{ij}}{r^6} + \frac{q_i q_j}{r} \qquad \text{(II.5)}$$

where U_{ij} is the interaction energy between sites *i* and *j*, *r* is the distance between them and the parameters A_{ij}, ρ_{ij} and C_{ij} are listed in Table II.1. The Matsui-Akaogi forcefield (Matsui and Akaogi 1991) represents the ions as rigid spheres with partial ionic charges, *q*'s, of +2.196 and -1.098 for titanium and oxygen, respectively.

Table II.2 Matsui-Akaogi forcefield parameters

Ion	***Q***	***A***	***B***	***C***
Ti	+2.196	1.1823	0.077	22.5
O	-1.098	1.6339	0.117	54.0

All the molecular dynamics simulations reported in this research work have been carried out using the Daresbury Laboratory molecular dynamics code, DL_POLY version 2.13 (Smith 1987; Smith and Forester 1996). DL_POLY uses Verlet's leapfrog algorithm (Allen and Tildesley 1997) in conjunction with multiple timestep method, to integrate Newton's laws of motion over time. The details about the simulations are described in the subsequent chapters.

The following aspects of TiO_2 nanoparticles have been studied in this work from atomistic point of view using molecular dynamics simulations as an analysis tool:

(a) Nanoparticle sintering (Chapters III and IV)

(b) Water adsorption on nanoparticle surface (Chapter V)

(c) Phase transformations during nanoparticle sintering (Chapter VI).

CHAPTER III

SINTERING OF TiO_2 NANOPARTICLES

III.1 Introduction

Sintering has been defined (German 1996) as “a thermal treatment for bonding particles into a coherent, predominantly solid structure via mass transport events that often occur at the atomic scale”. The process of sintering has been around for thousands of years (German 1996). Even today sintering is a primary operation in the production processes of most ceramics, for example: refractories, bricks, abrasives, porcelain and various other construction materials. When particles are heated together at relatively high temperatures, they typically sinter to bond together. These high temperatures generally range from one half the melting point to just below the melting point of the solid under consideration. It should be noted that the melting point of small particles can be considerably lower than bulk owing to “melting point depression”, which is addressed in greater detail in the next chapter. Sintering lowers the surface energy by reducing the surface area via formations of new bonds. The bonds are formed by various mechanisms occurring at the atomic level. In ceramics, sintering is accompanied by an increase in compact density as the particles attract each other and self-compress to eliminate pores. This compaction or densification is sometimes linked to the beginning of phase transformation (Kumar, Keizer et al. 1992; Yang, Yang et al. 1998; Boskovic, Kosanovic et al. 2001). Sintering particles tend to possess an inherent driving force for mass flow and this driving force increases as the particle size decreases. The sintering stress is higher for smaller particles due to larger surface area and the atomic mobility increases with temperature.

One characteristic of sintering has been that the sintering theory has always been far behind sintering practice (German 1996). Theories trying to explain the fundamentals of sintering phenomena first emerged in the late 1940s. Most of these theories are developed for larger particles and their applicability to smaller particles in the nanometer range is doubtful. Recently, due to the abundant use of submicron particles, questions regarding the nature of their growth kinetics and morphology have been of great concern (Zachariah, Carrier et al. 1996; Zachariah and Carrier 1999). It has been shown that nanoparticles cannot be treated as continuum elastic bodies, which is one of the major assumptions made in majority of the sintering theories. The fact that the nanoparticles comprise of individual atoms is extremely important (Preining 1998). Therefore, the process of nanoparticle sintering is an ideal candidate to be studied from atomic point of view using tools like molecular dynamics simulations.

There are believed to be six different mechanisms (Zeng, Zajac et al. 1998) contributing toward the sintering of larger particles, namely, (1) surface diffusion, (2) lattice diffusion from surface, (3) vapor transport, (4) grain boundary diffusion, (5) lattice diffusion from grain boundary and (6) lattice diffusion through dislocations. However, in smaller particles the sintering mechanism is radically different due to the presence of high surface curvature and the atomic forces becoming more significant. In the case of copper and gold nanoparticles (Zeng, Zajac et al. 1998), only two classical mechanisms are responsible for mass transport during the initial stages of sintering are surface diffusion and grain boundary diffusion. The other mechanisms that play a major role in the early sintering stages of metal nanoparticle sintering are (a) mechanical rotation, (b) plastic deformation due to dislocation generation and transmission, and (c) amorphisation of sub-critical grains (Zeng, Zajac et al. 1998).

In this chapter, the results obtained from molecular dynamics simulations of the initial stages of TiO_2 nanoparticle sintering are reported. As mentioned in Chapter I, TiO_2 nanoparticles are manufactured in flame reactors where inter-particle collisions lead to particle sintering. The final particle size and phase distribution dictate the overall properties of the TiO_2 powder, for example, its photocatalytic activity. Hence, a careful study of the sintering mechanism is needed to predict the final particle size and phase distribution with considerable accuracy. The motivation behind this work is to achieve a better understanding of the phenomenology and specifics of the sintering process of TiO_2 nanoparticles with the help of molecular dynamics simulations, by employing the Matsui-Akaogi forcefield (See section II.2 for details).

The driving force for the sintering of two TiO_2 nanoparticles is the decrease in the free energy due to a reduction in the surface area (Lehtinen and Zachariah 2001). Solid-state diffusion within the particle, which is due to the stress gradients generated by non-sphericity, is believed to be the controlling mechanism (Friedlander and Wu 1994). The resultant larger particle or agglomerate will have lower potential energy, and due to conservation of energy in an isolated system, a higher temperature (Lehtinen and Zachariah 2002). The temperature rise can also be explained by the formation of new chemical bonds between the particles after collision (Gay and Berne 1986; Lehtinen and Zachariah 2002). Since TiO_2 nanoparticles coalesce by virtue of solid-state diffusion, which is extremely sensitive to temperature (Lehtinen and Zachariah 2001), one can expect that temperature will play a critical role in the process of nanoparticle sintering. Earlier studies on silica nanoparticle sintering showed almost instantaneous coalescence at higher temperatures (Koch and Friedlander 1990) and fractal-like agglomerate formation at lower temperatures (Lehtinen and Zachariah 2002). It was also found that the heat release due to particle coalescence may reduce the coalescence time by as much as a few orders of magnitude in the case of silicon nanoparticles.

There have been many models attempting to explain the dynamics of coalescence of particles. Koch and Friedlander (Koch and Friedlander 1990; Lehtinen, Windeler et al. 1996) assumed that the rate of coalescence was directly related to the excess surface area of colliding particles. This simple linear decay law for the agglomerate surface area (Friedlander and Wu 1994), when combined with the aerosol general dynamics equation (Akhtar, Yun et al. 1991), has produced several successful models for particle size prediction. These models break down when the particle size goes down to a few nanometers. It was suggested that the high internal pressure of smaller particles could be responsible for the inapplicability of the models to smaller particles. For example, the pressure inside a 10 nm TiO_2 particle is reported to be around 2000 atmospheres (Ding and Liu 1997; Ehrman, Friedlander et al. 1998) and it increases with decreasing size. Such high internal pressures affect the diffusion coefficients, which in turn affect the rates of particle sintering (Ehrman, Friedlander et al. 1998; Schweigert, Lehtinen et al. 2002). Thus, atomistic studies of nanoparticles can shed light on the fundamental mechanisms of nanoparticle sintering, thereby providing valuable insights and guidance to experimental work (Zhu and Averback 1995; Zeng, Zajac et al. 1998). To date, very few simulation studies have actually probed the sintering of metal-oxide nanoparticles.

Zhu and Averback (Zhu and Averback 1995; Zhu and Averback 1996-a; Zhu and Averback 1996-b) carried out molecular dynamics simulations of sintering copper nanoparticles and nanocylinders, while Raut and coworkers (Raut, Bhagat et al. 1998) reported studies of sintering aluminum nanoparticles. Similar studies of sintering nickel particles have been carried out by Heinisch (Heinisch 1996). A few other simulation studies have examined ceramic sintering systems such as silicon clusters, silicon nitride and simple two-dimensional Lennard-Jones systems (Tsuruta, Omeltchenko et al. 1996; Zachariah, Carrier et al. 1996). All of these studies report a rise in temperature upon nanoparticle sintering. Zhu and Averback (Zhu and Averback 1996-a) concluded that copper nanoparticle sintering occurred via plastic deformation, while Raut *et.al. (Raut, Bhagat et al. 1998)* proved that aluminum nanoparticles do not sinter via plastic deformation. On the other hand, Heinisch (Heinisch 1996) and Tsuruta *et.al. (Tsuruta, Omeltchenko et al. 1996)* showed that sintering is driven by surface diffusion. Although it is possible that different systems, i.e., metals and ceramics, may have different dominant mechanisms of mass transport, the exact mechanism of nanoparticle sintering is still debatable. Further, the dependence of the sintering mechanism on particle size has not been rigorously investigated. Since the kinetics of particle sintering are related to grain growth kinetics, it is important to study the effect of particle size on sintering.

In the work presented here, the initial stages of TiO_2 sintering and the effect of size, crystallographic orientation and temperature on the sintering process are investigated. As anatase and rutile polymorphs of TiO_2 have the largest number of industrial applications, we have considered only 3 nm and 4 nm anatase and rutile in the simulations reported here. Each system contains two nanoparticles of the same phase.

Multiphase nanoparticle sintering is addressed in Chapter V. The effect of orientation on the sintering process is investigated by rotating one of particles in the system, while keeping the other unchanged. The relative mobilities of ions in the neck and core regions of the sintering nanoparticles are also reported.

III.2 Simulation Details

III.2.1 Forcefield Selection

The Matsui-Akaogi forcefield (Matsui and Akaogi 1991) has been selected to describe the interactions between Ti and O ions. The details and advantages of this forcefield over the other reported forcefields for TiO_2 have been listed in section I.2. The forcefield parameters are listed in Table II.2. The Daresbury laboratory molecular dynamics simulation code, DL_POLY version 2.13 (Smith 1987; Smith and Forester 1996), has been used to perform all the simulations on a parallel architecture (see section II.2).

III.2.2 Simulation Method

To generate the nanoparticles, a sphere of the desired diameter is cut out of a larger lattice, which is constructed using the lattice parameters (Abrahams and Bernstein 1971; Bokhimi, Morales et al. 2001) for anatase and rutile. These lattice parameters are listed in Table I.1. Excess titanium ions or oxygen ions are removed from the surface to obtain charge balance and ensure neutrality. The 3 nm particles of anatase and rutile particles thus obtained, contain 417 and 491 TiO_2 units, respectively. Initially, molecular dynamics simulation in canonical ensemble is performed to obtain a nanoparticle at the desired temperature. In canonical ensemble, the number of atoms in the system (N), volume of the system (V) and the system temperature (T) are held constant. Hence, molecular dynamics simulations in the canonical ensemble are also commonly referred to as NVT simulations. Figure III.1 shows snapshots of a 3 nm rutile nanoparticle before and after equilibration to the desired temperature of 1473 K. Then, to generate the initial configuration for the sintering simulation of same phase nanoparticles, the sphere is replicated and translated along the X-axis, so that the distance between the surfaces of the replicas is 1 nm. Sintering simulations are carried out in micro-canonical ensemble using 0.5fs timestep and no periodic boundary conditions are applied to ensure simulation of isolated nanoparicles. In microcanonical ensemble, the number of atoms in the system (N), volume of the system (V) and the total system energy (E) are held constant, simultaneously. Hence, these molecular dynamics simulations are also called NVE simulations. This is the best way to mimic the low-pressure conditions prevailing in the flame reactors of the chloride process. The cutoff is chosen such that all the ions in the system are included in force and energy calculations. Simulations were carried out for a total time of about 0.5 to 1ns. This time is extremely small to study the entire process of TiO_2 nanoparticle sintering but is long enough to study the important initial stages of sintering. Furthermore the potential energy reaches a plateau by this time indicating that the system is entering a quasi-steady state. Kobata et. al. (Kobata, Kusakabe et al. 1991) suggest that the characteristic sintering time for 3 nm TiO_2 sintering at 1473 K is about 12 μs, which is too long for a molecular dynamics simulation. In this work, various simulations with different starting temperatures, namely 573 K, 973 K and 1473 K, are carried out for 1ns each to investigate the dependence of temperature, as in the flame synthesis process there are different regions in the flame, representing different temperature zones, and the simulations are repeated for 3 nm and 4 nm particle because in the synthesis process particles of different sizes sinter and the effect of size is bound to be significant to the overall sintering process.

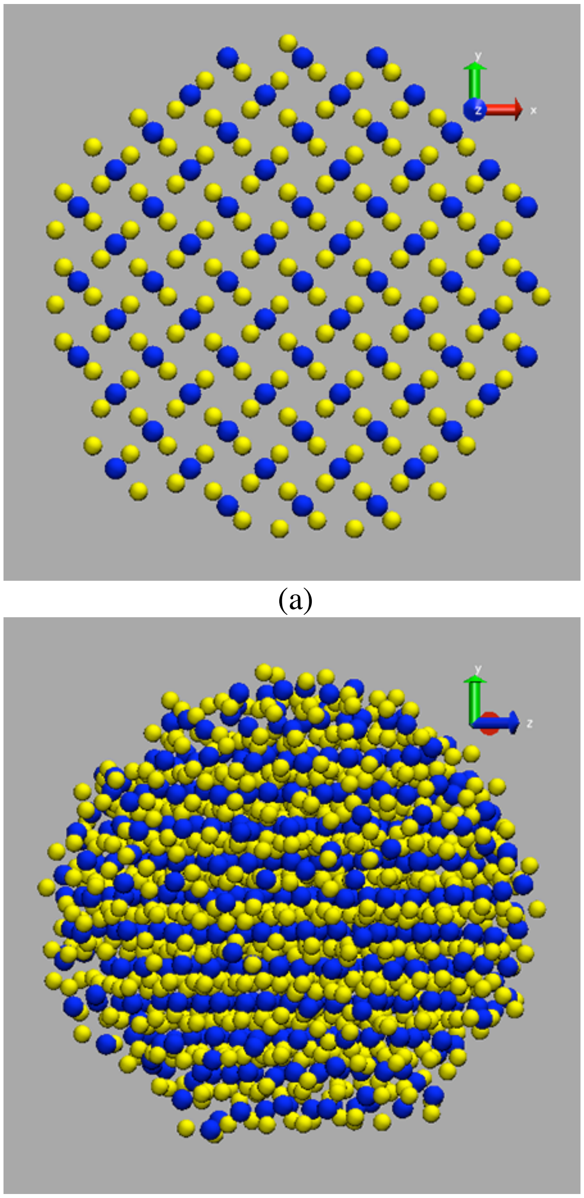

(a)

(b)

Figure III.1 Snapshots of 3 nm rutile nanoparticle (a) Before equilibration and (b) After equilibration at 1473 K. Note the different orientations in (a) and (b).

III.3 Results and Discussion

III.3.1 Characterization of TiO_2 nanoparticles

Simulated X-ray diffraction patterns of equilibrated 3 nm TiO_2 particles where determined. These are shown in Figure III.2. Anatase (101) peaks are observed at 25.5°. The peak height tends to decrease with increase in temperature. This suggests that as the temperature is increased the crystallinity is lost due to higher kinetic energy of the ions. There are two dominant peaks at 27.5° and 55° in the rutile particle X-ray patterns, namely, rutile (110) and (220), respectively. A similar decrease in the height of (220) peaks with temperature is observed indicating loss of crystallinity with temperature rise. The procedure of obtaining simulated X-ray diffraction patterns is explained in Appendix A.

The coordination number of Ti ions along the radius of the nanoparticle is shown in Figure III.3. The coordination number of Ti ions equals six in the core of the particle but as we move towards the surface of the nanoparticle it drops to four. This indicates that the ions rearrange themselves in the outer ~4 Å making it amorphous. The outer layer where the Ti-coordination is less than six is henceforth referred to as the "rough surface" or the "amorphous surface" layer.

Table III.1 shows the percentages of Ti coordination numbers for 3 nm anatase and rutile nanoparticles at 573 K, 973 K and 1473 K. The percentage of 3, 4, 5 and 7 coordinated Ti ions increases with increasing temperature for both anatase and rutile particles quantifying the loss of crystallinity. As all the Ti ions with coordination number not equal to six are in the amorphous surface layer, the table indicates that about 35% to

45% of the total Ti ions in the nanoparticle are in the surface layer. The table also shows that the percentage of 6-coordinated Ti ions is always greater in rutile than anatase at any given temperature, indicating that rutile particles have a smaller amorphous surface layer compared to anatase. This can also be seen by careful examination of Figure III.3.

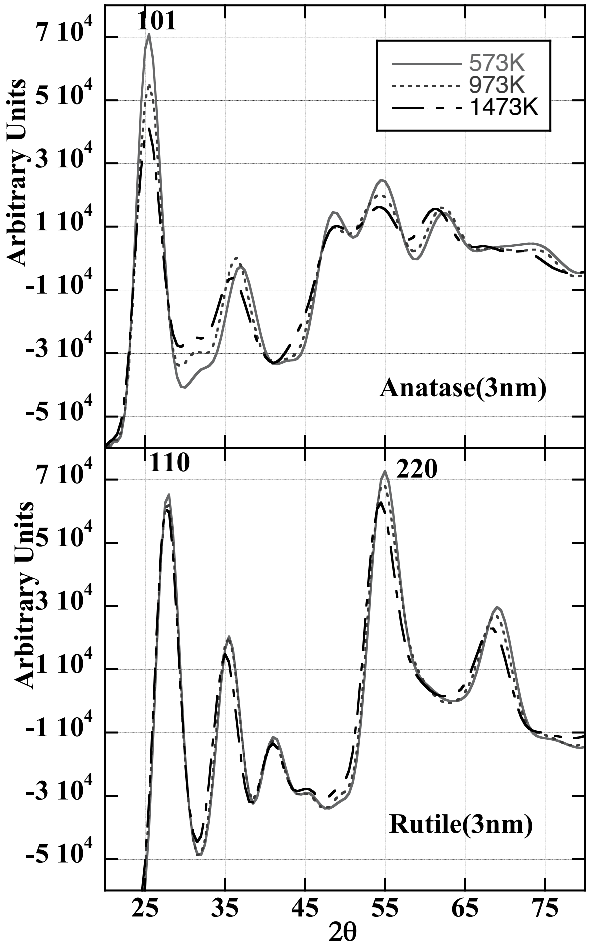

Figure III.2 Simulated XRD patterns of 3 nm TiO_2 nanoparticles at 573 K, 973 K and 1473 K.

Table III.1 Percentages of Ti ion coordination number at various temperatures for 3 nm anatase and rutile particles.

Coordination Number	***Anatase (573 K)***	***Anatase (973 K)***	***Anatase (1473 K)***	***Rutile (573 K)***	***Rutile (973 K)***	***Rutile (1473 K)***
3	0.01	0.02	0.08	0.01	0.01	0.07
4	10.09	11.62	12.13	8.88	9.44	10.37
5	27.41	27.86	31.23	25.36	26.78	27.28
6	61.60	59.57	55.09	65.48	63.40	61.83
7	0.89	0.93	1.46	0.27	0.37	0.45

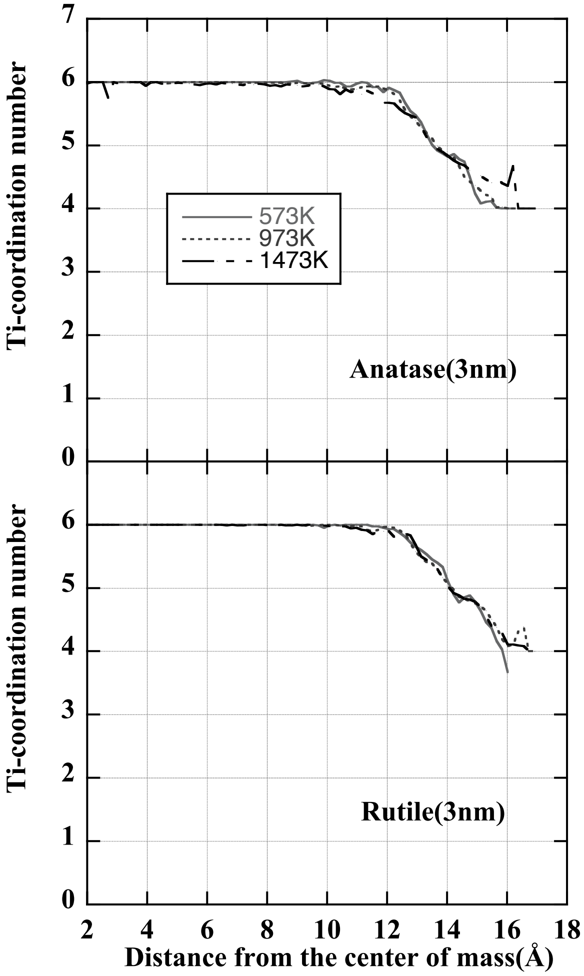

Figure III.3 Ti coordination number along the radius of 3 nm anatase and rutile particles.

III.3.2 Sintering Simulations

Figure III.4 shows snapshots of a typical sintering simulation. The simulation involves two 3 nm anatase nanoparticles with a starting temperature of 573 K. The simulation begins as shown in Figure III.4 (a) where the identical nanoparticles are separated by 1 nm, or, in other words, the center-to-center distance between the 3 nm anatase nanoparticles is about 4 nm. It is observed, as in Figure III.4 (b), that the nanoparticles are mutually attracted towards each other. It should be noted that no external force is applied on any of the nanoparticles throughout the simulation. There is visual evidence of surface distortion, or increase in surface roughness, as the particles come into close proximity. The collision takes place in about 20-25ps without any rebounding or fracturing. This is depicted in Figure III.4 (c). A neck formation follows the collision, which quickly grows to a diameter of about 1.6 nm. A gradual broadening of the neck is observed in the period that follows to reach a final agglomerated state indicated in Figure III.4 (d) with a neck diameter of about 1.75 nm. The simulation is continued for a total time of about 0.5ns and complete fusion of the two anatase nanoparticles is not observed over the course of simulation, although we expect the formation of a larger spherical nanoparticle if the simulations were permitted to run for a very long time. Simulated X-ray diffraction patterns (see Appendix A) suggested that there is no phase transformation during the entire simulation.

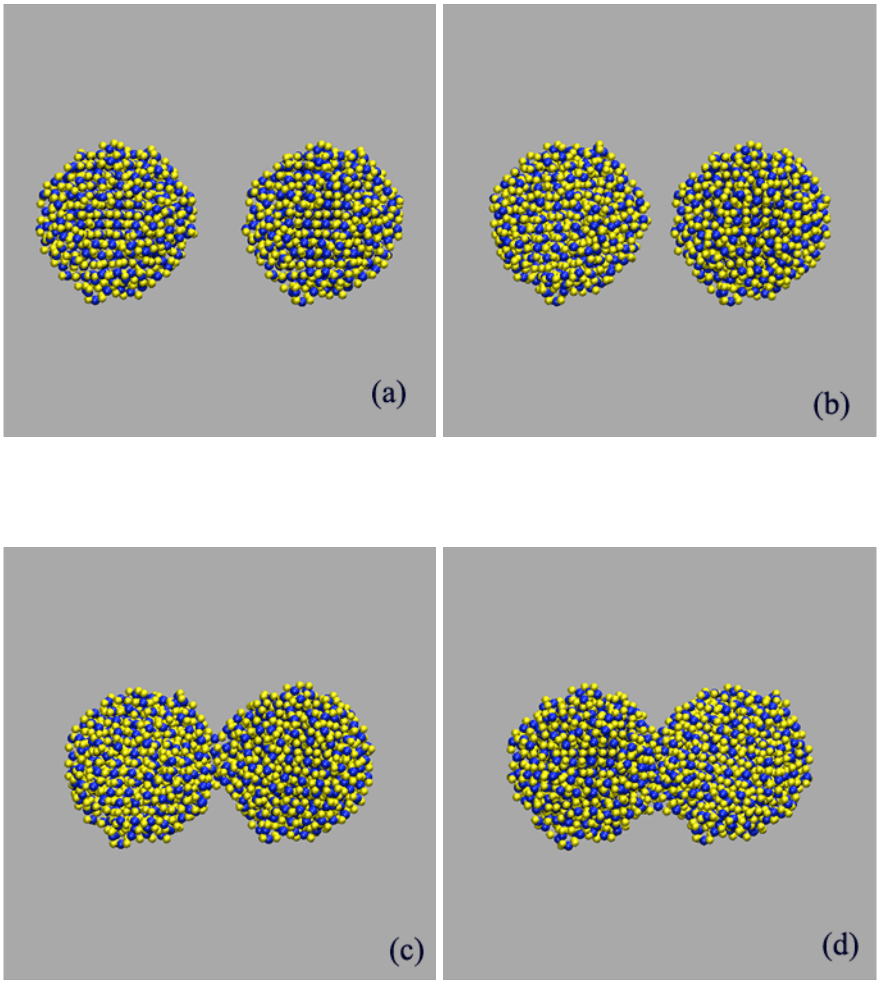

Figure III.4 Snapshots of a typical sintering simulation

Figures III.5 and III.6 show the temperature and configurational energy profiles with various initial temperatures for 3 nm anatase sintering and 3 nm rutile sintering, respectively. In all the cases, a drop in the configurational energy occurs when the two nanoparticles touch each other for the first time, and is caused by the new low potential energy pairs created when ions from each nanoparticle come in proximity of each other. It is observed that there is a rapid increase in temperature immediately after the nanoparticles come in contact with each other. As the nanoparticles form a neck, their cumulative surface area decreases, thereby decreasing their overall potential energy. Since, the total energy of an isolated adiabatic system must be conserved, the kinetic energy goes up accordingly increasing the temperature of the system. The temperature rise is about 60 K for 3 nm particle sintering of rutile and anatase. Similar profiles for 4 nm sintering are shown in Figure III.7. For these simulations, the temperature rise is observed to be of the order of 35K. Thus, the temperature rise upon neck formation seems to be decreasing with particle size. This is consistent with the temperature being given by the average kinetic energy per particle; hence, for larger particles a given decrease in total potential energy (compensated by an equal increase in total kinetic energy) translates to a smaller increase in temperature. The temperature rise is however found to be independent of the starting temperature of the simulation. This is expected as in all the simulations with identical particle sizes, the decrease in surface area is similar; thereby the amount of potential energy to be converted to kinetic energy upon agglomeration is almost the same. These figures also indicate that sintering of TiO_2 nanoparticles takes place in two steps. The first step is very rapid and involves the formation of the neck region, which leads to the sudden drop in the overall configurational energy of the system, and the second step includes all the rearrangements that follow. The second step is very slow (few microseconds) and cannot be studied over the course of our molecular dynamics simulations.

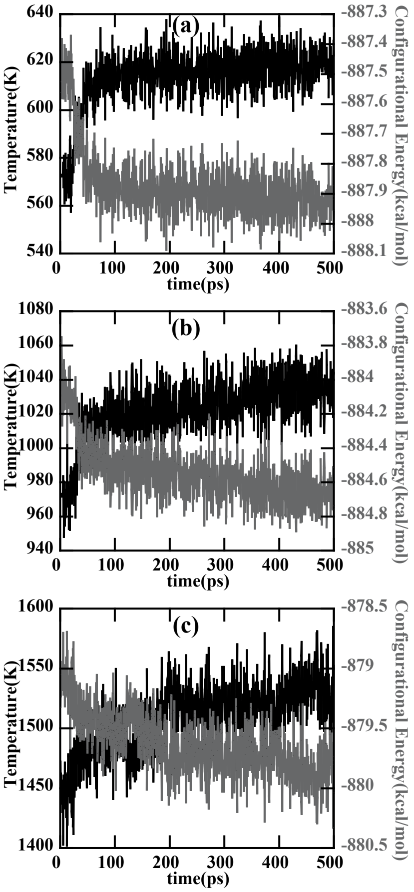

Figure III.5 Temperature and configurational energy variation with time for 3 nm anatase sintering with initial temperatures of (a) 573 K, (b) 973 K and (c) 1473 K

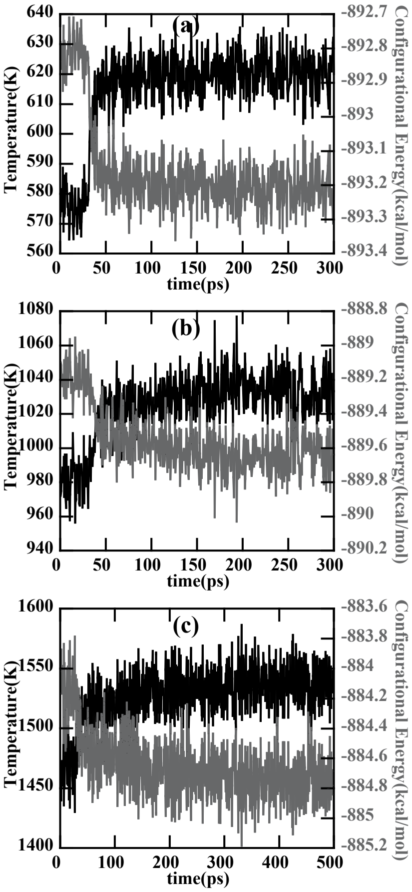

Figure III.6 Temperature and configurational energy variation with time for 3 nm rutile sintering with initial temperatures of (a) 573 K, (b) 973 K and (c) 1473 K

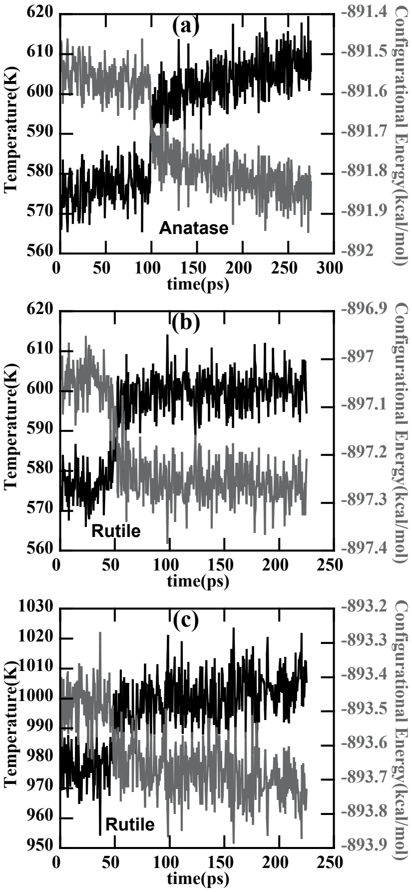

Figure III.7 Temperature and configurational energy variation with time for 4 nm sintering with initial temperatures of (a) 573 K (anatase), (b) 573 K (rutile) and (c) 973 K (rutile)

III.3.3 Shrinkage, Neck Diameter and Number of Ions in the Neck Region

In earlier studies (Raut, Bhagat et al. 1998), shrinkage was defined as $\Delta L/L_0$ where L_0 is the distance between the centers of mass of the sintering nanoparticles and ΔL is the change in this distance with time. We modify this definition to,

$$shrinkage = \frac{\left(\frac{d_1 + d_2}{2}\right) - d_{COM}}{\left(\frac{d_1 + d_2}{2}\right)} \qquad \text{(III.1)}$$

where d_1 and d_2 are the diameters of the sintering nanoparticles and d_{COM} is the distance between their centers of mass at any instance. Shrinkage is a quantitative measure of the extent of intermingling or interpenetration of the sintering particles. As per equation (III.1), shrinkage is negative when particles are not touching each other, zero when they touch each other for the first time and positive when the start intermingling. Thus, the new definition of shrinkage indicates the beginning of neck formation with a sign change. Figure III.8 show the variations in shrinkage during the course of sintering of 3 and 4 nm particles. Shrinkage increases as the particles are attracted to each other and then reaches a pseudo-steady state. It is believed that the result of sintering will be a larger spherical particle, i.e., shrinkage will finally reach unity but the time required to observe this is too long to simulate using molecular dynamics given currently available computational resources. It can be concluded from the figures that, shrinkage has no dependence on the starting temperature of the simulation but decreases as the particle size is increased. This suggests that the smaller the sintering particles, the greater is the interpenetration.

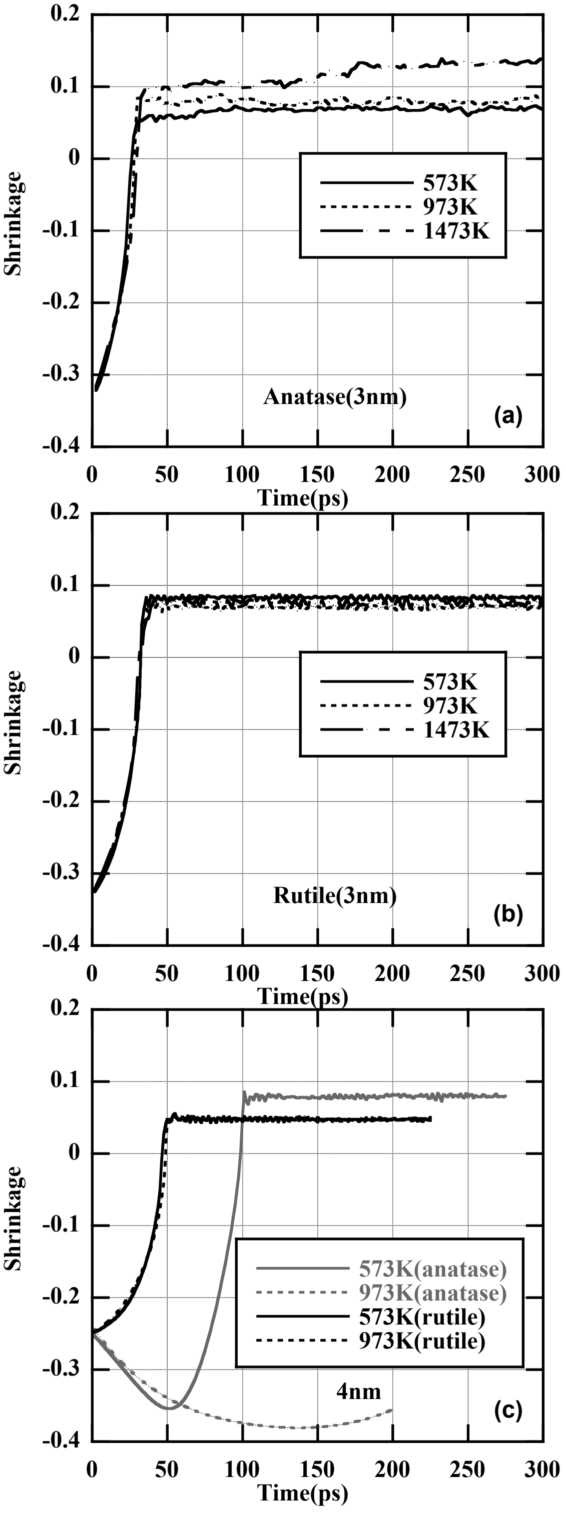

Figure III.8 Shrinkage for (a) 3 nm anatase, (b) 3 nm rutile and (c) 4 nm particles. The indicated temperatures are the starting temperatures.

The shrinkage increases with the starting temperature in the case of 3 nm anatase sintering. But no such temperature dependence is observed for 3 nm rutile sintering. It is shown later in Chapter IV that 3 nm anatase particles have a lower melting point than 3 nm rutile, thus at 1473 K the 3 nm anatase particles are close to their melting temperature leading to greater ionic mobility than their rutile counterparts leading to greater interpenetration and therefore, higher value for shrinkage.

Another important measurable quantity is the diameter of the neck region. All the ions lying within 3 Å of the orthogonal plane bisecting the line joining the centers of mass of the equally sized sintering particles are considered to be in the neck region. The diameter of this neck region increases with starting temperature of simulation for 3 nm anatase nanoparticles, ranging from 17 Å for the starting temperature of 573 K to 22 Å for the starting temperature of 1473 K. In the case of rutile simulations, no such relationship between neck diameter and temperature is observed in the 3 nm case but limited results from the 4 nm simulations suggest that neck diameter does increase with temperature. The neck diameter at the end of the first stage of 3 nm rutile sintering is about 20 Å irrespective of the starting temperature. This value is expected to be higher near the melting point of the nanoparticles under consideration. It can also be noted from Figure III.9 that 3 nm simulations take about 30-35ps to reach the pseudo-steady state neck diameter while 4 nm simulations show times greater than 50ps. This suggests that as the nanoparticle size increases the it takes longer to for the particles to achieve the pseudo-steady state.

Similarly, the number of ions in the neck regions seems to increase with temperature for 3 nm anatase particles while there is no obvious dependence on temperature in the case of rutile particles as shown in Figure III.10. Simulated X-ray diffraction patterns (see Appendix A) were determined for the agglomerates at the end of the simulations. These patterns indicated that no phase change had occurred in any of the simulations. The neck region is also examined separately for phase change. These examinations indicate that the neck region between two anatase nanoparticles becomes amorphous while the neck region between two rutile nanoparticles remains rutile.

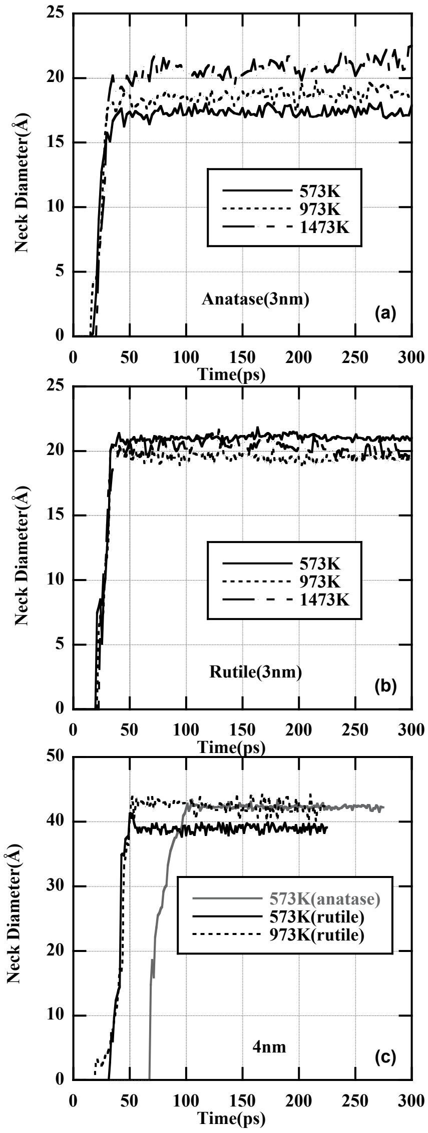

Figure III.9 Neck Diameter for (a) 3 nm anatase, (b) 3 nm rutile and (c) 4 nm particles. The indicated temperatures are the starting temperatures.

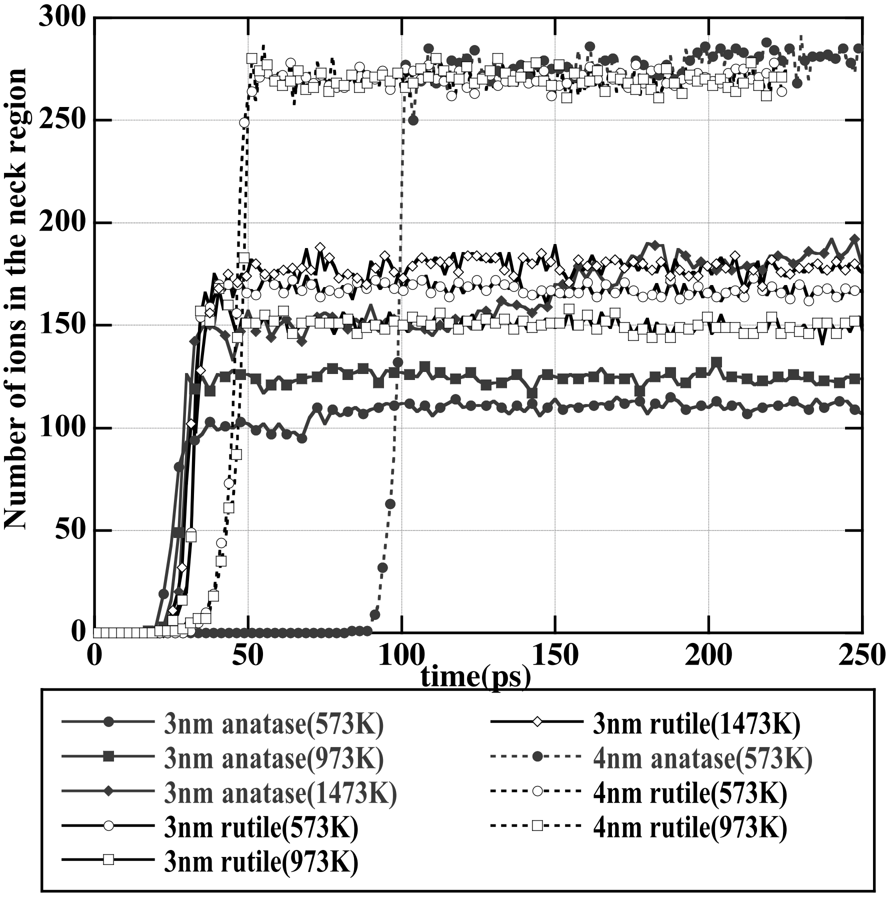

Figure III.10 Number of ions in the neck region vs time for sintering anatase and rutile nanoparticles with different starting temperatures indicated in parentheses.

III.3.4 Dependence on Particle Orientation

It is believed that crystallographic orientation also plays a vital role in the sintering of crystalline particles. This dependence would be greatly enhanced for nanosized particles. To study this effect, the duplicated particle in the 3 nm anatase simulation system was rotated about the Z-axis through various angles, namely, 20°, 45°, 90° and 180°, before starting the simulation. The simulations were repeated at 573 K. The particles attract each other initially and move towards each other along the X-axis. Such rotations of one particle about the Z-axis will ensure different crystallographic orientations along the X-axis each time and thus enable us to study the dependence on crystallographic orientation. Simulations were carried out for the 3 nm anatase particles for 0.5ns at these different initial orientations. Neck formation occurred almost at the same time in all the cases except when the rotation was 180°. In this case, the particles repelled and moved away from each other, and never collided over the period of the simulation. This proves that orientation of the nanoparticles is extremely important in the process of sintering. This is further corroborated quantitatively by Figure III.11, which shows the shrinkage, neck diameter and the number of ions in the neck region for simulations performed at these various orientations. The orientation of 90° produced maximum interpenetration, indicated by the highest shrinkage, largest neck diameter and highest number of ions in the neck region, suggesting that this initial configuration may be most favorable for sintering. It is also observed from Figure III.12 that the configurational energy of the system decreases sharply for the 90° orientation resulting in greater temperature rise at this orientation as compared to the other orientations. Similar densification observed experimentally using X-ray diffraction of larger titania particles by Kumar and coworkers

(Kumar, Keizer et al. 1992) was attributed to the anatase-rutile transformation, but no such phase transformation was detected over the course of the simulation based on the simulated X-ray diffraction patterns. No comments can be made concerning the possibility of such phase transformation over longer periods of time, which are not possible using molecular dynamics simulations. Thus, except for the 90° case, the results appear to be compatible with the idea that the surfaces of the particles are nanoscopically rough and so the rotation of particles does not affect their interaction with each other. However, the 90° case proves that crystallographic orientation is an important factor to consider when studying nanoparticle sintering.

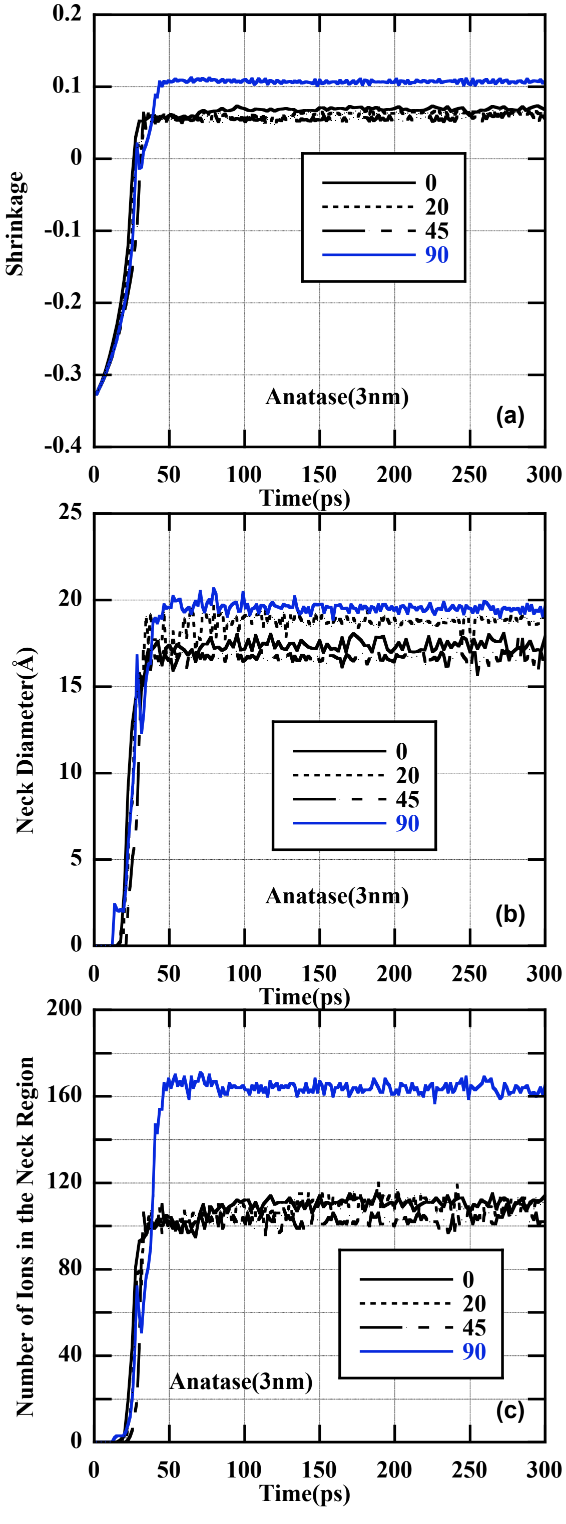

Figure III.11 (a) Shrinkage, (b) Neck diameter and (c) Number of ions in the neck region for 3 nm anatase sintering simulations at various crystallographic orientations

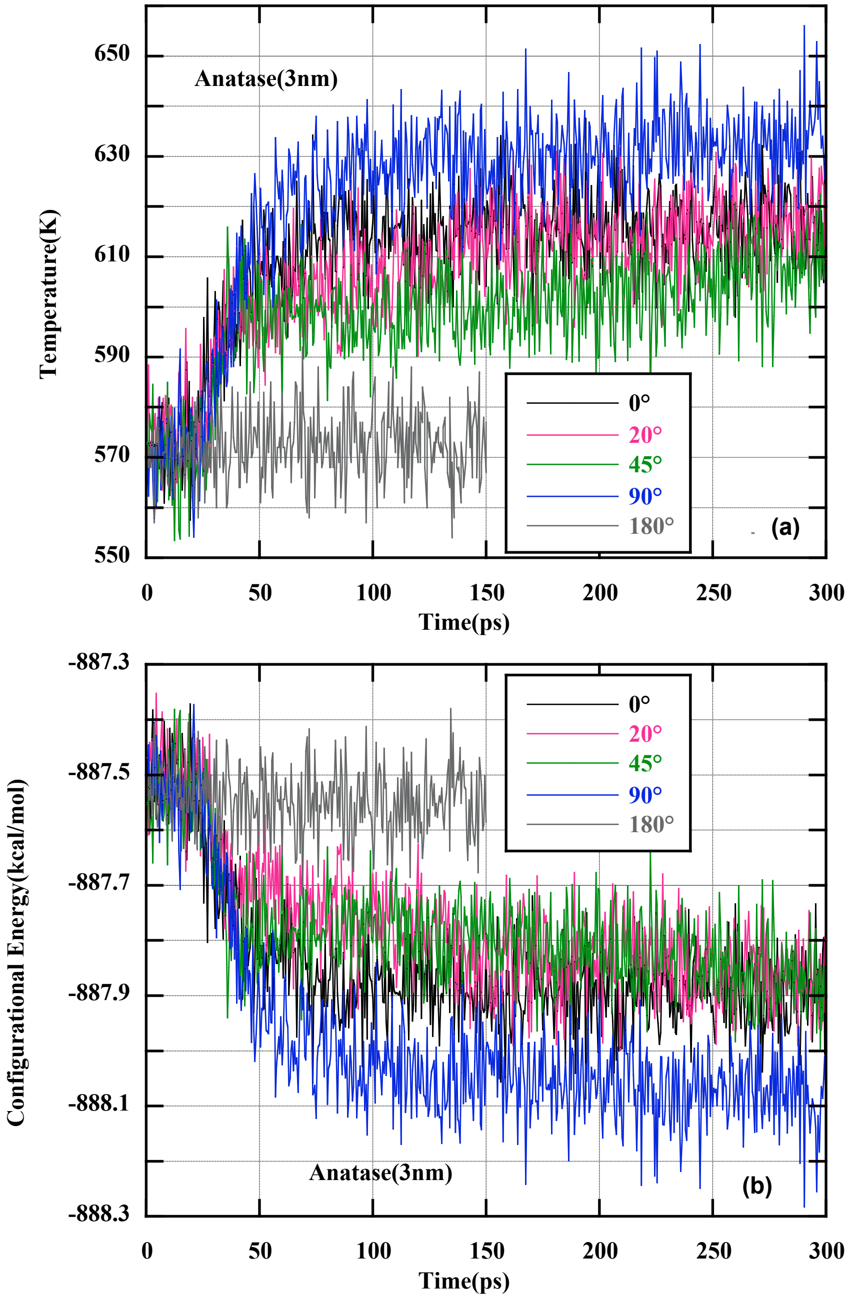

Figure III.12 (a) Temperature and (b) Configurational energy profiles of 3 nm anatase sintering at various orientations

III.3.5 Dipole-dipole Interaction

To examine the dependence of particle orientation on the sintering phenomenon, the dipole-dipole interaction between the two interacting nanoparticles before they intermingle could be of great significance. The dipole moment of an individual nanoparticle can be calculated as (Jackson 1975),

$$\bar{\mu} = \sum_i q_i \bar{r}_i \tag{III.2}$$

where $\bar{\mu}$ is the dipole moment of the particle, q_i is the charge on the ion *i*, and $\bar{r}_i$ is the position vector of ion *i*. The interaction energy between two adjacent dipoles, W_{d-d}, is given by (Jackson 1975),

$$W_{d-d} = \frac{\bar{\mu}_1.\bar{\mu}_2 - 3(\hat{n}.\bar{\mu}_1)(\hat{n}.\bar{\mu}_2)}{\left|\bar{r}_1 - \bar{r}_2\right|^3} \tag{III.3}$$

where $\bar{\mu}_1$ and $\bar{\mu}_2$ are the individual dipole moments of the interacting nanoparticles, $\bar{r}_1$ and $\bar{r}_2$ are the position vectors of the centers of mass of the particles, and $\hat{n}$ is the unit vector along $\bar{r}_1 - \bar{r}_2$. In general, the dipole-dipole interaction between particles will be the dominant contribution to the overall long-range nanoparticle-nanoparticle interaction.

Figure III.13 shows that as the angle of rotation increases the initial dipole-dipole interaction becomes more repulsive and for 180° it is repulsive enough to prevent the particles from touching each other throughout the simulation. Also, the slightly repulsive configuration at 90° orientation could explain why rotation and reorientation of particles is observed prior to neck formation. The relationship between the initial dipole-dipole interaction and the angle of rotation is almost a linear one, with the nature of interaction changing from attractive to repulsive at about 90°. At 90°, the initial dipole-dipole interaction is almost zero, suggesting that the inter-particle dynamics at this configuration are independent of individual particle dipoles and coulombic interactions between the surface ions dominate. Temporal evolution of dipole-dipole interactions showed that these interactions gradually continue to become more attractive with time until shrinkage became zero. It may be possible to model TiO_2 nanoparticles as nanoscopic spheres with fluctuating dipole moments, interacting via equation III.3, before they collide. Thus, the inter-particle dipole-dipole interaction is very critical in the sintering dynamics of nanoparticles at lower temperatures. This may not be the case for nanoparticles larger than 5 nm as observed by Ogata and coworkers (Ogata, Iyetomi et al. 2000), who suggest from their 6 nm anatase and rutile particle simulations that surface charge effects dictate the course of nanoparticle sintering. Here it should be noted that Ogata and coworkers used a variable-charge potential for their simulations in contrast to the rigid-ion-partial-charge Matsui-Akaogi potential used in this work.

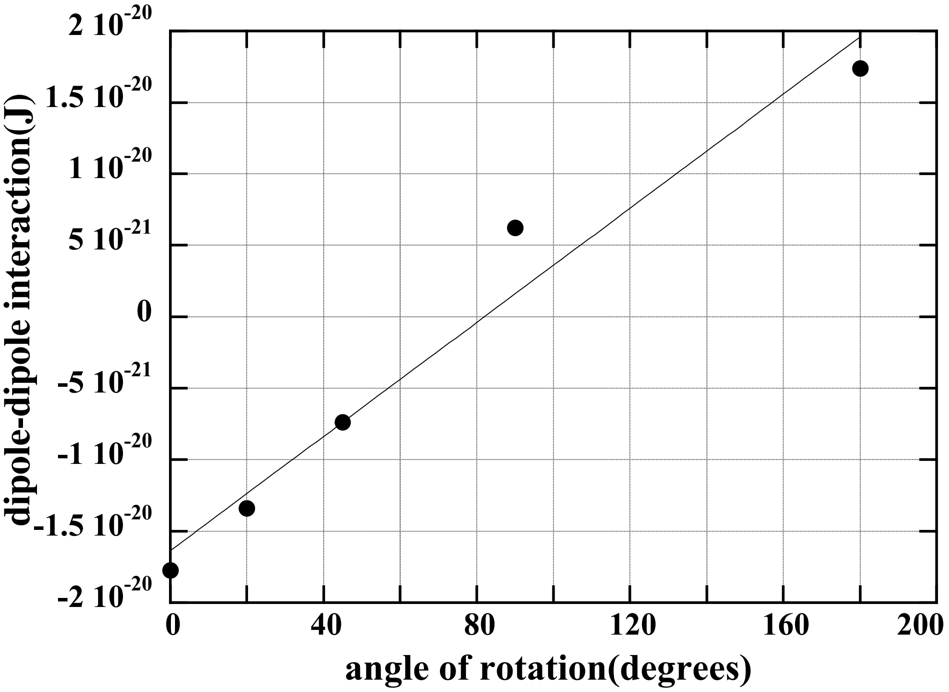

Figure III.13 Variation of dipole-dipole interaction of the nanoparticles at various initial orientations

III.3.6 Relative Displacements of Ions in the Neck and Core Regions

In order to gain further insight into the sintering mechanism, the relative ionic mobilities in the neck and core region are calculated. All nanoparticles in the simulations, have a crystalline core and an amorphous surface. In anatase and rutile lattice, the coordination number of titanium ion is six. Figure III.3 shows the variation of the co-ordination number of titanium ion in 3 nm anatase particle along the radius of the nanoparticle. The external region where the coordination number starts going below six can be considered as amorphous. Simulation results show that the thickness of this amorphous region, which is about the order of 4 Å, is independent of size and temperature. Thus, ions within a distance less than 60% of the radius of the particle from the center of mass of the particle are considered to be in the core region of the particle. All the ions within 3 Å of the orthogonal plane bisecting the line connecting centers of mass of the two sintering nanoparticles are considered to be in the neck region. Zhu and Averback (Zhu and Averback 1995) defined relative atomic displacement for a system comprising of single species as,

$$\Delta r_i(t,t') = \sqrt{\left(\left(r_i(t) - r_i(t') \right) - \frac{1}{n'} \left(\sum_{j=1}^{n'} \left(r_j(t) - r_j(t') \right) \right) \right)^2} \qquad \text{(III.4)}$$

where $r_i(t)$ is the position vector of the i^{th} atom at time t and n' is the number of neighbors of the i^{th} atom. The first term under the square-root sign is the individual atomic displacement and the second term is relative displacement of the center of mass. Following the same lines, the relative displacement of the i^{th} ion from time t to t' in our system can be calculated as,

$$\Delta r_i(t,t') = \sqrt{\left(\left(r_i(t) - r_i(t') \right) - \frac{1}{m_{Ti} n'_{Ti} + m_O n'_O} \left(\sum_{j=1}^{n'_{Ti}} m_{Ti} \left(r_j(t) - r_j(t') \right) + \sum_{k=1}^{n'_O} m_O \left(r_k(t) - r_k(t') \right) \right) \right)^2}$$

(III.5)

where $r_i(t)$ is the position vector of the i^{th} atom at time t, m_{Ti} and m_O represent the ionic masses of Ti and O ions. These are 47.9000 and 15.9994 a.m.u., respectively. The relative ionic mobility can then be calculated from the relative ionic displacement as follows,

$$\mu_{rel} = \lim_{t \to \infty} \frac{\langle \Delta r^2 \rangle}{2dt} \tag{III.6}$$

where the numerator is the relative mean-square displacement in time t and d is the dimensionality of the system, which in this case is three.

Figures III.14 and III.15 compare the core and neck region mobilities for sintering anatase and rutile 3 nm particles, respectively. The initial peak in the core mobility suggests fast motion of the ions on first contact between sintering particles. It should also be noted that the relative ionic mobility in the neck region remains more than that in the core region throughout all simulations by about one order of magnitude. Similarly, Raut and coworkers (Raut, Bhagat et al. 1998) reported that relative mobility of aluminum atoms in the neck region was about two orders of magnitude greater than that in the core region for sintering aluminum particles. The relative mobility in the neck and core regions does not show any significant dependence on phase but are observed to be increasing with initial temperature of the particles, as expected. The relative ionic mobility of ions in the neck region is a representation of surface diffusion.

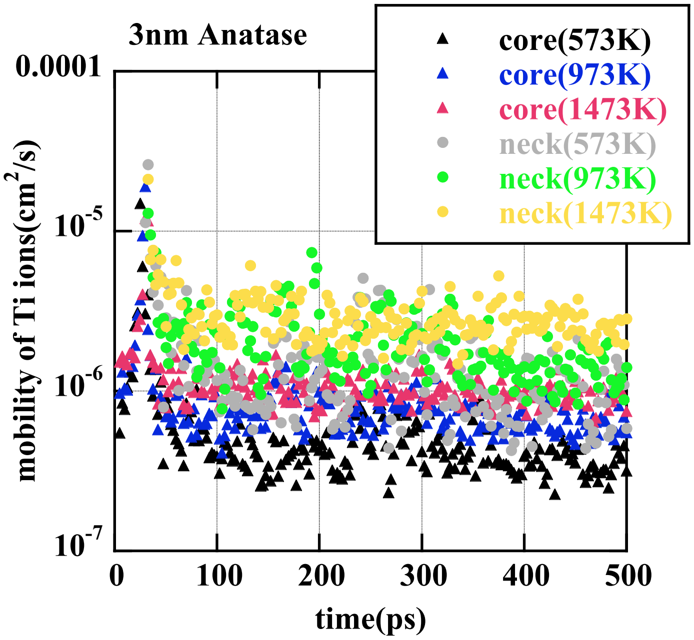

Figure III.14 Relative mobilities of Ti ions in the core and neck regions for a 3 nm anatase sintering simulation with initial temperatures of 573 K, 973 K and 1473 K

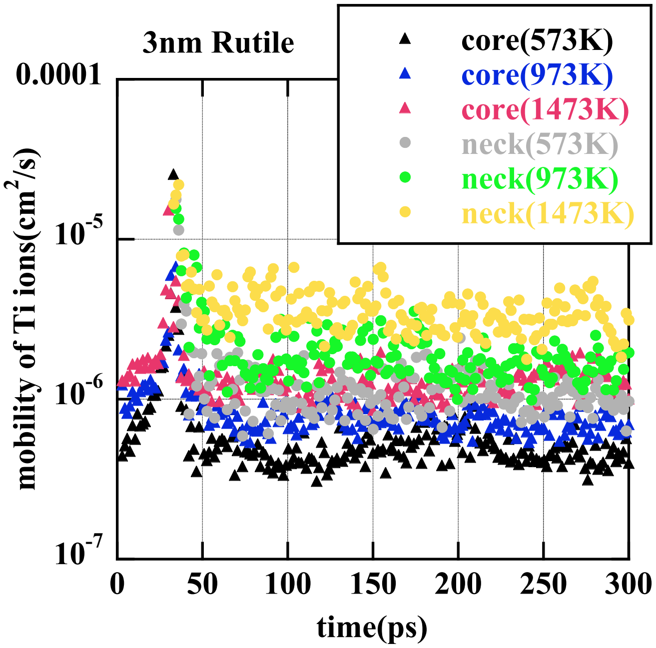

Figure III.15 Relative mobilities of Ti ions in the core and neck regions for a 3 nm rutile sintering simulation with initial temperatures of 573 K, 973 K and 1473 K

III.4 Conclusions

A number of interesting details about the sintering characteristics of TiO_2 nanoparticle systems have been elucidated. The study demonstrates that the sintering of anatase and rutile nanoparticles is very rapid and occurs in a few picoseconds. The initial stage of the sintering process involves neck formation, upon first contact, followed by gradual particle interpenetration and broadening of the neck region. The surface energy is converted to kinetic energy thereby increasing the temperature. The temperature rise upon sintering is found to be independent of the initial temperature of the sintering particles but dependent on the particle size. It is about 65K for 3 nm particles, while it drops down to 35K for 4 nm particles. Thus, the temperature rise for micron-sized particles will be negligible and hence, can be neglected from models for the sintering mechanism of micron-sized particles. Higher initial temperatures promote greater intermingling of anatase particles leading to larger neck sizes and higher shrinkage. No such dependence is observed for rutile particles under the temperatures considered. The relative orientation of sintering nanoparticles has a strong influence on the shrinkage and the neck sizes, suggesting that the contributions from surface diffusion can be altered by variation of initial orientation. It is also found that increasing the particle size slows down the sintering kinetics. The neck diameter at a given initial temperature was found to be larger for 4 nm particle as compared to that of 3 nm particles.

The sintering simulations at lower temperatures indicate that the dipole-dipole interactions between nanoparticles play a very important role. It may be possible to model titania nanoparticles as spheres with fluctuating dipole moments that undergo collision before the onset of sintering.

Two-particle systems are useful for studying the isolated sintering process, but systems with larger number of particles with periodic boundary conditions could be employed in future to study many-particle sintering. Further efforts are directed toward correlating the various observations and developing scaling laws for sintering at the nanoscales that can be applied to phenomenological models of particle sintering. These are discussed in Chapter IV.

CHAPTER IV

SINTERING OF TiO_2 NANOPARTICLES: COMPARISON WITH PHENOMENOLOGICAL MODELS

IV.1 Introduction

As the importance of understanding the sintering phenomenon is clear from Chapters I and III, many attempts at developing phenomenological models to describe sintering of particles have been made since the 1940s (German 1996). There have been different models developed for ceramics that describe the sintering process of equal sized particles utilizing the neck growth rate as a scaling parameter (Coblenz, Dynys et al. 1980). Most of them are valid for the early stages of sintering and are often used in numerical solutions (Kobata, Kusakabe et al. 1991; Kruis, Kusters et al. 1993; Kraft and Riedel 2004). The applicability of most of models to nanosized particles is debatable. Many of these models do not distinguish between amorphous and crystalline particles or polar and non-polar particles. It is apparent that the interactions between two amorphous particles will be different than two crystalline particles, and hence, there is a need to model them differently. It is evident that, as the particle size decreases, the percentage of atoms or ions on the surface of the particle increases. In other words, surface effects become more and more significant with decrease in particle size. As it can be argued from Figure III.3 and Table III.1, the 3 nm TiO_2 nanoparticles have an amorphous surface layer about 4 to 5 Å thick with about 35 to 45% of ions residing in this layer. Thus, the fact that these particles are partly amorphous and partly crystalline will play a vital role in modeling their sintering. It has also been hypothesized that the extremely high internal pressure of smaller particles is responsible for the inapplicability of the sintering models to these particles. For example, the pressure inside a 10 nm TiO_2 nanoparticle is reported to be ~2000 atmospheres and it further increases with decrease in particle size (Ding and Liu 1997; Ehrman, Friedlander et al. 1998). Such high internal pressure has a direct impact on the diffusivity of the atoms or ions in the particle, which in turn affects kinetics the sintering mechanism. Thus, it is believed that there exists a need to incorporate the fact that these particles are comprised of individual atoms or ions into the model development. The sintering phenomenon has been studied from the atomic point of view using molecular dynamics simulations in Chapter III. The insights obtained from the molecular dynamics simulations can be used to evaluate and improve the general phenomenological models to extend their applicability to nanosized particle sintering.

Zachariah and Carrier (Zachariah and Carrier 1999) have reported positive results upon applying phenomenological models to sintering of silica nanoparticles and comparing them to results obtained via molecular dynamics simulations. It should be noted that silica is amorphous and no charged species where present in their molecular dynamics study. Applicability of these phenomenological models to anatase and rutile nanoparticles is studied in this chapter.

Surface diffusion and grain boundary diffusion are the most significant mass transport processes for smaller particles due to their high surface curvature as reported for gold and copper nanoparticles by Zeng and coworkers (Zeng, Zajac et al. 1998). The process of diffusion is extremely sensitive to temperature and physical state of matter. The diffusion rates in a liquid can be many orders of magnitude higher than those in a solid. In the flame reactors where TiO_2 nanoparticles are manufactured, the sintering nanoparticles are found to be in an adiabatic environment as they are present a low pressure dilute gaseous phase. Infrequent collisions with gaseous molecules ensure that the total energy of the sintering particles remains constant and is not dissipated. A decrease in surface energy during sintering in an adiabatic environment increases the kinetic energy and hence the temperature. If the pressure is low and the collisions with the gaseous solvent molecules are infrequent, then this temperature will keep rising with every subsequent particle-particle collision and could consequently cause melting. Hence, accurate knowledge of melting points of nanoparticles is required prior to the modeling of the sintering process. The melting point or particles has been reported to decrease with increase in the percentage of surface atoms, which happens with decreasing particle size. This is referred to as “melting point depression”. For example, the melting point of gold nanoparticles drops sharply as the particle diameter goes below 5 nm as indicated in Figure IV.1 (Buffat and Borel 1976).

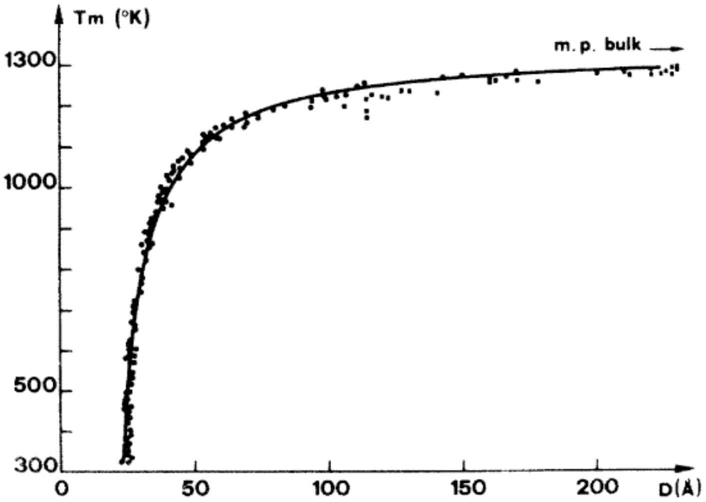

Figure IV.1 Melting point depression observed for gold particles.

IV.2 Melting point of TiO_2 nanoparticles

IV.2.1 Simulation Details

A series of molecular dynamics simulations to determine the melting points of anatase and rutile nanoparticles were performed using DL_POLY, version 2.13 (Smith 1987; Smith and Forester 1996). The Matsui-Akaogi forcefield (Matsui and Akaogi 1991) has been selected to describe the interactions between Ti and O ions. The details and advantages of this forcefield over the other reported forcefields for TiO_2 have been listed in Section I.2. The forcefield parameters are listed in Table I.2. Anatase and rutile nanoparticles with 2.5, 3, 3.5, 4 and 5 nm diameter are considered. For each sized nanoparticle, an NVT simulation was performed for 0.5ns with a time step of 0.5fs after which the temperature was incremented by 100 K. This procedure was repeated until the temperature was well above the reported bulk melting point of TiO_2. No periodic boundary conditions were used in order to simulate isolated nanoparticles and the cut-off used was large enough to include all the ions in the energy and force calculations. The leap-frog algorithm is used in conjunction with the multiple-step method to integrate the Newton's equation of motion using DL_POLY.

IV.2.2 Simulated X-ray Diffraction

The most prominent X-ray diffraction peaks in anatase and rutile are (101) located at 25.5° and (110) located at 27.5°, respectively. Simulated X-ray diffraction patterns are calculated from the Cartesian coordinates of the ions in the nanoparticles at each temperature. It is observed that the above-mentioned prominent peaks become shorter and broader indicating loss of crystallinity. The temperature at which these peaks are lost is where the nanoparticle has completely melted. The resultant particle is in liquid state. The X-ray diffraction patterns for 2.5 nm, 3 nm, 3.5 nm and 4 nm anatase and rutile particles are shown in Figures IV.3, IV.4, IV.5 and IV.6, respectively.

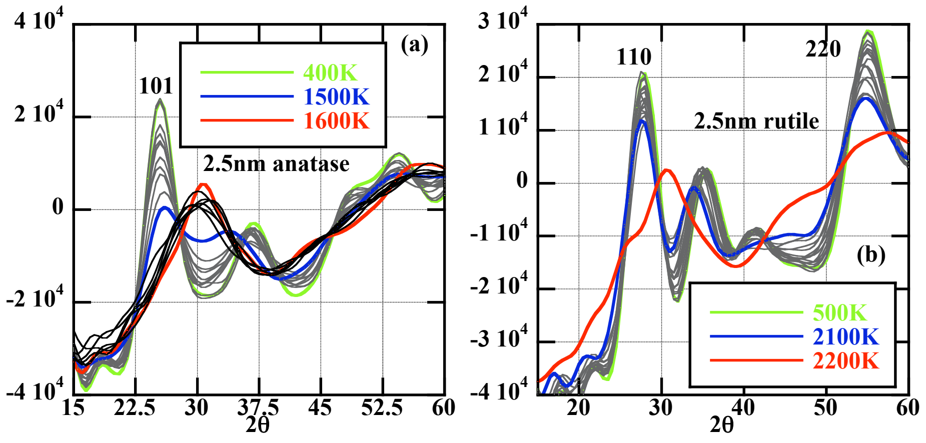

Figure IV.2 X-ray diffraction patterns of 2.5 nm (a) anatase and (b) rutile nanoparticles with increasing temperature.

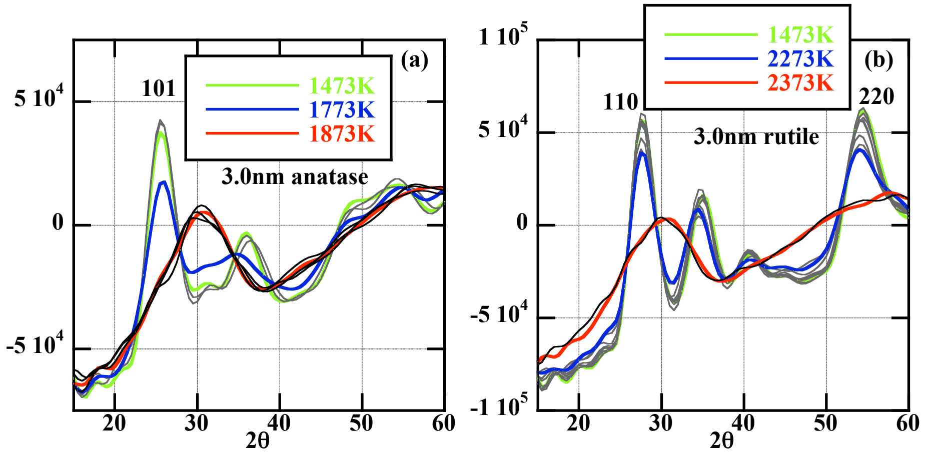

Figure IV.3 X-ray diffraction patterns of 3.0 nm (a) anatase and (b) rutile nanoparticles with increasing temperature.

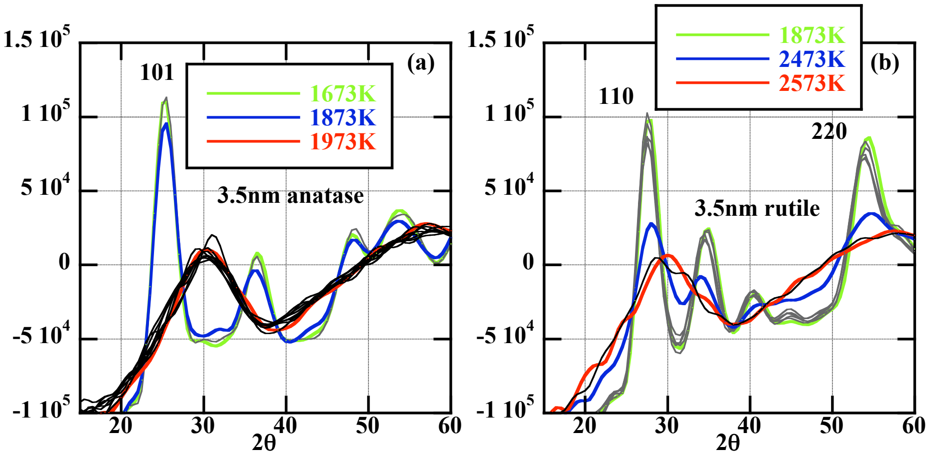

Figure IV.4 X-ray diffraction patterns of 3.5 nm (a) anatase and (b) rutile nanoparticles with increasing temperature.

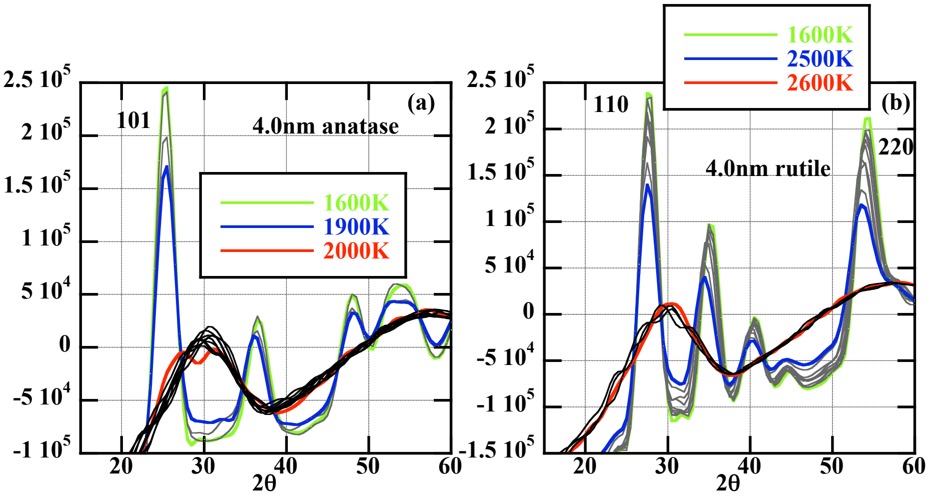

Figure IV.5 X-ray diffraction patterns of 4.0 nm (a) anatase and (b) rutile nanoparticles with increasing temperature.

IV.2.3 Pair Correlation Function

The Ti-Ti pair correlation function can also be used as an indication of melting phenomenon. The equilibrium distance between a Ti ion and its nearest neighbor Ti ion is ~3.05 Å in an anatase crystal. The loss of crystallinity is indicated by the decrease in the height of the peak at ~3.05 Å. In a molten particle the position of this peak shifts to a higher distance, as Ti ions at higher temperature have greater kinetic energy. Figures IV.6, IV.7, IV.8 and IV.9 show Ti-Ti pair correlation functions at various temperatures for 2.5 nm, 3.0 nm, 3.5 nm and 4.0 nm anatase and rutile nanoparticles.

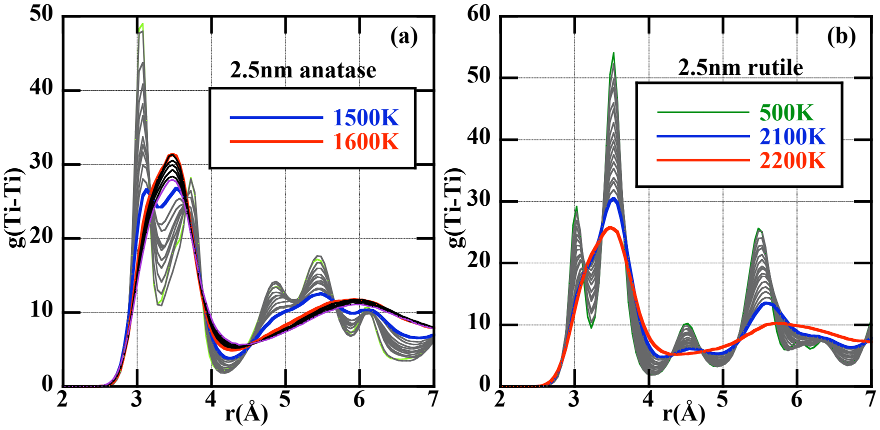

Figure IV.6 g (Ti-Ti) for 2.5 nm (a) anatase and (b) rutile nanoparticles with increasing temperature.

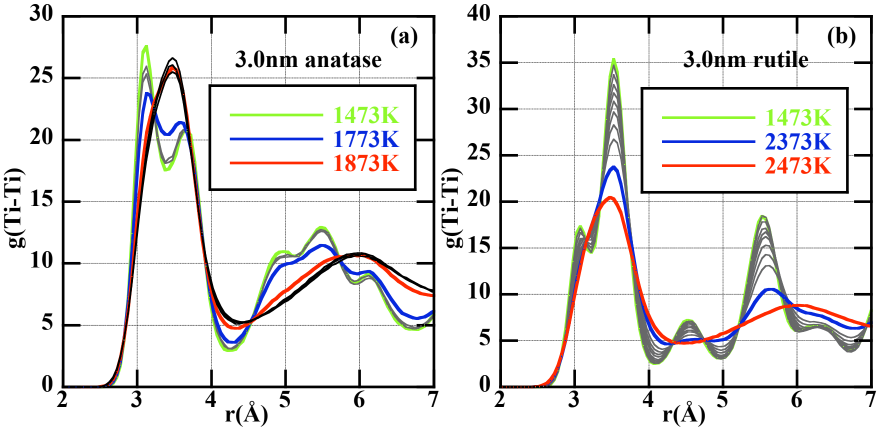

Figure IV.7 g (Ti-Ti) for 3.0 nm (a) anatase and (b) rutile nanoparticles with increasing temperature.

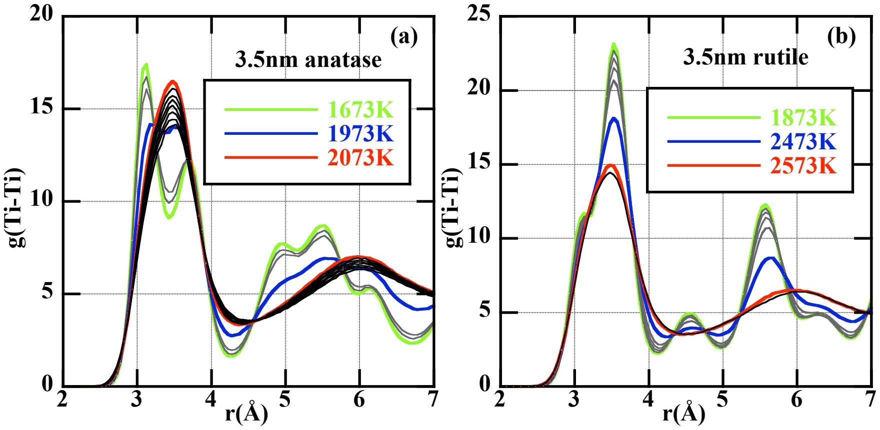

Figure IV.8 g (Ti-Ti) for 3.5 nm (a) anatase and (b) rutile nanoparticles with increasing temperature.

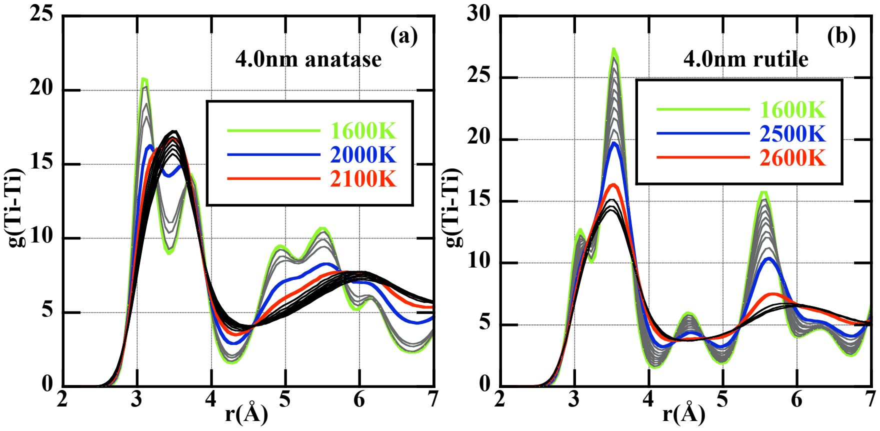

Figure IV.9 g (Ti-Ti) for 4.0 nm (a) anatase and (b) rutile nanoparticles with increasing temperature.

IV.2.4 Diffusivity

Diffusivity is another physical quantity used to detect phase transformation. Solids generally have diffusivities of the order of 10^{-12} m^2/s or lower, while liquid diffusivities are about 10^{-9} m^2/s (Bird, Stewart et al. 2002). As particle size decreases, percentage of surface atoms/ions increases and thus, surface diffusivity is very important for nanoparticles. It has been shown in Chapter II that TiO_2 nanoparticles with diameters ranging from 2.5 nm to 5 nm have a 4-5 Å thick amorphous liquid-like outer surface layer. Since about 35% to 45% of the total ions reside in this layer for the nanoparticles considered here (particle diameter between 2.5 nm and 5 nm), the overall diffusivity of the solid nanoparticles is expected to be slightly higher than bulk solid diffusivity.

The diffusivity of Ti and O ions in various nanoparticles considered at different temperatures is calculated using the equation (Frenkel and Smit 2002),

$$D = \lim_{t \to \infty} \frac{\langle r^2 \rangle}{2dt} \tag{IV.1}$$

where $\langle r^2 \rangle$ is the mean square displacement of the atoms in time t and d (=3) is the dimensionality of the system. The values of ionic diffusivities are of the order of 10^{-11} m^2/s at lower temperatures and increase to 10^{-9} m^2/s at higher temperatures indicating that melting has occurred. The Ti and O ionic diffusivities calculated utilizing the trajectories obtained from the molecular dynamics simulations are shown in Figure IV.10.

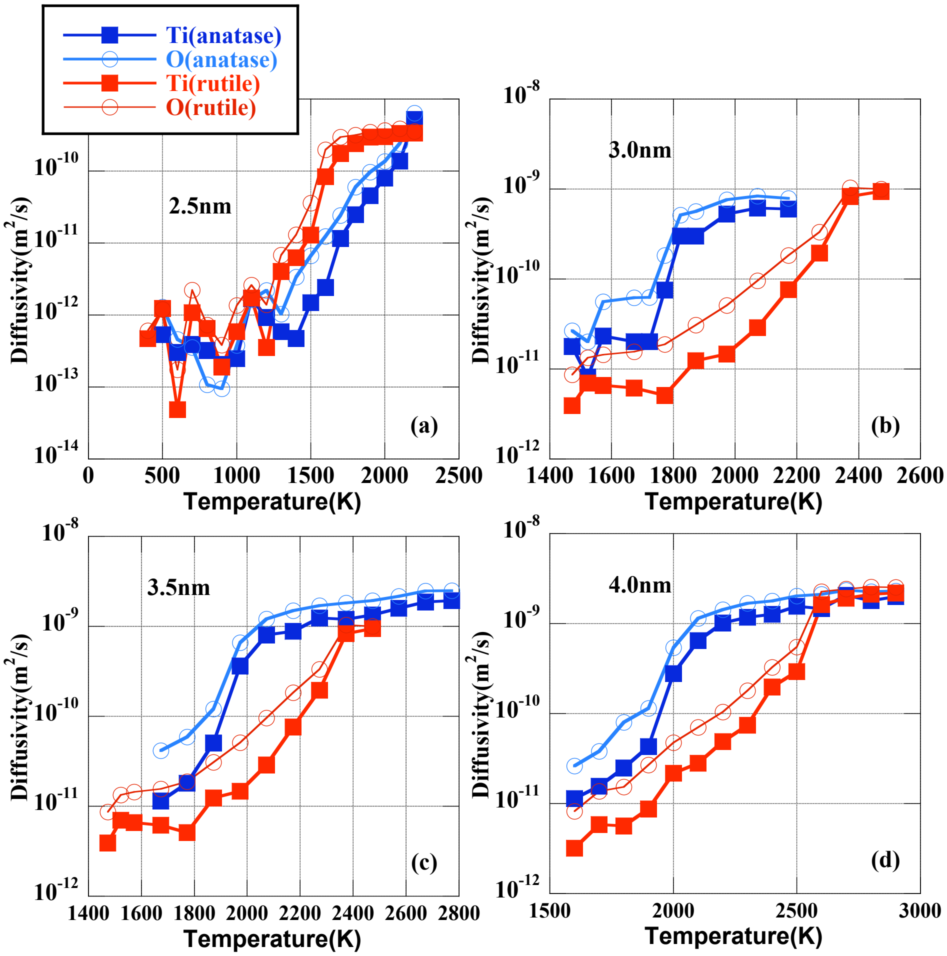

Figure IV.10 Ionic diffusivities of Ti and O ions in (a) 2.5 nm, (b) 3.0 nm, (c) 3.5 nm and (d) 4.0 nm anatase and rutile nanoparticles over various temperatures.

IV.2.5 Lindemann Index

The Lindemann index, δ, is extremely useful in identifying solid to liquid phase transformation (Egorov, Brodskaya et al. 2002; Egorov, Brodskaya et al. 2003; Egorov, Brodskaya et al. 2006). It has been used in the past to study melting of various metallic and non-metallic clusters (Lee, Lee et al. 2001; Lee, Nieminen et al. 2001; Zhou, Karplus et al. 2002; Alavi and Thompson 2006), isolated homopolymers (Zhou, Karplus et al. 1997), heteropolymers (Zhou and Karplus 1997) and proteins (Zhou, Vitkup et al. 1999). It is a distance fluctuation criterion for melting as shown in equation (IV.2),

$$\delta = \frac{2}{N(N-1)} \sum_{i=1}^{N-1} \sum_{j=i+1}^{N} \frac{\sqrt{\left\langle r_{ij}^{2} \right\rangle_t - \left\langle r_{ij} \right\rangle_t^{2}}}{\left\langle r_{ij} \right\rangle_t} \tag{IV.2}$$

where r_{ij} is the separation between atoms *i* and *j*, and $\langle \ \rangle_t$ indicates a time average.

The Lindemann index was first introduced in 1910 by F. A. Lindemann (Zhou, Karplus et al. 2002). The atoms in solids undergo small amplitude variations or fluctuations about their equilibrium lattice positions, which are accumulated in the Lindemann index. Hence, it increases with temperature for a solid and has been found to reach a critical value at the melting temperature beyond which it cannot increase without damaging or destroying the lattice, thereby causing melting. This critical value generally lies in the range of 0.1 to 0.15 for simple solids, and has been found to be independent of the type of substance, the nature of the interaction potential and the crystal structure. At the melting point, the lattice atoms gain some translational freedom and the Lindemann factor is enhanced by as much as a factor of 3.

An average value of the Lindemann index was calculated at each simulation temperature for various particle sized under consideration. The variation of the

Lindemann indices with temperature of different sized anatase and rutile nanoparticles are shown in Figure IV.11

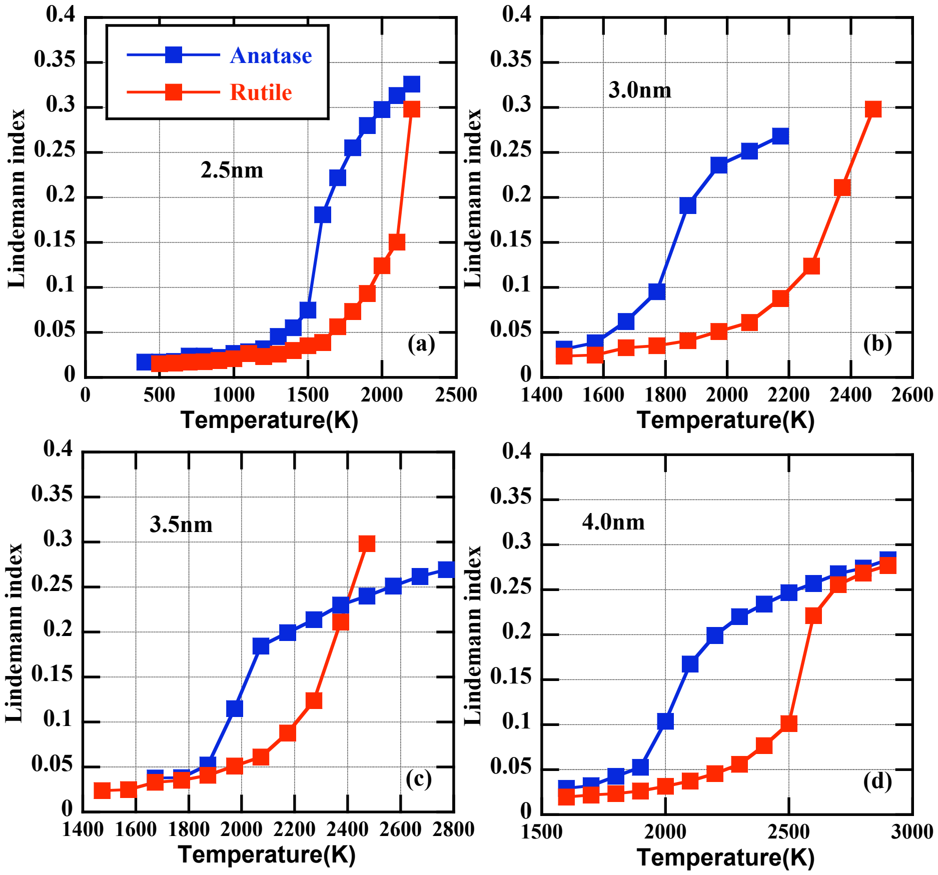

Figure IV.11 Lindemann Incides for (a) 2.5 nm, (b) 3.0 nm, (c) 3.5 nm and (d) 4.0 nm anatase and rutile nanoparticles

The melting points of 2.5, 3, 3.5, 4 and 5 nm anatase and rutile nanoparticles obtained from analyzing the X-ray diffraction patterns, pair correlation functions, ionic diffusivities and the Lindemann indices are represented in Figure IV.12. The melting point of nanoparticles can also be estimated using the Buffat and Borel (Buffat and Borel 1976) empirical formula,

$$T_{mp} = T_m\left[1 - \frac{4}{L\rho_s d_p}\left\{\sigma_s - \sigma_l\left(\frac{\rho_s}{\rho_l}\right)^{\frac{2}{3}}\right\}\right] \tag{IV.3}$$

where T_{mp} is the melting point of the nanoparticle, T_m is the bulk melting temperature in K, L is the latent heat of melting in J/kg, d_p is the particle diameter in m, ρ_s,ρ_l are the solid and liquid densities in kg/m^3 and σ_s,σ_l are the solid and liquid surface tensions in J/m^2. The equation (IV.3) can be solved for anatase and rutile using the following values,

$L_{anatase}$=91.25 kJ/mol (Li and Ishigaki 2002)

L_{rutile}=66.9 kJ/mol (Li and Ishigaki 2002)

T_m=2143 K (Li and Ishigaki 2002)

$\rho_{anatase}$=3893 Kg/m^3 (Li and Ishigaki 2002)

ρ_{rutile}=4249 kg/m^3 (Li and Ishigaki 2002)

ρ_l=3249 kg/m^3 (Dingwell 1991)

$\sigma_{anatase}$=0.51 J/m^2 (lowest energy anatase surface) (Barnard, Zapol et al. 2005)

σ_{rutile}=1.25 J/m^2 (lowest energy rutile surface) (Barnard, Zapol et al. 2005)

σ_l=0.38 J/m^2 (Ikemiya, Umemoto et al. 1993; Li and Ishigaki 2002)

The melting points obtained from the empirical formula are shown in Figure IV.12. The melting point of nanoparticles calculated from simulations show the correct trend, i.e., they increase with increasing particle size seem to be tending towards an asymptotic behavior for larger particles. The melting points obtained via simulations for 2.5 nm anatase and rutile nanoparticles are comparable to those predicted by the Buffat and Borel empirical formula (Buffat and Borel 1976). For all larger nanoparticles, simulations are found to over predict the melting points when compared to the empirical formula.

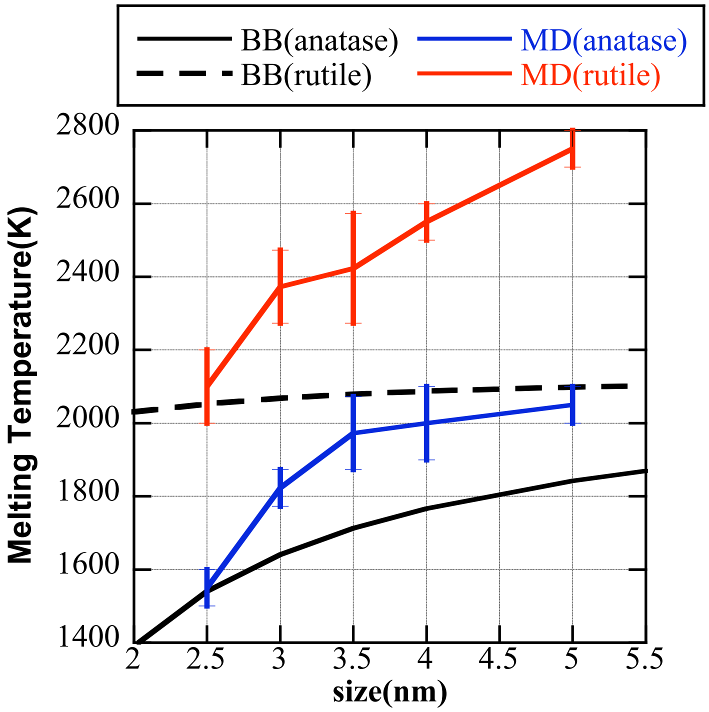

Figure IV.12 Melting point of anatase and rutile nanoparticle calculated using Buffat-Borel (BB) model and molecular dynamics (MD) simulations.

IV.3 Model Development

Consider a system comprising of two identical spherical nanoparticles, each with N TiO_2 units. During the process of sintering, a neck is formed between the spheres, which grows with time. A larger spherical particle is assumed to be final result. It is believed that total energy of the system (E) can be divided into contributions from the bulk (E_{bulk}) and the surface ($E_{surface}$) as (Lehtinen and Zachariah 2002),

$$\begin{aligned} E &= E_{bulk} + E_{surface} \\ E_{bulk} &= 2N[\varepsilon_b(0K) + c_v T_p] \qquad \text{(IV.4)} \\ E_{surface} &= \sigma_{sv} a \end{aligned}$$

where a is the total surface area of the coalescing nanoparticles, σ_{sv} is the solid-vapor surface tension, $\varepsilon_b(0K)$ is the binding energy at absolute zero temperature, c_v is the constant volume heat capacity and T_p is the temperature of the particle. As the collisions with the dilute gas in the flame reactor are very infrequent, the dissipation of energy through such collisions will be negligible and can be neglected. The loss of energy via radiation is also found to be insignificant when compared with contributions from the bulk and surface. Thus, any changes in the total energy of the system can be represented as,

$$\frac{dE}{dt} = 2N\frac{d}{dt}\left(c_v T_p\right) + \frac{d}{dt}\left(\sigma_{sv} a\right) \qquad \text{(IV.5)}$$

Since, N is the number of TiO_2 units, it does not vary with time. As there is no energy loss to the surrounding, the system is adiabatic and the total energy of the system will remain constant. Hence,

$$\frac{dE}{dt} = 0 = 2N\frac{d}{dt}\left(c_v T_p\right) + \frac{d}{dt}\left(\sigma_{sv} a\right) \qquad \text{(IV.6)}$$

c_v and σ_{sv} do not vary appreciably for solids over wide range of temperatures and therefore, can be assumed to be constant. With this assumption we can rewrite equation (IV.6) as,

$$\frac{dT_p}{dt} = -\frac{\sigma_{sv}}{2Nc_v}\frac{da}{dt} \tag{IV.7}$$

Koch and Friedlander (Koch and Friedlander 1990) postulated that for the reduction in area of sintering particles can be approximated as a linear rate, which can be mathematically expressed as,

$$\frac{da}{dt} = -\frac{1}{\tau_f}\left(a - a_{sph}\right) \tag{IV.8}$$

where τ_f is the characteristic sintering time and a_{sph} is the surface area of the spherical particle, which is assumed to be the final outcome of the sintering process. As the temperatures observed in the sintering simulations never exceeded the melting points, solid-state diffusion can be assumed. The characteristic time for sintering via solid-state diffusion is given as (German 1996),

$$\tau_f = \frac{3kT_pN}{64\pi\sigma_{sv}D(T_p)} \tag{IV.9}$$

where k is the Boltzmann's constant and $D(T_p)$ is the diffusion coefficient at temperature T_p. Substituting equation (IV.9) in equation (IV.8) we get,

$$\frac{da}{dt} = -\frac{64\pi\sigma_{sv}D(T_p)}{3kT_pN}\left(a - a_{sph}\right) \tag{IV.10}$$

Equation (IV.7) and (IV.10) can be solved simultaneously using an ODE (ordinary differential equation) solver in order to predict the temperature profile of sintering particles. It should be noted that the equation (IV.10) is very non-linear and extremely sensitive to temperature. The sensitivity comes from the exponential dependence of the diffusion coefficient on temperature:

$$D \cong A\exp\left(-\frac{B}{T_p}\right) \tag{IV.11}$$

where A and B are non-negative constants. The results obtained by solving (IV.7) and (IV.10) for 3 nm anatase (N=417) and 3 nm rutile (N=491) with starting temperatures of 573 K, 973 K and 1473 K are shown in Figure IV.13. As the model does not distinguish between anatase and rutile polymorphs of TiO_2, the solutions will be solely dependent on the number of TiO_2 units in the nanoparticles (N). Anatase has fewer TiO_2 units than rutile for the same particle size, due to its lower density. As the temperature varies inversely with the number of TiO_2 units, anatase will always have a larger temperature compared to rutile. This is observed in the model solution plotted in Figure IV.13. According to the model solution, the temperature increases gradually during sintering until a steady-state is achieved at longer times. The time taken to approach this steady-state increases dramatically as the systems initial temperature is increased. It is of the order of milliseconds when the starting temperature is 573 K, a few microseconds when the starting temperature is 973 K and few hundred nanoseconds when the initial temperature is 1473 K. In each of the above cases, the overall temperature rise is about 80 to 100 K. A temperature rise of about 65K was observed in the molecular dynamics simulations of 3 nm particles to reach a pseudo-steady state in few picoseconds. Thus both, the predicted temperature rise and the predicted time required to achieve it, are over-predicted by the model. It should be noted that if the simulation was run for very long period of time a slight increase in temperature is anticipated. Even if the simulation temperature becomes comparable to the model solution, the time required to achieve that temperature is highly over predicted. The discrepancy between simulation and model solution may be due to an incorrect assumption made during model development. It has been assumed that the surface area reduction follows a linear rate law as suggested by Koch and Friedlander. The assumption predicts the overall trend correctly but breaks down when applied to timescales of the order of 10^0-10^3 picoseconds, which are the timescale relevant for the molecular dynamics simulations. It has been shown that Koch and Friedlander (Koch and Friedlander 1990) linear rate law for surface reduction successfully predicts the temperature variations of sintering silica particles by Zachariah and Carrier (Zachariah and Carrier 1999). It should be noted that the TiO_2 nanoparticle considered in the simulations reported in Chapter II contain charged species and are crystalline, unlike the uncharged and amorphous silica nanoparticles considered by Zachariah and Carrier. Hence, with the goal of better predicting the temperature profiles of sintering TiO_2 nanoparticles, the area reduction can be calculated directly using the trajectories obtained from the molecular dynamics simulations unlike the empirical predictions made using Koch and Friedlander.

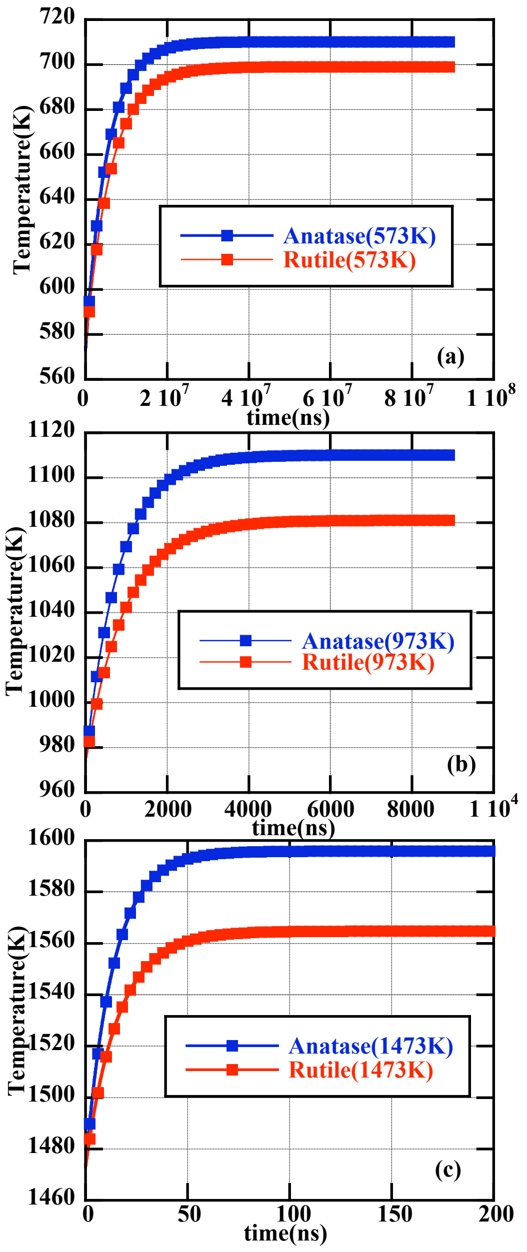

Figure IV.13 Model solution for 3 nm anatase and rutile nanoparticles at (a) 573 K, (b) 973 K, and (c) 1473 K.

IV.3.1 Surface Area Calculation

Various methods to calculate the solvent accessible surface area of nanoparticles and proteins have been reported in the literature (Gavezzotti 1985; Meyer 1988; Perrot, Cheng et al. 1992; Legrand and Merz 1993). Most of these methods are computationally very demanding. The surface area needs to be calculated at each timestep of the simulation to determine *da/dt*. Following the Meyer method, the nanoparticle system is embedded in a rectangular mesh and each mesh point is examined one by one. If the mesh point under consideration is within the Van der Waal's radii of any of the ions in the nanoparticle, then that point is counted towards volume calculation. Van der Waal's radii for Ti and O ions are 2.5 Å and 1.54 Å, respectively (Bondi 1964). The mesh points, which do not lie within the nanoparticle volume are then examined for proximity to nanoparticle surface. The area and volume calculated at numerous time intervals during the simulation is shown in Figure IV.14. The figure shows that as soon as the particles touch each other, the total area goes down dramatically. Once the neck diameter has reached certain critical value, the decrease in surface area is very gradual. This behavior is very different from that predicted by the Koch and Friedlander (Friedlander and Wu 1994) linear rate assumption. It has been shown in Chapter II that these nanoparticles have an outer amorphous layer of about ~4 Å in width, while the core is crystalline. The width of this amorphous surface layer is independent of temperature. The self-diffusion within this amorphous layer is fast and liquid-like. This may explain the accelerated initial reduction in surface area. As the shrinkage reaches a certain threshold value, the crystalline cores of the particle come in contact with each other in the neck region. Beyond this point, the diffusion mostly occurs along the grain boundaries, which is slow and solid-like. This could account for the slow decline in surface area after about 25ps of the start of the simulation.

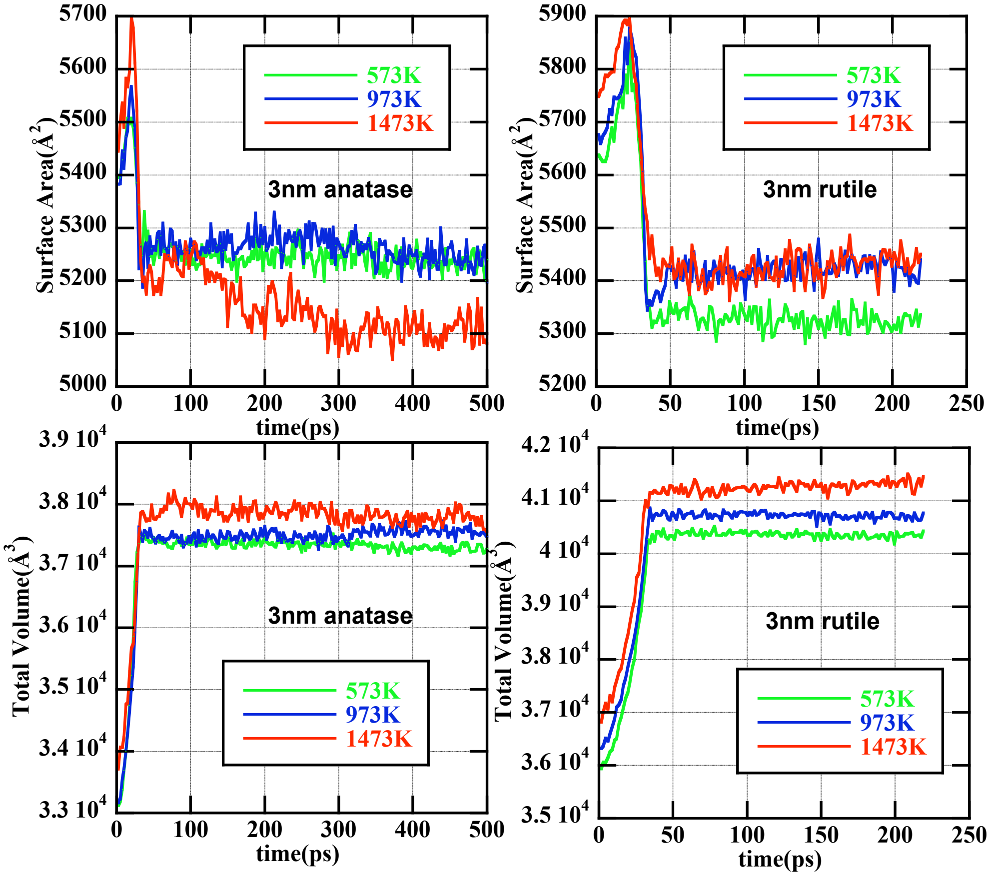

Figure IV.14 Surface area and Total volume of 3 nm anatase and rutile nanoparticles undergoing sintering at various starting temperatures calculated using the Meyer method.

IV.3.2 Model Predictions

Using the surface area calculated by the Meyer method, the rate of change in surface area, *da/dt,* is computed and inserted into equation (IV.7) to solve for variation particle temperature with time. The heat capacity at constant volume, c_v, can be calculated directly from molecular simulation data using equation (IV.12),

$$c_v = \left. \frac{dE_{conf}}{dT} \right|_{N,V} \tag{IV.12}$$

and the diffusivity, *D*, can be determined using equation (IV.1). The temperature profiles obtained by using σ_{sv} as a fitting parameter are reported in Figures IV.15 and IV.16 for 3 nm anatase and rutile nanoparticle sintering with various starting temperatures ranging from 573 K to 2173 K. It is found that the fitted values of σ_{sv} vary between 0.2 and 1.7J/m^2. As the particle size decreases, the percentage of total atoms on the surface increases along with increase in surface curvature, thereby increasing the surface tension. Hence, the surface tension is expected to be higher for smaller particles when compared to the bulk. Also, it has been shown that as the temperature increases, the surface of the particles becomes more agitated and liquid-like, decreasing the surface tension and pushing it towards the liquid surface tension value (σ_l=0.38J/m^2 (Ikemiya, Umemoto et al. 1993; Li and Ishigaki 2002)). This trend is observed in the fitted surface tension values for 3 nm TiO$_2$ particle sintering. The fitted parameter has values close to the bulk solid surface tension at lower temperatures and as the temperature is increased towards the melting point of the particles, the fitted parameter approaches liquid surface tension values. This is graphically represented in Figure IV.17. Thus the overall trend in σ_{sv} is consistent with the picture - higher at lower temperatures and tending to the bulk liquid value at higher temperatures. At this point, neither the peak in the fitted surface tension at about 1000 K for rutile and anatase, nor the shallow minimum at about 1200 K for anatase and at about 1800 K for rutile can be readily explained. The problem with inferring σ_{sv} from agreement with single simulation runs is that the variance in σ_{sv} is unknown. Computing the variance would require multiple simulations, which are currently beyond our computational capacity. It is interesting to note that the fitted surface tension are the correct order of magnitude, comparable to the reported (Ikemiya, Umemoto et al. 1993; Barnard, Zapol et al. 2005) surface tension for bulk TiO_2 (see figure IV.17). This gives credibility to the use of the Meyer method to determine *da/dt* to be used in the model and thus, confirms the inapplicability of the Koch and Friedlander rate law to TiO_2 nanoparticle sintering.

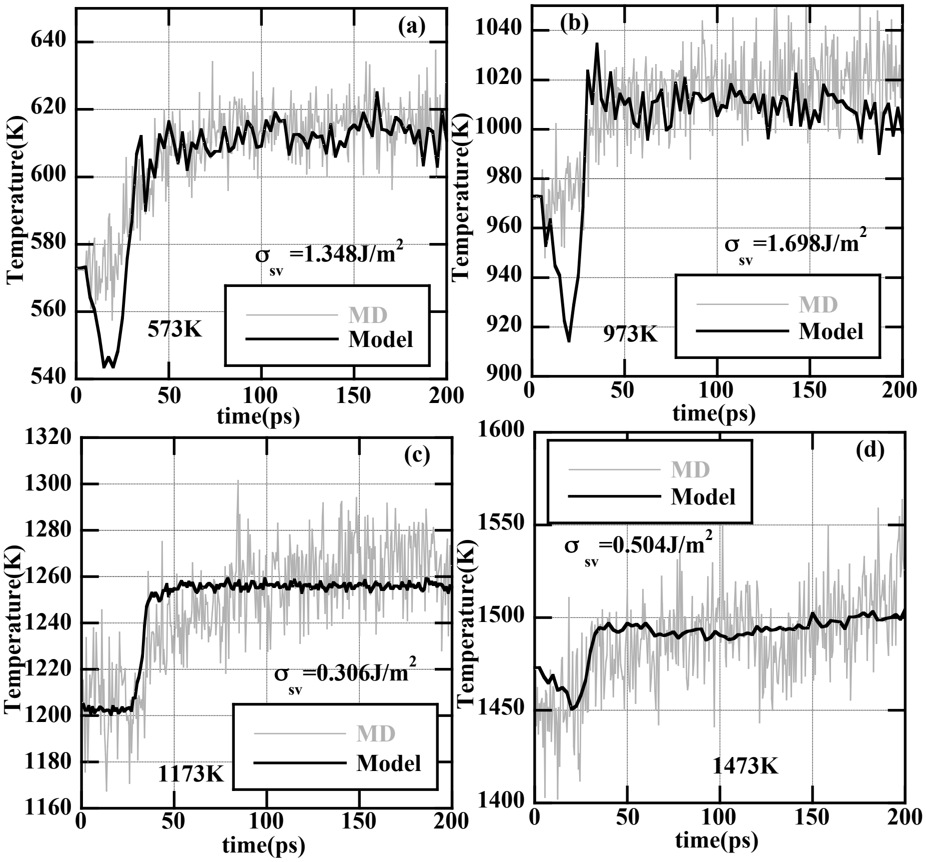

Figure IV.15 Temperature profiles obtained from molecular dynamics simulations (MD) and the model solutions of 3 nm anatase sintering with the starting temperatures of (a) 573 K, (b) 973 K, (c) 1173 K and (d) 1473 K.

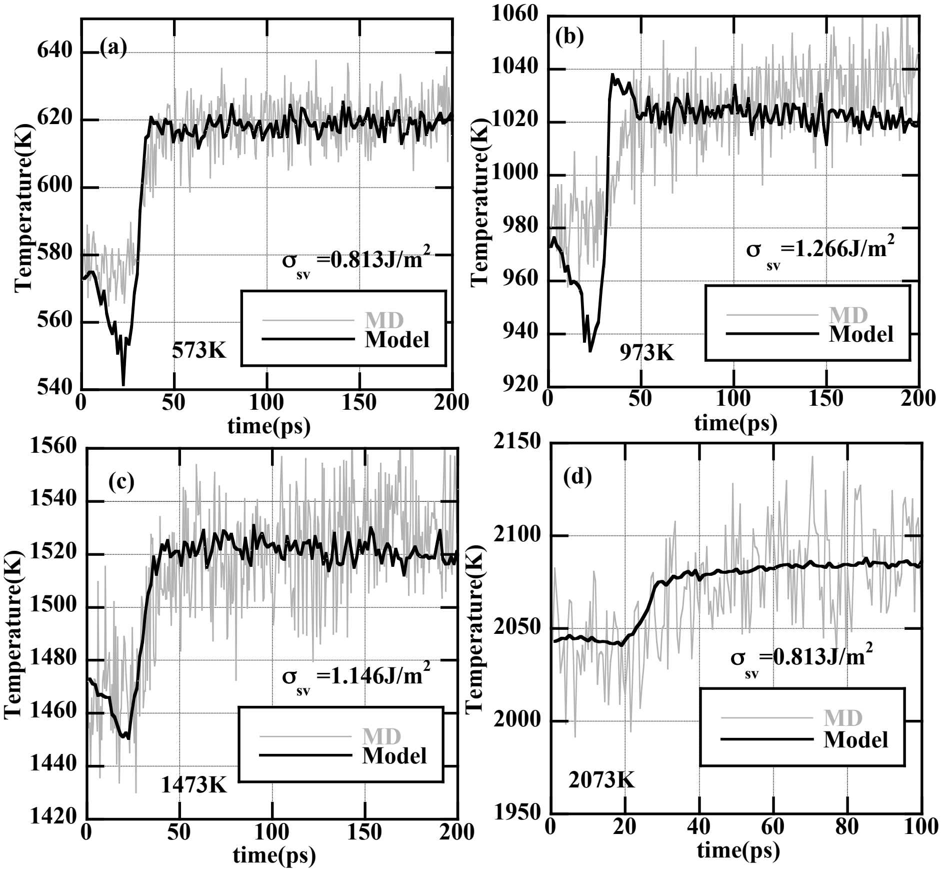

Figure IV.16 Temperature profiles obtained from molecular dynamics simulations (MD) and the model solutions of 3 nm rutile sintering with the starting temperatures of (a) 573 K, (b) 973 K, (c) 1173 K and (d) 1473 K.

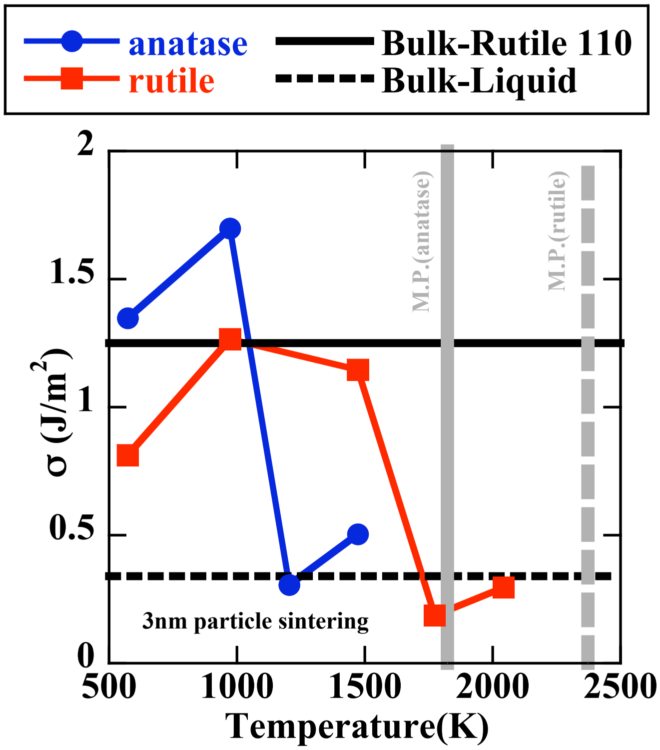

Figure IV.17 Fitted surface tension at various initial temperatures (3 nm anatase and rutile sintering).

IV.4 Conclusions

The melting points of anatase and rutile nanoparticle calculated using molecular dynamics simulations exhibit the expected trend, showing considerable decrease in melting point as the particle size decreases. The calculations from simulations were very close to predictions made using the empirical formula developed by Buffat and Borel (Buffat and Borel 1976) at the particle size of 2.5 nm. For all other particle sizes (3-4 nm), simulations predict higher values of melting temperature than that obtained from Buffat and Borel. The melting point of anatase is found to be lower than rutile at all sizes consistent with the Buffat and Borel correlation.

The surface area of sintering 3 nm anatase and rutile nanoparticles is directly measured using the Meyer method to calculate da/dt. The fact that this measurement, when used in conjunction with the sintering model, gives better results than the Koch and Friedlander (Koch and Friedlander 1990) assumption of linear rate of surface area reduction suggests the Koch and Friedlander assumption may not be valid at the timescales and length scales under consideration. It has been shown (Lehtinen and Zachariah 2001) that the exclusion of heat release resulting from coalescence can lead to the break down of the Koch and Friedlander type coalescence model. The results obtained here corroborate this finding. The fact that anatase and rutile nanoparticles are crystalline and contain charged species seems to play an important role in the deviation of the simple Koch and Friedlander model for TiO_2 nanoparticles. Also, the increased curvature of smaller particles needs to be considered for successful modeling of nanoparticle sintering. For example, Xing and Rosner (Xing and Rosner 1999) have produced results comparable to experiments by using a curvature-dependent solid state diffusion coefficient in their sintering model. By using the surface tension as the only fitted parameter to minimize the error, the sintering model predicts temperature rise during sintering within acceptable limits. The fitted surface tension values follow the correct trends with increase in temperature and were of comparable order of magnitude to those reported for bulk TiO_2.

CHAPTER V

WATER ADSORPTION ON TiO_2 NANOPARTICLE SURFACE

V.1 Introduction

Nanoparticle-water interfaces are common occurrences in nature and in industrial environments. In the interfacial region, water properties and the structure of the nanoparticle both deviate from the characteristic bulk phases (Stumm 1992). This deviation of molecular behavior at the interface has been the impetus to various investigations directed at studying the solid-water interface. TiO_2 nanoparticles are insoluble in water and found various photocatalytic and photovoltaic applications in the aqueous form as slurry or colloids (Ohtani, Okugawa et al. 1987; Augugliaro, Loddo et al. 1995). Molecular dynamics has proven to be an essential technique for the investigation of the fundamentals of adsorption at the atomic level. Most of these studies done using molecular dynamics have been directed towards studying water structure at planar surfaces (Cummings, Predota et al. 2002; Predota, Bandura et al. 2004; Predota, Zhang et al. 2004; Zhang, Fenter et al. 2004). Very few simulation attempts to examine water (or other liquid) adsorption at the surface of nanoparticles (Qin and Fichthorn 2003; Ju 2005) are found in the literature. As shown for TiO_2 nanoparticles in the preceding chapters, all nanoparticles generally have an extremely rough surface. Due to the rough surface, these nanoparticles cannot be considered to be perfectly spherical and the study of water adsorption at their surfaces thereby becomes more complex. In this chapter, the research work performed to study water orientation and structure at the surface of anatase and rutile nanoparticle is described. The motivation behind this work is to understand the behavior of water molecules near the surface of TiO_2 nanoparticles and the variation of their thermodynamic, structural and transport properties with nanoparticle size and environmental conditions. As rutile and anatase are more important polymorphs of TiO_2, due to their large number of applications, brookite is not being considered in the study.

V.2 Simulation Details

V.2.1 Forcefield Selection

The Matsui-Akaogi forcefield (Matsui and Akaogi 1991) has been selected to describe the interactions between Ti and O ions. The details and advantages of this forcefield over the other reported forcefields for TiO_2 have been listed in Chapter II. The forcefield parameters are listed in Table II.2. The Daresbury laboratory molecular dynamics simulation code, DL_POLY version 2.13 (Smith 1987; Smith and Forester 1996), has been used to perform all the simulations on a parallel architecture.

The SPC/E (Berendsen, Grigera et al. 1987) potential is used to model water molecules around the TiO_2 nanoparticles. It is a three-site model with one negatively (q_{OW}=-0.8476) and two positively (q_{HW}=+0.4238) charged sites representing the O and H atoms in the water molecule, respectively. It can be written as

$$U(r_{ij}) = \varepsilon_{ij}\left[\left(\frac{\sigma_{ij}}{r_{ij}}\right)^{6} - 2\left(\frac{\sigma_{ij}}{r_{ij}}\right)^{12}\right] + \frac{q_i q_j}{r_{ij}} \qquad \text{(V.1)}$$

where r_{ij} is the distance between *i* and *j*, and the other parameters are listed in Table V.1. The O-H distance in each water molecule is constrained to 1 Å and the H-O-H angle in each molecule is maintained at 109.47° by constraining the H-H distance to 1.633 Å. DL_POLY uses the SHAKE algorithm (Allen and Tildesley 1997; Frenkel and Smit 2002) to maintain these constrained bonds at the above-mentioned equilibrium values. To model the interactions between the water molecules and the Ti and O ions in the nanoparticles we have used the *ab initio* derived interaction parameters reported by Bandura and Kubicki (Bandura and Kubicki 2003), which suggests that there is not interaction between ions and the water hydrogen atoms except for the electrostatic interactions. The interaction potentials describing the non-coulombic O-O_W interactions, are considered to be the same as O_W-O_W interactions (see Table V.1). The Ti-O_W non-coulombic interactions are represented in a Buckingham form as follows,

$$U(r_{ij}) = A_{ij} \exp\left(-\frac{r_{ij}}{\rho_{ij}}\right) - \frac{C_{ij}}{r_{ij}^6} \tag{V.2}$$

where r_{ij} is the distance between i and j in Å, A_{ij}=28593.02$\frac{\text{kcal}}{\text{mol}}$, ρ_{ij}=0.265 Å and C_{ij}=148.00$\frac{\text{kcal}}{\text{molÅ}^6}$.

Table V.1 SPC/E interaction parameters

i-j	ε_{ij} ***(kcal/mole)***	σ_{ij} ***(Å)***
O_W-O_W	0.15539	3.5532
O_W-H_W	0.000	
H_W-H_W	0.000	

V.2.2 Simulation Method

Constant temperature and constant pressure molecular dynamics simulations where carried out using DL_POLY version 2.13. DL_POLY uses Verlet's leapfrog algorithm in conjunction with multiple timestep method to integrate Newton's laws of motion over time. Each simulation considers a simulation box, which has periodic boundaries in the x, y and z-directions. The size of the box was chosen such that the interaction between the particle and its own image in the neighboring box is negligible. TiO_2 nanoparticles are manufactured either by the dry process or the wet process. The solvent involved in the wet process is generally hydrothermal water (Cheng, Ma et al. 1995; Wu, Long et al. 1999; Yang, Mei et al. 2000; Ovenstone 2001; Yang, Mei et al. 2001; Yang, Mei et al. 2001; Yang, Mei et al. 2002; Yin, Li et al. 2002). Hence, the temperature of 523 K and pressure of 50 Kbar are chosen for simulating hydrothermal conditions (HT). For the simulations at room temperature and pressure (ambient), the values of 300 K and 1 bar are used. In order to generate the initial configuration file, the vacuum equilibrated nanoparticles obtained at the end of the vacuum simulations described in Chapter II are enclosed in a box and then the box is then filled with SPC/E water molecules using a utility provided with DL_POLY. The simulations are repeated for rutile and anatase nanoparticles of 2.5, 3.0 and 4.0 nm diameters at both HT and ambient conditions. For all simulations a timestep of 0.5fs is used and statistical data is collected every 2000 timesteps. After an equilibration period of 250ps, data production runs of 750ps are conducted for all the simulations. The simulation of 4.0 nm rutile nanoparticle involves a system of 22869 atoms, while the simulation of 2.5 nm anatase nanoparticle is the smallest system under consideration containing 5499 atoms. The Ewald summation method (Allen and Tildesley 1997; Frenkel and Smit 2002) is utilized for long-range corrections of electrostatic interactions.

V.3 Results and Discussion

Figure V.1 gives a snapshot of a 3 nm rutile nanoparticle surrounded by water molecules. The simulation box contains 491 TiO_2 units, each containing one Ti and two O ions, and 2756 water molecules, each containing one O and two H atoms.

V.3.1 X-ray Diffraction Patterns

Figures V.2 and V.3 compare the simulated x-ray diffraction patterns of 2.5 and 3.0 nm anatase and rutile nanoparticles in vacuum, under hydrothermal conditions (HT) and at room temperature and pressure (ambient). The simulated X-ray diffraction patterns (see Appendix A) suggest that the nanoparticles do not undergo any phase transformations when immersed in water at HT or ambient conditions. The rutile (110) X-ray diffraction peak, observed at $2\theta=27.5°$, is taller for the particles immersed in water than those in vacuum. Also, the height of rutile (220) peak ($2\theta=55°$) is higher for particle at ambient conditions than that particle in hydrothermal environment, which is in turn higher than that for particle in vacuum. Similarly, for anatase nanoparticles the higher order peaks become taller and narrower. This suggests that when TiO_2 nanoparticles are immersed in water they undergo some degree of structural change. The nanoparticles in water at ambient conditions are more crystalline than those in water at HT, which are more crystalline than those in vacuum.

V.3.2 Coordination Number Distributions

Tables V.2 through V.5 show the percentage distributions of co-ordination numbers of Ti ions in 2.5 nm and 3.0 nm anatase and rutile particles under various conditions. The percentages of 3, 4 and 7 coordinated Ti ions are relatively small in all cases. It can be observed that about 3 to 5% of Ti ions, which were 5-coordinated in vacuum, become 6-coordinated when immersed in water. It should be noted that the coordination between Ti ions and the O atoms in the water molecules is not considered while calculating these coordination numbers for the Ti ions, in order to make them comparable to the vacuum calculations. As the coordination number of Ti ions in bulk anatase and rutile is six, these tables corroborate our previous conclusion that the nanoparticles are more crystalline in water than in vacuum. Calcite nanoparticles show greater crystallinity in water than in vacuum (Kerisit, Cooke et al. 2005). Zhang and co-workers (Zhang, Gilbert et al. 2003) have also reported similar conclusions for ZnS nanoparticles in the same size range.

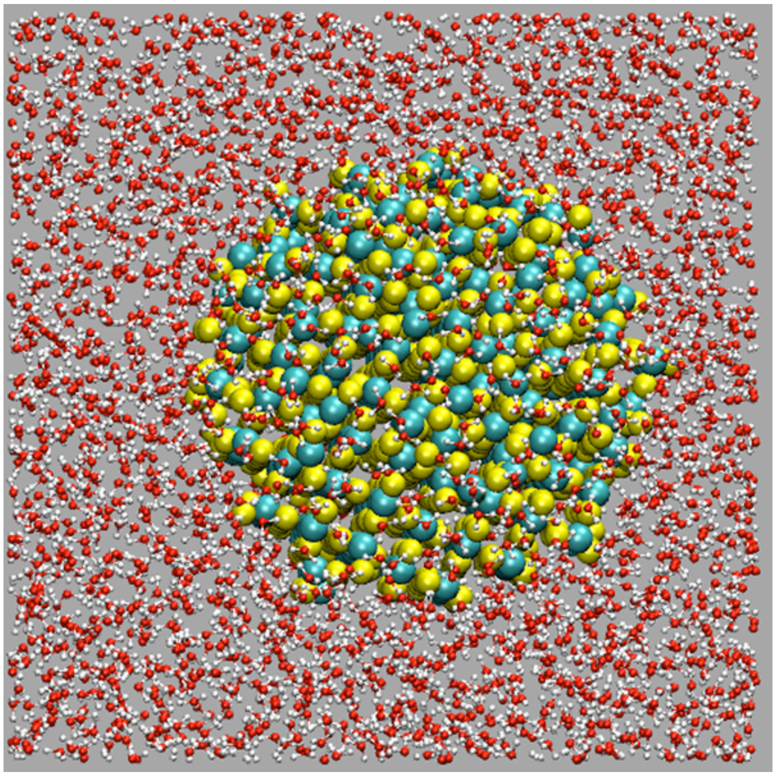

Figure V.1 Snapshot of 3 nm rutile nanoparticle in hydrothermal water (Cyan-Ti ion and Yellow-O ion; Red-Water oxygen; White-Water hydrogen)

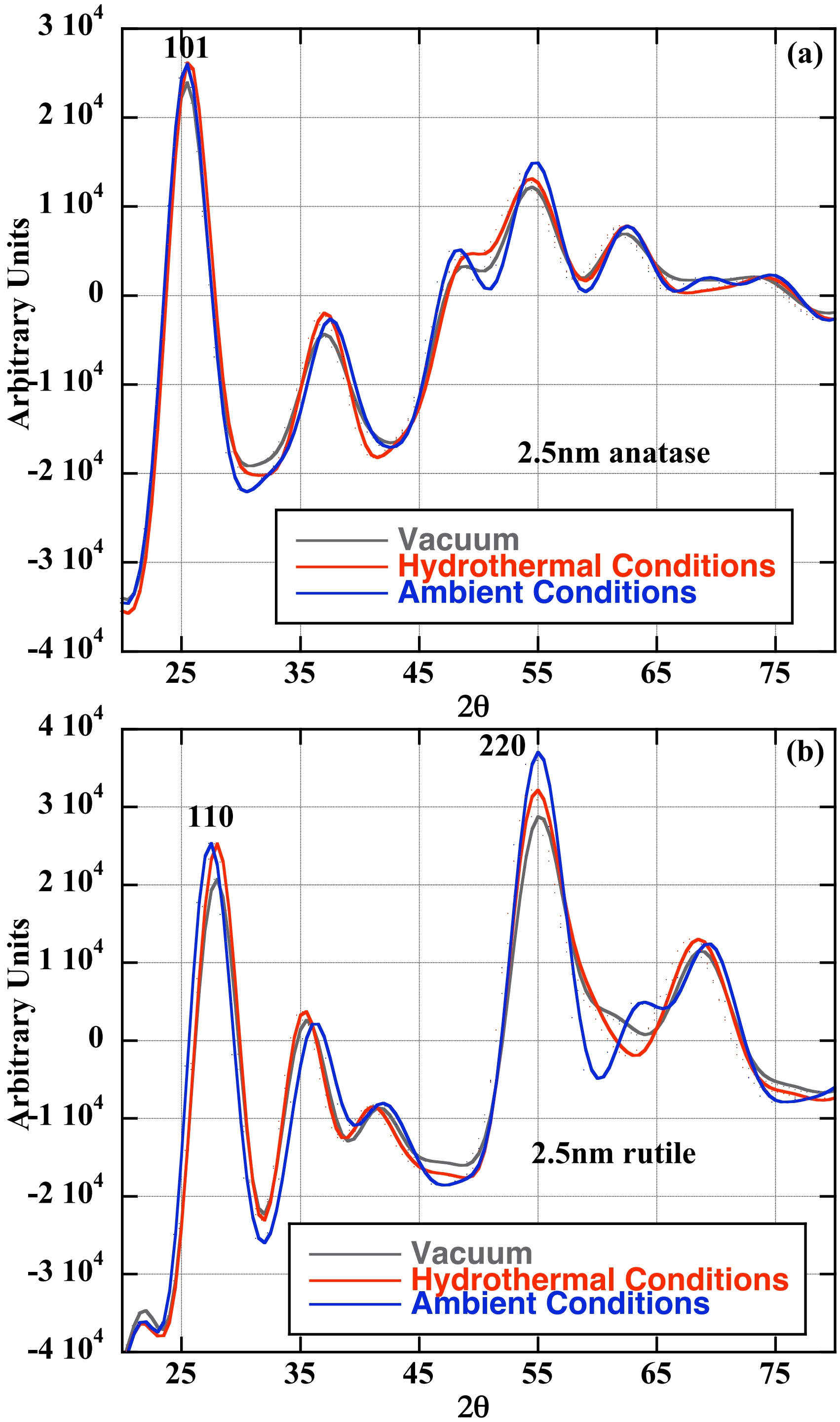

Figure V.2 Simulated X-ray diffraction patterns of 2.5 nm (a) anatase and (b) rutile nanoparticles in vacuum, in hydrothermal water and in water at ambient conditions.

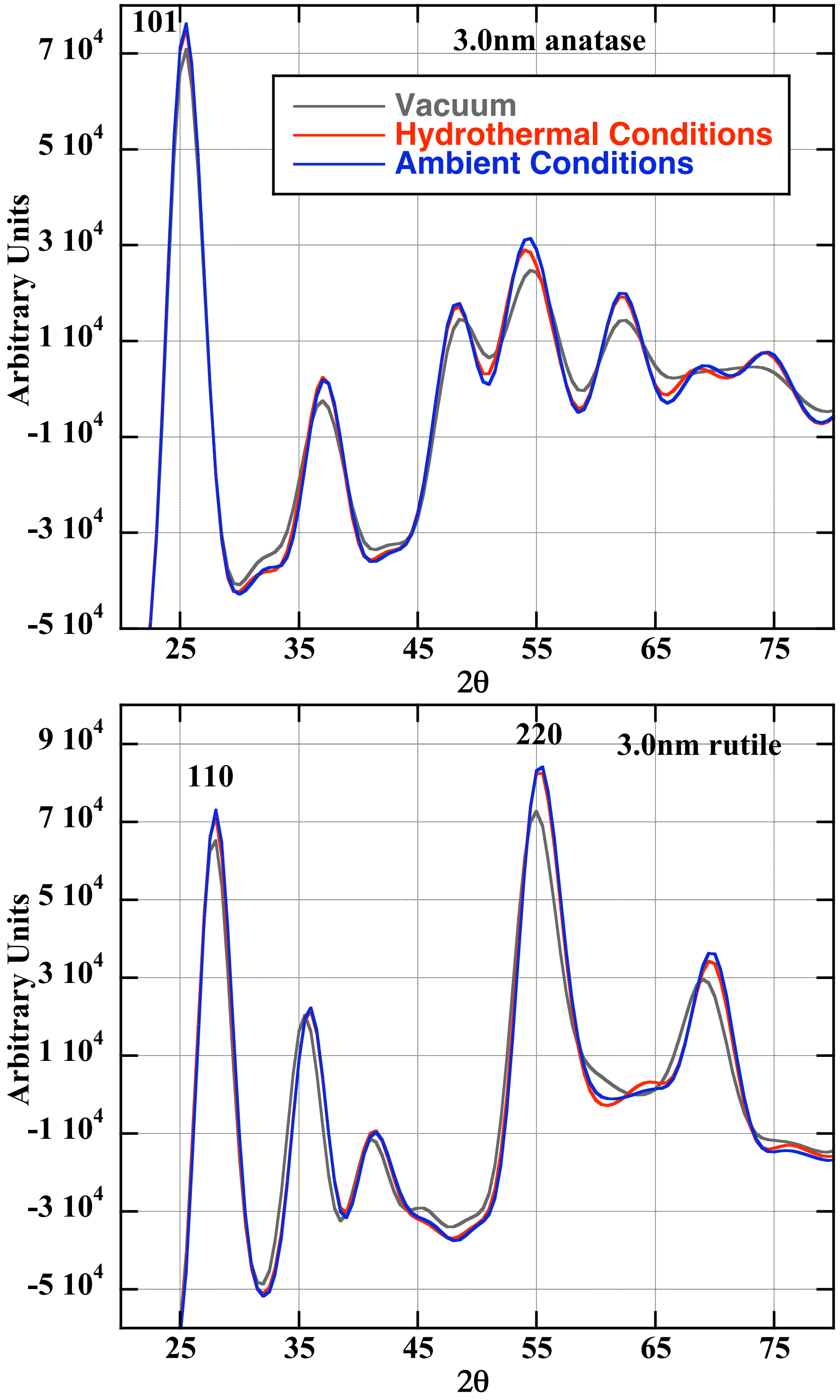

Figure V.3 Simulated X-ray diffraction patterns of 3.0 nm (a) anatase and (b) rutile nanoparticles in vacuum, in hydrothermal water and in water at ambient conditions.

Table V.2 Coordination number distributions of 2.5 nm anatase nanoparticle in vacuum and in water at hydrothermal and ambient conditions.

Co-ordination #	***% in vacuum***	***% at HT***	***% at ambient conditions***
3	0.00	0.06	0.00
4	11.67	11.90	11.60
5	30.35	28.76	28.29
6	57.59	58.52	58.94
7	0.39	0.78	1.16

Table V.3 Coordination number distributions of 2.5 nm rutile nanoparticle in vacuum and in water at hydrothermal and ambient conditions.

Co-ordination #	***% in vacuum***	***% at HT***	***% at ambient conditions***
3	0.01	1.48	1.75
4	11.06	12.73	11.51
5	31.81	25.21	26.93
6	56.75	60.17	59.79
7	0.38	0.41	0.02

Table V.4 Coordination number distributions of 3.0 nm anatase nanoparticle in vacuum and in water at hydrothermal and ambient conditions.

Co-ordination #	***% in vacuum***	***% at HT***	***% at ambient conditions***
3	0.01	0.09	0.24
4	10.09	11.44	10.94
5	27.41	21.78	21.32
6	61.60	66.02	66.90
7	0.89	0.68	0.60

Table V.5 Coordination number distributions of 3.0 nm rutile nanoparticle in vacuum and in water at hydrothermal and ambient conditions.

Co-ordination #	***% in vacuum***	***% at HT***	***% at ambient conditions***
3	0.01	0.21	0.20
4	8.88	9.47	9.65
5	25.36	23.00	22.86
6	65.48	67.24	67.18
7	0.27	0.08	0.11

V.3.3 Density profiles

Figure V.4 shows the density profile of water at HT around the nanoparticle, with respect to the center of mass of the particle. There is no significant increase in water density around the particles suggesting that the particles are not strongly hydrophilic. The broadness of the density peak is due the fact that the surface of the nanoparticle is very rough. The rough nanoparticle surface also explains the apparent penetration of water molecule into the nanoparticle. Due to the rough nature of the nanoparticle surface, the density profile determined with respect to the center of mass of the nanoparticle cannot be compared to the water density profile near a planar surface. In fact, these profiles cannot be compared with each other with confidence as the surface roughness of the nanoparticles varies from particle to particle.

In order to better understand the arrangement of water molecules near the nanoparticle surface and to overcome the problem of surface roughness, we determine the water density with respect to the surface ions. Figure V.5 shows the number of water oxygens when calculated from the outermost Ti ions on the nanoparticle surface. Two distinct peaks of water oxygens are observed at 2.1 Å and 3.9 Å respectively. For all sizes of nanoparticles considered, the first peak for rutile is taller than the first peak for anatase and the second peak for anatase is taller than the second peak for rutile, in both ambient and hydrothermal conditions. Also, the peaks at ambient conditions are taller and narrower for the same size and phase of nanoparticles, suggesting stronger adsorption and better ordering as compared to the hydrothermal conditions.

Similarly, Figure V.6 shows the number of water hydrogens calculated from the outermost O ions on the nanoparticle surface. In the water hydrogen-surface O profiles, two significant peaks are observed at 1.8 Å and 3.1 Å from the surface O ions. Again, the first peak is taller for rutile and second peak is taller for anatase particles of the same size. Since the relative positions of the surface Ti and O ions vary considerably across the rough nanoparticle surface, we cannot directly superimpose the oxygen and hydrogen profiles. In order to achieve this, we had to determine the water distribution profile from the nanoparticle surface without biasing between the surface Ti and O ions. Hence, we determined the three nearest surface ions (denoted as A, B and C) from each water molecule, and then calculated the minimum distance between the water molecules and the triangle defined by these three ions, referred to subsequently as the triangle ABC. Using these distances we plot the water distribution profiles shown in Figure V.7. The ordering of water molecules is prominent only in the first 6 Å from the nanoparticle surface, beyond which the oscillations quickly damp out. In all simulations, independent of size, phase and environmental conditions, three distinct water oxygen peaks are observed around the nanoparticles at 2.1 Å, 2.7 Å and 4.3 Å, respectively. It is also found that there are three hydrogen peaks are at 1.7 Å, 2.8 Å and ~5 Å. It may seem like there are three hydration shells surrounding the nanoparticles. But it is highly improbable for the first two oxygen peaks to be separated by a distance of only 0.6 Å. Hence, there are two hydration shells surrounding the TiO_2 nanoparticles and the water molecules within this first hydration shell interact in two different ways with the nanoparticle surface depending upon the local environment, that is, depending upon whether it is relative close to a Ti ion or an O ion from the nanoparticle surface. Just by examining the heights of the water O-surface peaks, the orientational preference is inverted when conditions are changed from hydrothermal to ambient. The water molecules in the second hydration shell are far enough from the nanoparticle to indicate any such multiple orientational preferences.

In order to differentiate between the two orientations in the first hydration shell, we have defined different regions on the water distribution profile from the surface. All water molecules with oxygen atoms within the first minima (~2.5 Å) are considered to be in region 1, all those between the first and the second minima (~3.2 Å) are said to be in region 2. All water molecules with oxygen atoms between 3.2 Å and 5.7 Å from the surface, that is, in the second hydration shell, are referred to in region 3.

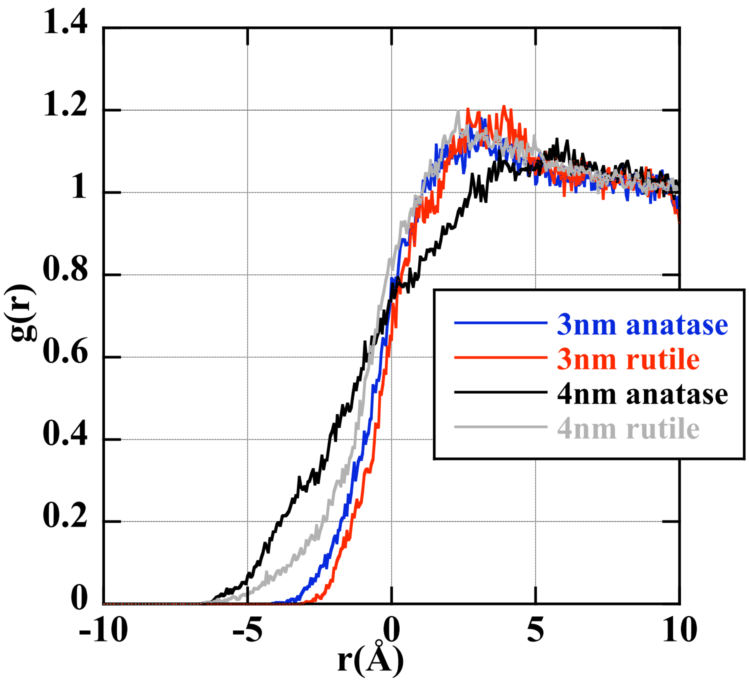

Figure V.4 Density profiles of water molecules around 3 nm and 4 nm anatase and rutile nanoparticles at hydrothermal conditions.

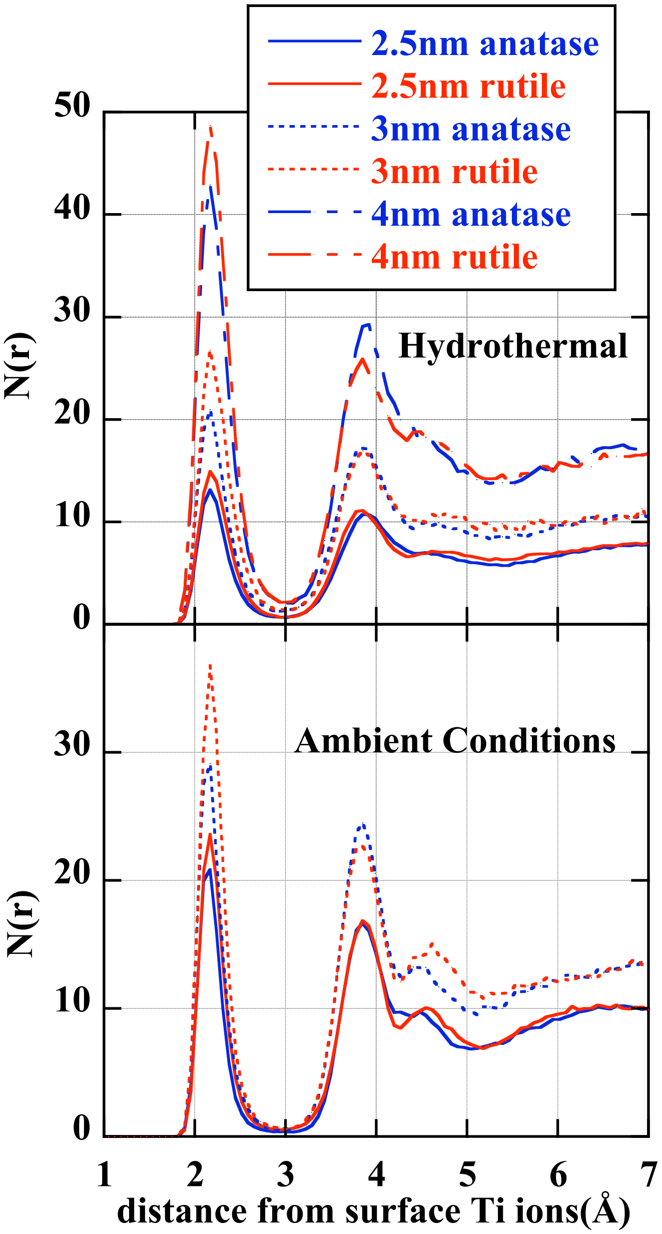

Figure V.5 Density profile of water oxygens from the surface Ti ions at hydrothermal and ambient conditions

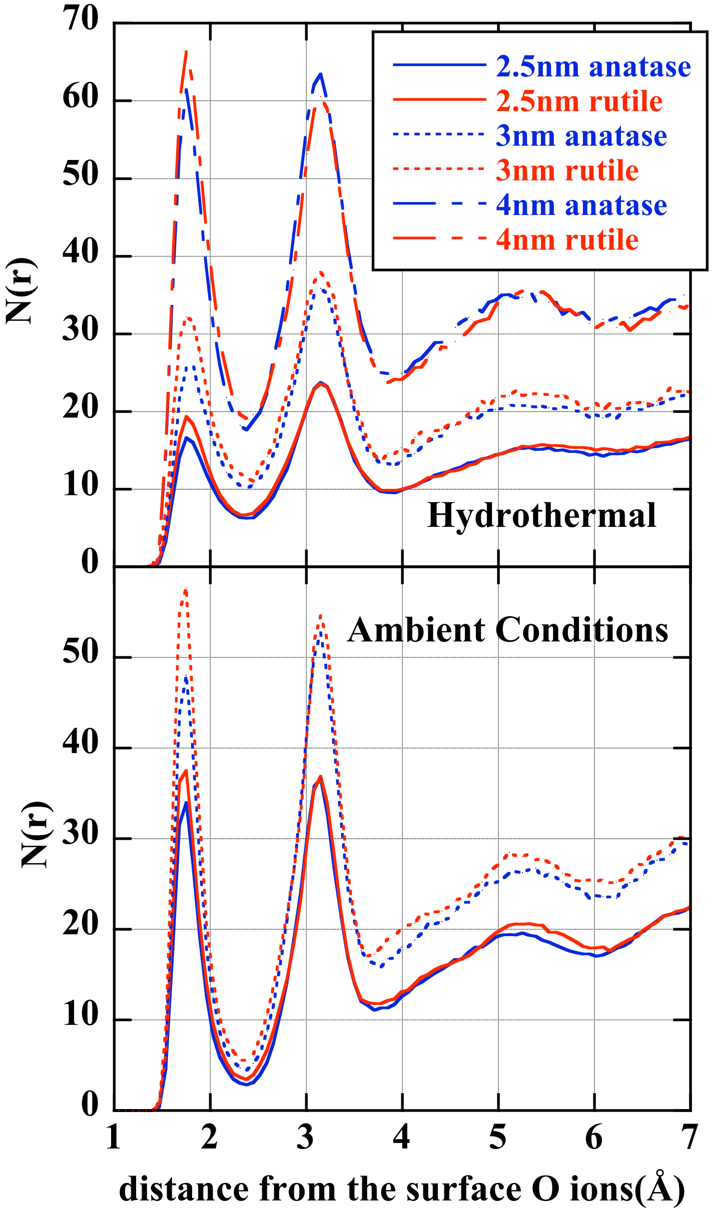

Figure V.6 Density profile of water hydrogens from the surface O ions at hydrothermal and ambient conditions

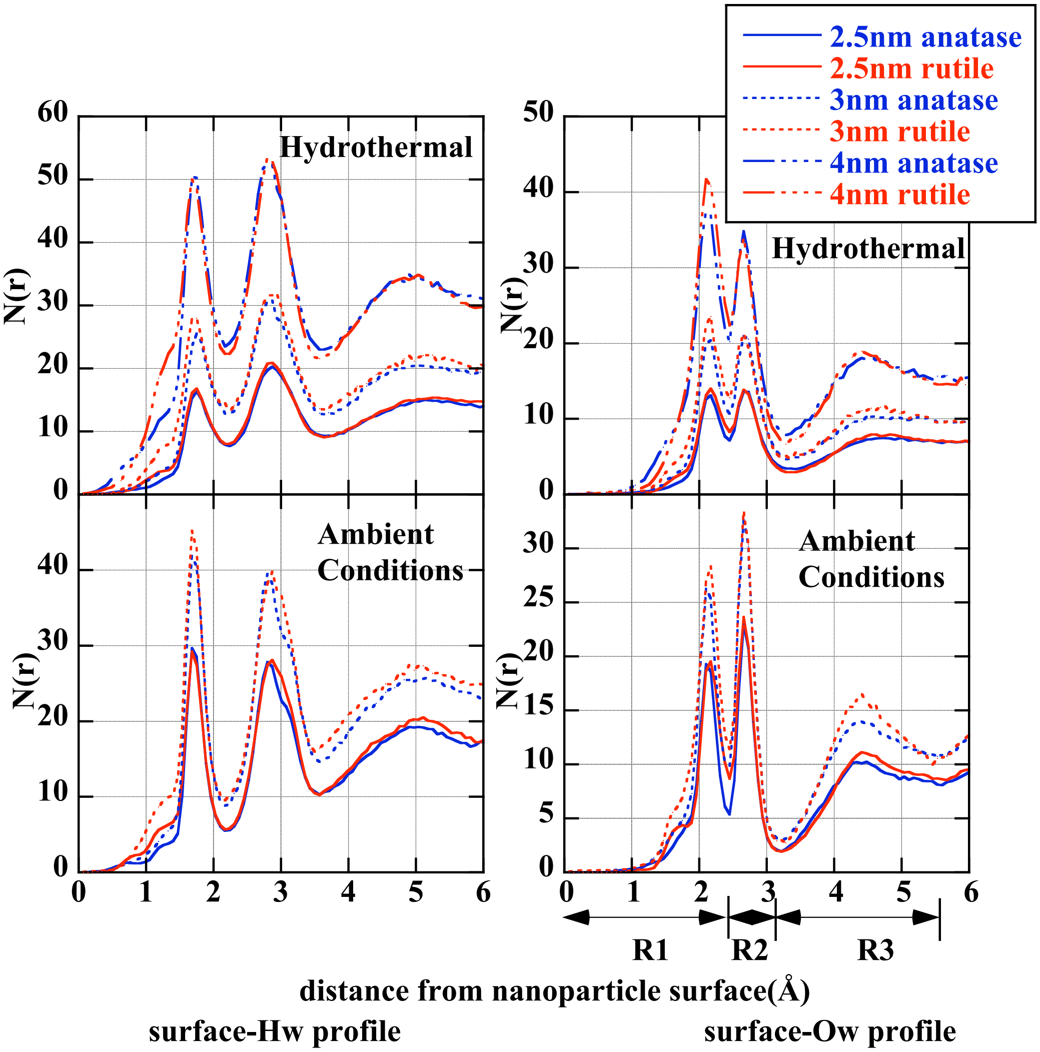

Figure V.7 Density profiles of water H and water O from the nanoparticle surface

V.3.4 Water Coverage

Water coverage has been defined as,

$$\text{coverage} = \frac{\text{Number of water molecules in the first hydration shell}}{\text{Nanoparticle surface area}} \qquad \text{(V.3)}$$

The solvent accessible surface area of the nanoparticles is calculated for all the simulations using the method proposed by Meyer (Meyer 1988). This method is chosen because it is simpler and computationally less intense and yet manages to give results comparable to more complex methods reported in the literature (Gavezzotti 1985; Perrot, Cheng et al. 1992; Legrand and Merz 1993). The details about calculating the surface area of the nanoparticle using the Meyer method have been reported in Chapter IV. By counting the number of water molecules within the first hydration shell, we can calculate the number of water molecules physically adsorbed on the nanoparticle surface. Knowing the solvent accessible surface area of the nanoparticles the water coverage is determined and plotted for various nanoparticle diameters in Figure V.8. The water coverage increases with increase in particle size for rutile and anatase nanoparticles and is always higher for rutile than anatase suggesting that rutile nanoparticles are slightly more hydrophilic than anatase nanoparticles at all particle sizes and environmental conditions. As the particle size increases, the percentage of Ti ions that are 6-coordinated also increases. Thus the larger particles have a higher percentage of crystallinity than the smaller ones. Also, the curvature of the surface decreases considerably with increase in particle size, tending more and more towards planar surfaces. The coverage is found comparable in magnitude to that of a rutile (110) surface under ambient conditions reported by Predota and coworkers (Predota, Bandura et al. 2004).

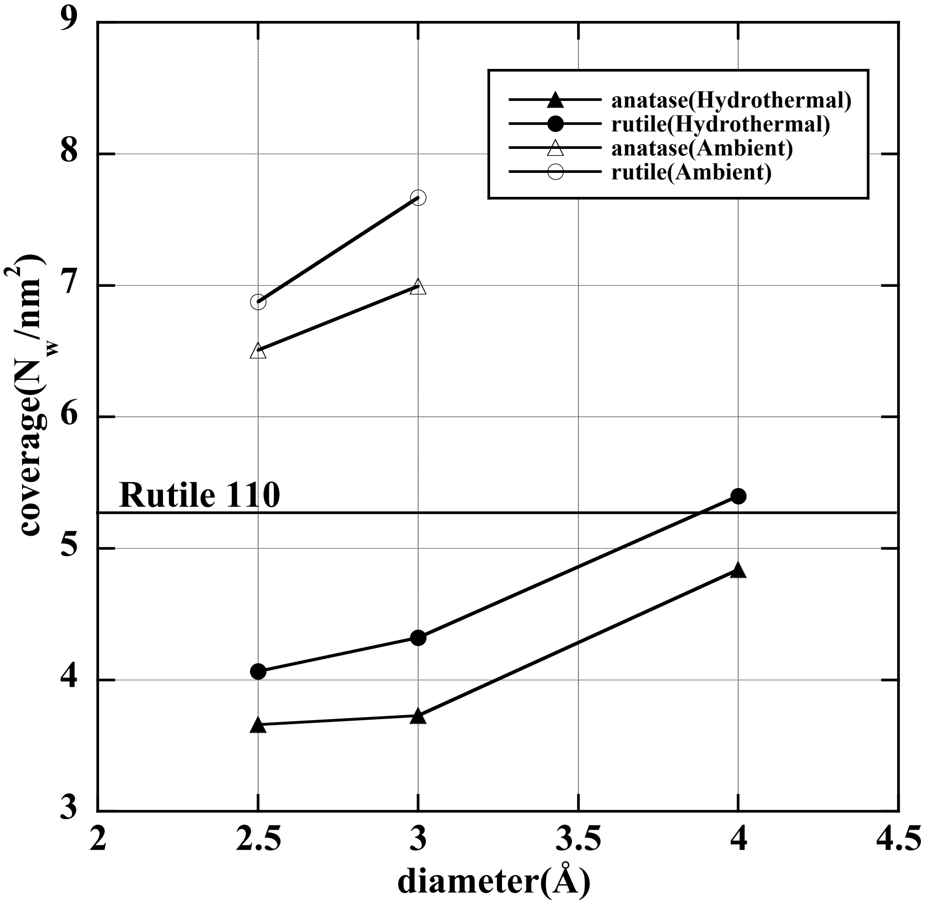

Figure V.8 Water coverage with changing particle diameter at hydrothermal and ambient conditions.

V.3.5 Water Residence Time

In order to investigate the strength of water adsorption at the metal oxide nanoparticle surface, we calculated the time correlation function for the water molecules within the first hydration layer from the nanoparticle surface. The residence time correlation function is defined as (Impey, Madden et al. 1983),

$$\langle R(t) \rangle = \left\langle \frac{1}{N_0} \sum_{i=1}^{N_t} \theta_i(0)\theta_i(t) \right\rangle \tag{V.4}$$

where N_0, N_t are the number of water molecules within the first hydration layer from the surface at t=0 and t=t; and $\theta_i(t)$ is so defined that it equals 0 if the ith water molecule is not in the first hydration shell at time t and it equals 1 if the ith water molecule is in the first hydration shell at time t. The residence time correlation functions are plotted against simulation time in Figure V.9. It is clear that the particle size or phase does not affect the time correlation function significantly but the environmental conditions play a vital role in determining the strength of water adsorption. The residence time can be determined by integrating $\langle R(t) \rangle$,

$$\tau = \int_0^\infty \langle R(t) \rangle \tag{V.5}$$

The approximate value of the residence time is obtained by fitting the time correlation function to an exponential function.

$$\langle R(t) \rangle \approx \exp\left(-\frac{t}{\tau}\right) \tag{V.6}$$

The residence time of water molecules at the surface of TiO_2 nanoparticles is found to be ~500ps at ambient conditions and ~50ps under hydrothermal conditions. Thus, water molecules stay at the surface about 10 times longer at ambient conditions than at HT and so they are strongly adsorbed on the surface at room temperature and pressure.

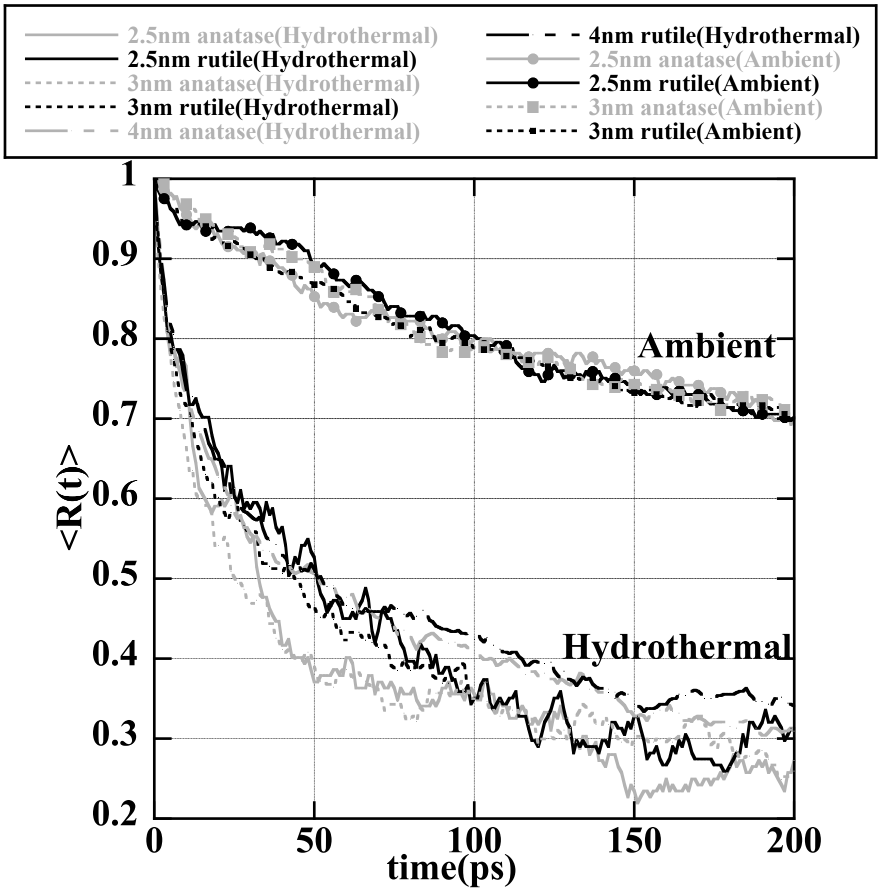

Figure V.9 Time correlation functions of anatase and rutile nanoparticles at ambient and hydrothermal conditions.

V.3.6 Water Orientation Distributions

The orientation of a water molecule at an interface has frequently been discussed by considering four vectors bound to the water molecule (Jedlovszky, Vincze et al. 2002). These vectors are the dipole vector ($\bar{r}_{dp}$), the normal vector ($\bar{r}_n$), the vector joining the two hydrogen atoms of the water molecule ($\bar{r}_{HH}$) and the vector from the oxygen atom towards any one of the two hydrogen atoms in the water molecule ($\bar{r}_{OH}$). For a planar surface the orientation is characterized by the angles between these four vectors and the vector perpendicular to the planar surface, and are denoted by the Greek letters α, β, γ and χ, respectively. In order to account for the non-planar nature of the surface under consideration, these angles have been redefined as the angles between the four vectors bound to the water molecule ($\bar{r}_{dp},\bar{r}_n,\bar{r}_{HH},\bar{r}_{OH}$), and the vector ($\bar{r}_x$) originating from the oxygen atom in the water molecule and normal to the triangle ABC, formed by the three surface ions nearest to the water molecule under consideration. It should be noted that the vectors $\bar{r}_n$ and $\bar{r}_{HH}$ can be equally directed in two opposite directions unlike the vectors $\bar{r}_{dp}$ and $\bar{r}_{OH}$, and there is no physical way of distinguishing between them. Hence, the angles β and γ can only vary between 0° and 90°, while the angle α and χ varies between 0° and 180°. In order to determine the orientational preference of the water molecules, the probability density functions of the cosines of the angles α, β, γ and χ in the regions 1, 2 and 3 are determined. Note that cos β and cos γ will lie between 0 and 1, cos α and cos χ will vary between -1 and 1.

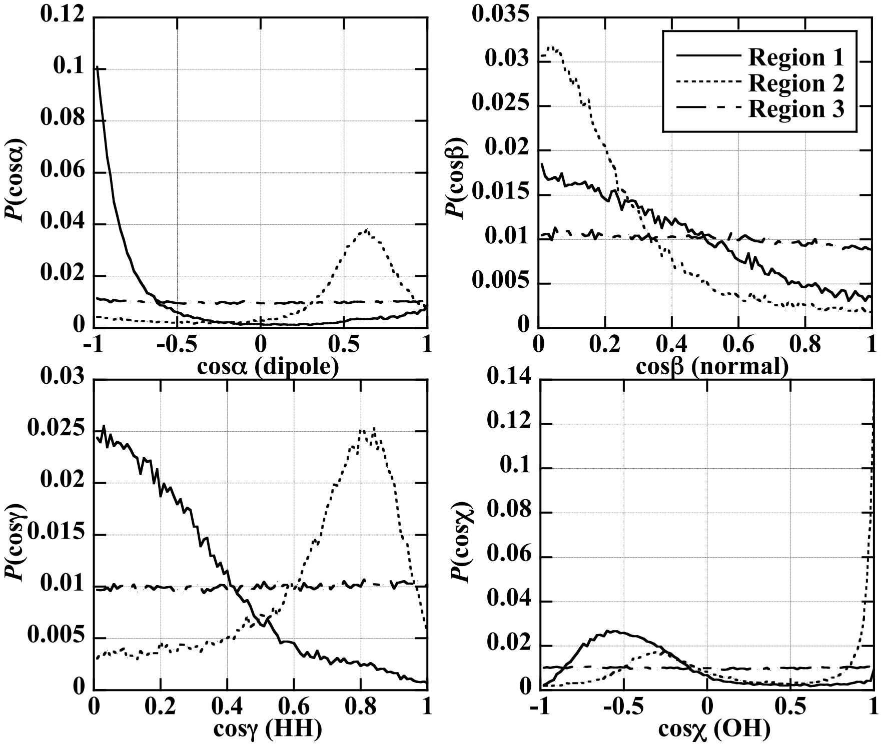

Figure V.10 Probability density functions of angles α,β,γ and χ for 3 nm rutile nanoparticle at hydrothermal conditions.

Figure V.10 shows these probability density functions of angles α, β, γ and χ for 3 nm rutile in various regions at HT. As per the definitions of these regions (see section V.3.3), region 1 is the closest to the nanoparticle surface followed by region 2, which is then followed by region 3. It is found that all probability density functions show similar trends at all phase and sizes at HT.

Region 1:

In this region the most preferred values of α, β, γ and χ are 180°, 90°, 90° and 127°, respectively. This indicates that the water molecules in this region are aligned in such a way that their dipole moment vector is almost parallel to the surface normal, with the oxygen being close to the surface and hydrogen atoms oriented away. The $\bar{r}_{HH}$ vector is also perpendicular to the surface normal confirming this arrangement. Thus, the region 1 consists of water molecules that are interacting with the Ti ions on the nanoparticle surface. The schematic in Figure V.11 gives better interpretation of this orientation.

Region 2:

In region 2, α, β and γ are most likely to be 53°, 90° and 35°, respectively. The angle with the $\bar{r}_{OH}$ vector has high probabilities for two angles, namely, 0° and 109°. This indicates that the water molecules in region 2 have one of their $\bar{r}_{OH}$ vector aligned pointing towards the surface, parallel but opposite to the direction of the surface normal. The plane of the molecules is preferentially perpendicular to the surface. This is depicted as a schematic in Figure V.11.

Region 3:

The probability density functions for all angles are almost flat in the region 3 inferring that there is no preferential orientation of the water molecules in this region, thereby indicating bulk-like behavior.

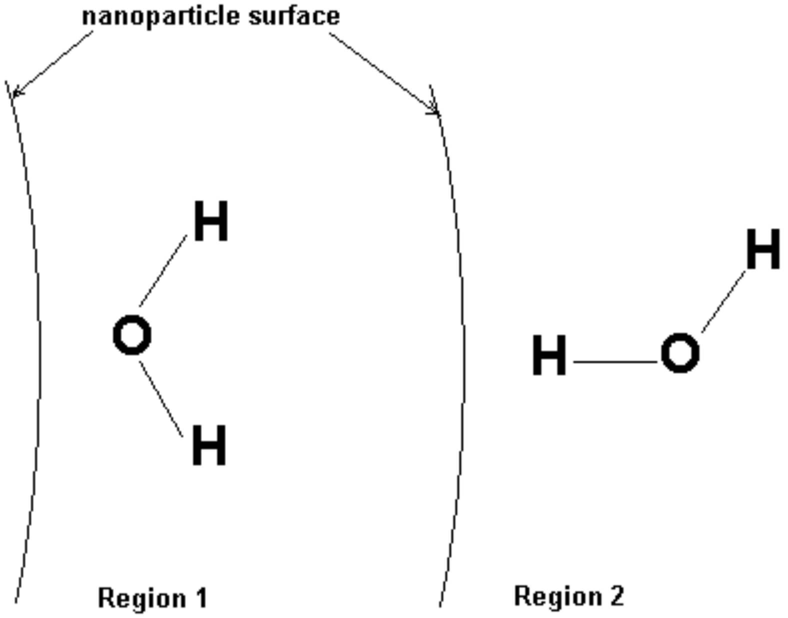

Figure V.11 Schematic representation of preferred water orientations in Region 1 and 2.

The probability density functions of angles α,β,γ and χ for 3 nm rutile at ambient conditions are shown in Figure V.12. They indicate that at room temperature and pressure, the peaks are narrower and taller but their positions remain unchanged. This indicates that the orientations at ambient conditions are similar to HT in the various regions but the preference of these orientations over other possible ones is greatly enhanced.

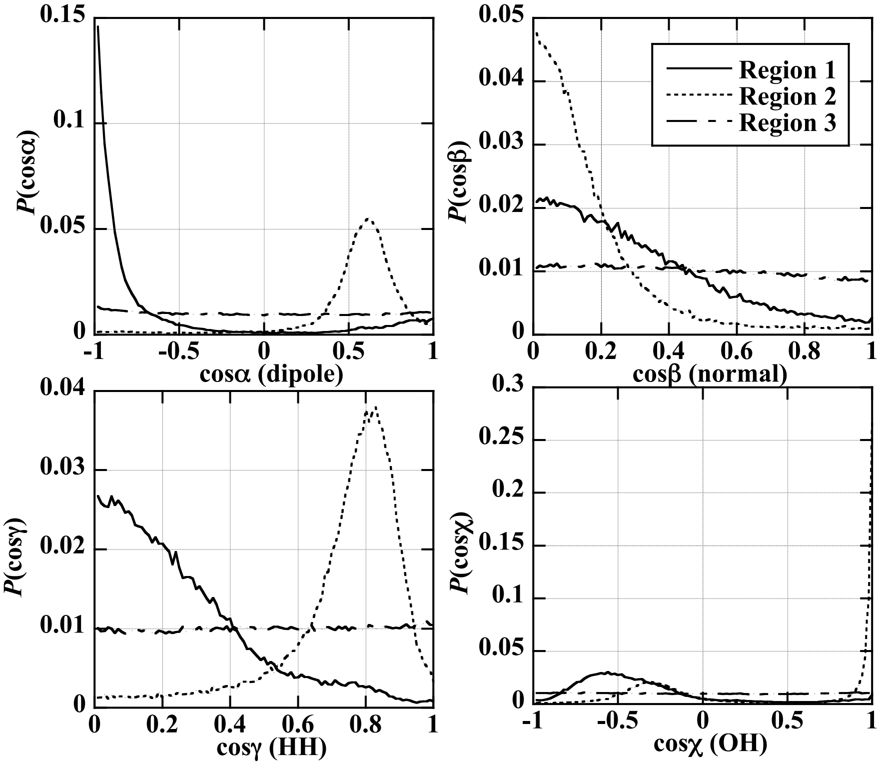

Figure V.12 Probability density functions of angles α, β, γ and χ for 3 nm rutile nanoparticle at ambient conditions.

V.3.7 Bivariate Plots

Although the above mentioned probability distribution functions, give information about the preferential orientation of a single water molecule, their joint statistical distribution cannot be obtained from their individual distribution due to the fact that these angles are not mutually independent (Jedlovszky, Vincze et al. 2002). For example, angles α and β can have some preferential values but we cannot say with certainty that these values appear simultaneously. Hence, in order to get independent molecular directions we define a new angle ϕ, as the angle between the vector $\bar{r}_n$ with the projection of the vector $\bar{r}_x$ in the plane containing the vectors $\bar{r}_n$ and $\bar{r}_{HH}$. The vectors $\bar{r}_{dp}$, $\bar{r}_{HH}$ and $\bar{r}_n$ define the frame of reference. Uniform spatial distribution of water molecules in bulk water would lead to uniform distribution of the angle ϕ and the cosine of the angle α. Hence, joint probability distribution of ϕ and $\cos\alpha$ would provide us information of molecular orientation with greater certainty (Jedlovszky, Vincze et al. 2002). These $P(\cos\alpha,\phi)$ plots are referred to as bivariate joint distribution plots. The bivariate joint distributions in region 1, 2 and 3 for all considered simulations are calculated. The plots for 2.5 nm rutile, 3.0 nm rutile, 3.0 nm anatase at ambient conditions, and 3.0 nm rutile at hydrothermal conditions are presented in Figures V.13, V.14, V.15 and V.16, respectively. Other plots are omitted for brevity. As all region 3 plots indicate uniform distributions, hence only one representative region 3 plot is included in Figure V.17. It should also be noted that the scale used for Figure V.17 is 10 times smaller than that used for other bivariate joint distribution plots reported here.

It is observed from Figure V.13 through V.16 that in region 1, the water molecules prefer a value of α to be 180° but no particular preference for ϕ. The plots of region 2 shows that there is strong orientational preference for α and ϕ to be ~53° and ~90°, respectively in this region. This infers that water molecules are aligned with one of their hydrogen atoms pointed towards the surface with the $\bar{r}_{OH}$ perpendicular to the surface and the molecular normal being parallel to the surface. Thus, the water molecules in region 2 have stronger orientation preference than those in region 1.

Comparing Figures V.13 and V.14, it seems that the orientational distribution is not dependent on particle size. Similar conclusions can be drawn about the phase dependence of orientational distributions by comparing plots in Figures V.14 and V.15. Upon close examination of Figures V.14 and V.16, it can be found the orientational dependence in region 1 and 2 is enhanced when the environmental conditions are changed from hydrothermal to ambient.

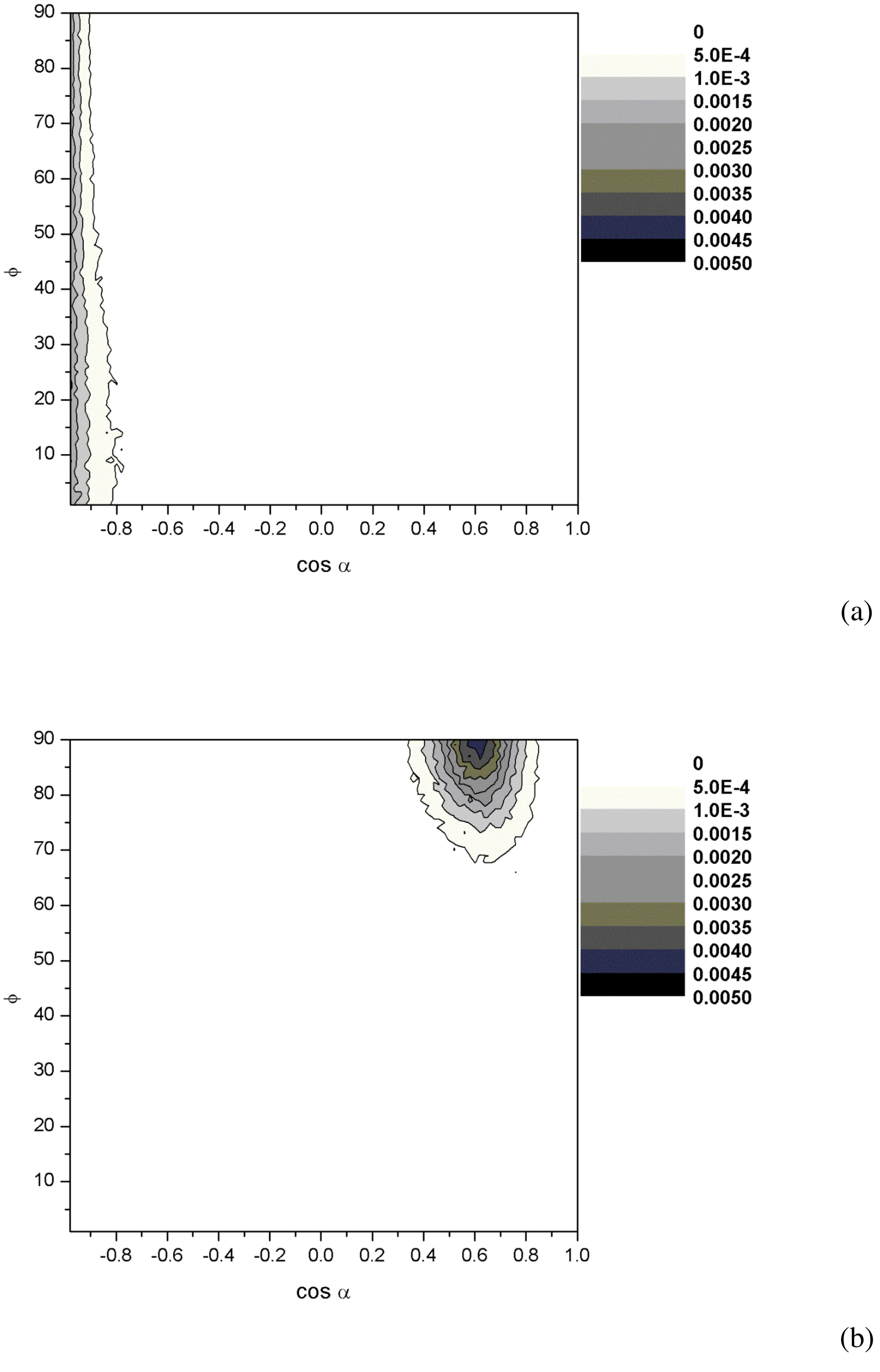

(a)

(b)

Figure V.13 Bivariate plots for 2.5 nm rutile nanoparticle in water at ambient conditions: (a) Region 1, (b) Region 2.

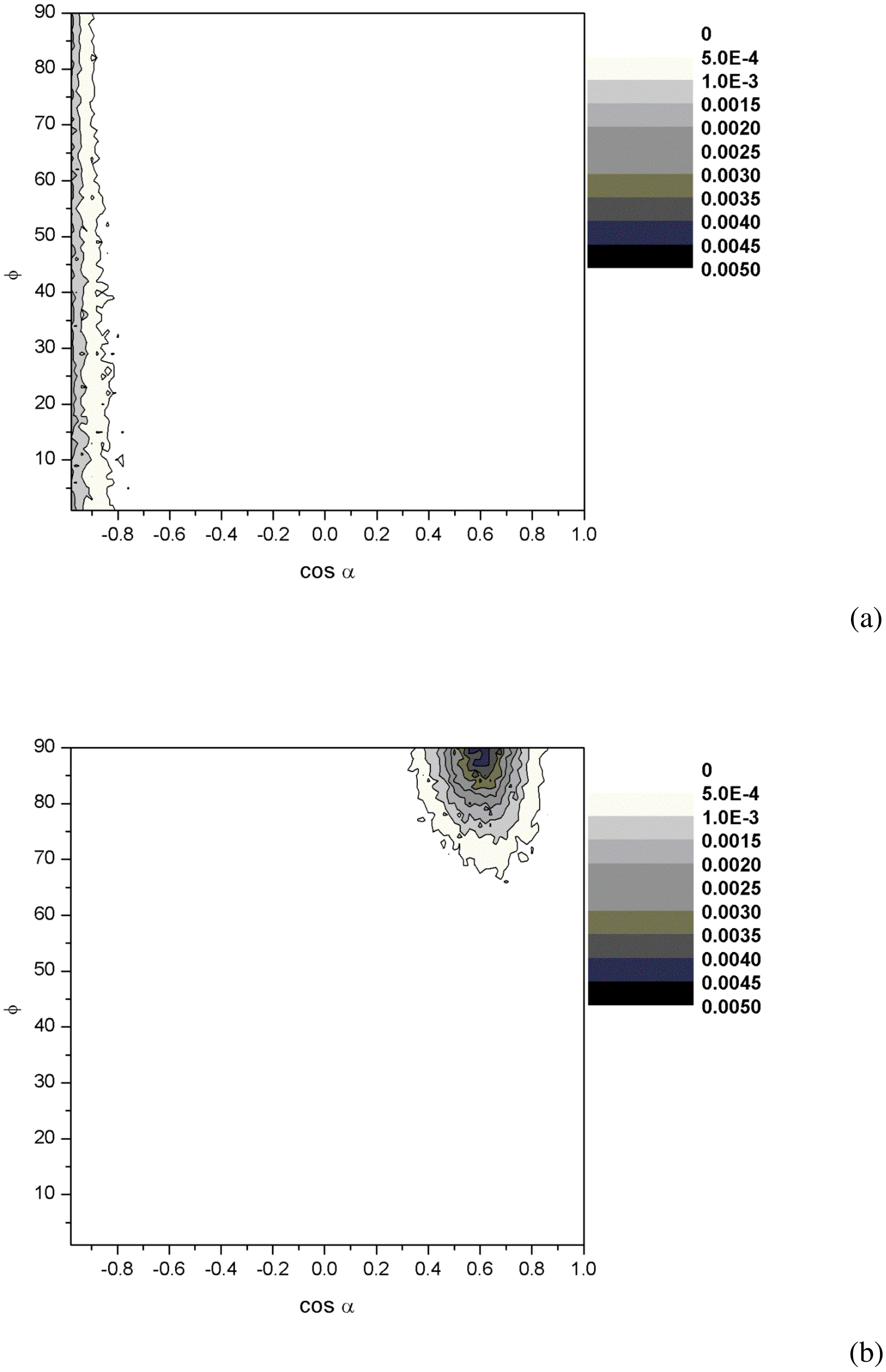

Figure V.14 Bivariate plots for 3.0 nm rutile nanoparticle in water at ambient conditions: (a) Region 1, (b) Region 2.

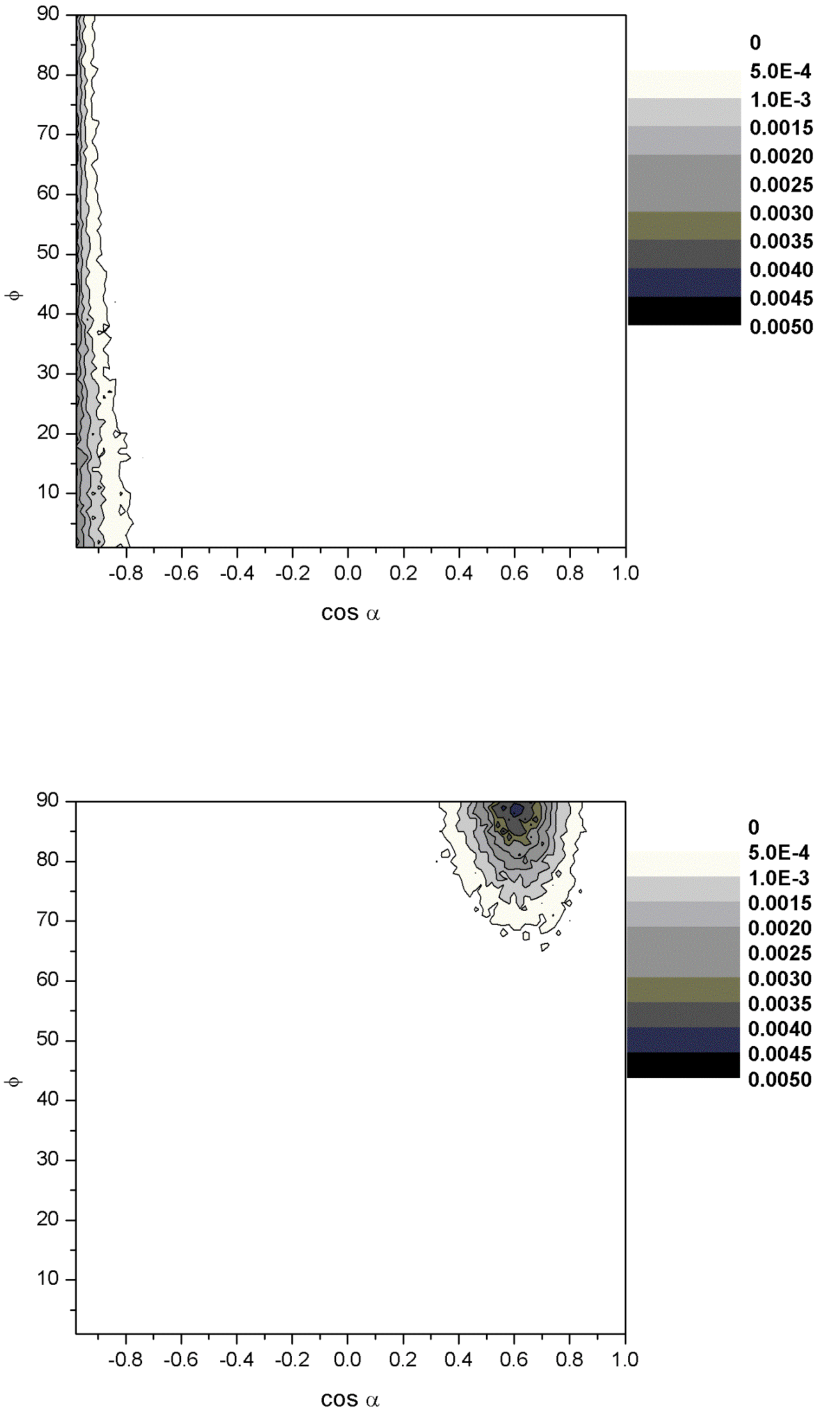

(a)

(b)

Figure V.15 Bivariate plots for 3.0 nm anatase nanoparticle in water at ambient conditions: (a) Region 1, (b) Region 2.

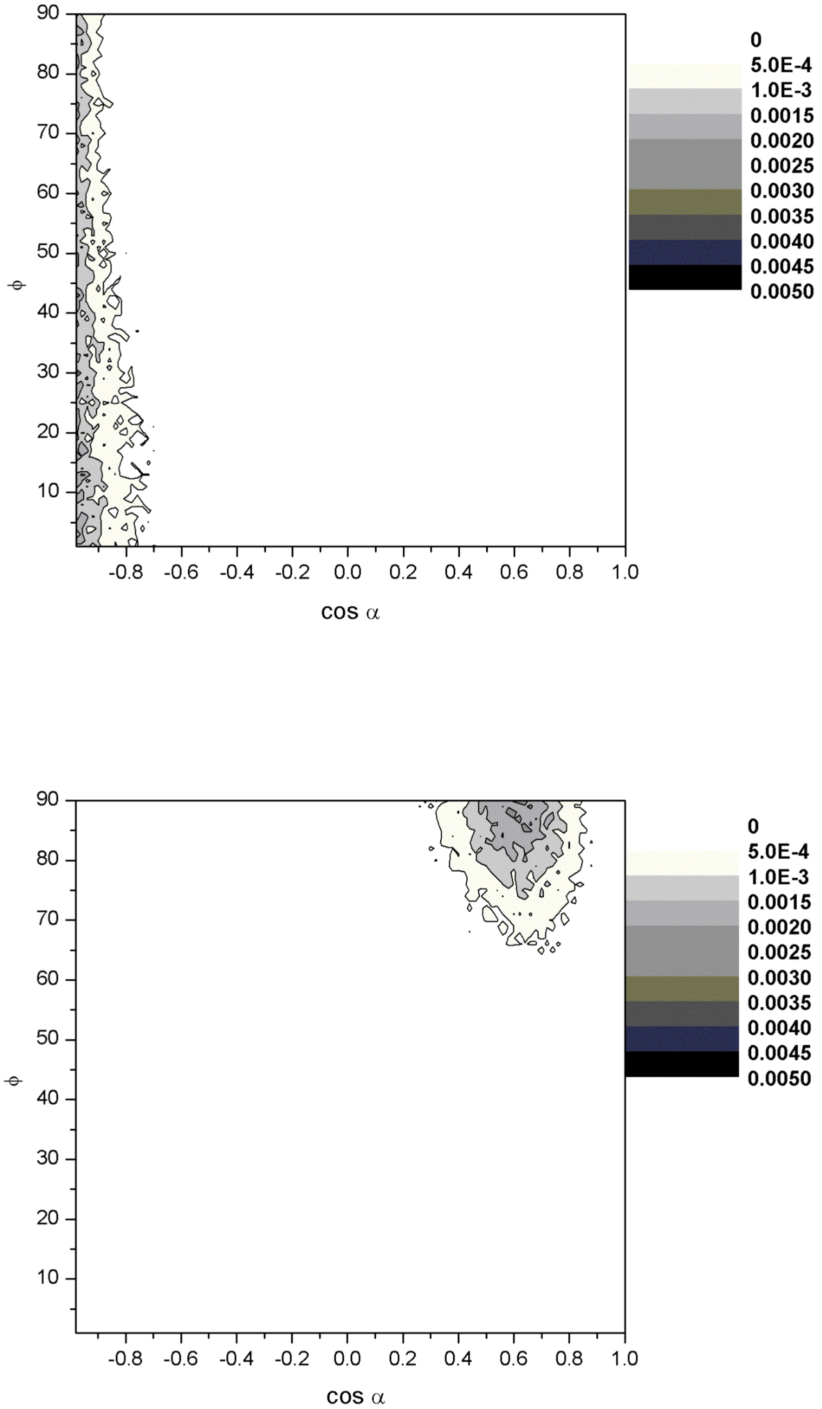

(a)

(b)

Figure V.16 Bivariate plots for 3.0 nm rutile nanoparticle in water at hydrothermal conditions: (a) Region 1, (b) Region 2.

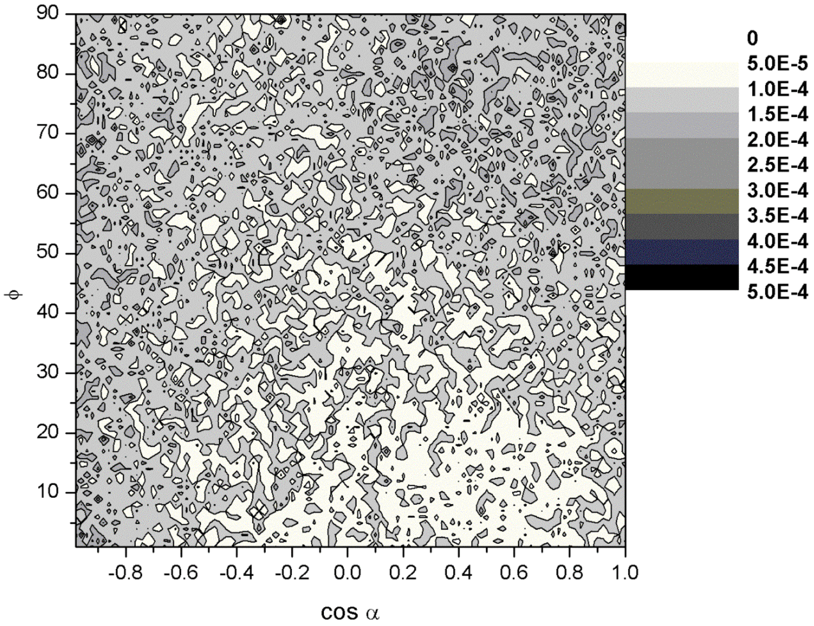

Figure V.17 Bivariate plots for 3.0 nm rutile nanoparticle in water at ambient conditions: Region 3.

V.4 Conclusions

This research work investigated the adsorption of molecular water on the surfaces of anatase and rutile nanoparticles. It was found that the rutile nanoparticles were more hydrophilic than anatase nanoparticles of the same size, both at ambient conditions (T=300 K,P=1bar) and under hydrothermal conditions (T=523 K,P=50 Kbar). When nanoparticles are inserted in water, they undergo structural modification but no phase transformation occurs over the time scales accessible via molecular dynamics simulations. As a result of this modification, we do observe phase enhancement or greater crystallinity. This is indicated by a higher percentage of 6-coordinated Ti ions in the nanoparticle in water and taller/narrower peaks in the simulated X-ray diffraction pattern. The number of water molecules per unit surface area of the nanoparticles (coverage) increased with the size of the nanoparticles and with the percentage crystallinity of the particle. The coverage for rutile is always greater than anatase nanoparticle of the same size, corroborating our previous conclusion. Also, the water molecules are more strongly adsorbed on the nanoparticle surface at room temperature than under hydrothermal conditions.

Two hydration layers were found to be present around the nanoparticles. The first hydration layer has water molecules with two distinctly different orientation preferences. No such orientational preference is observed in the second hydration layer. The interactions between the water molecules in the first hydration layer and the nanoparticle surface are dependent on the local environment of the water molecule under consideration, that is, its proximity to a Ti or O surface ion. The bivariate joint distribution plots also depict the probabilistic preferences of these two orientations.

CHAPTER VI

PHASE TRANSFORMATIONS DURING TiO_2 NANOPARTICLE SINTERING

VI.1 Introduction

Phase transformation in TiO_2 has been extensively studied from both scientific and technological points of view (Kumar, Keizer et al. 1992; Cerrato, Marchese et al. 1993; Kumar 1995; Ahn, Park et al. 1998; Suresh, Biju et al. 1998; Nair, Nair et al. 1999; Gouma and Mills 2001; Lu, Zhang et al. 2003; Hu, Tsai et al. 2003-a; Borkar and Dharwadkar 2004; Kim, Kim et al. 2005; Machado and Santana 2005; Bakardjieva, Stengl et al. 2006). TiO_2 occurs naturally in rutile, anatase and brookite crystal phases or polymorphs. Rutile is the only stable phase in the bulk form, and bulk brookite and anatase are metastable and transform irreversibly to rutile upon heating. But it has been argued often that the phase stability is different at the nanoscale. Anatase is the reported stable phase when the particle size is only few nanometers. Many attempts have been made to understand and control the anatase to rutile transition as these phases have extremely different physical properties in the nanometer range. For example, nanoanatase is more photocatalytically active than nanorutile (Wahi, Yu et al. 2005; Panpranot, Kontapakdee et al. 2006). Hence, it is necessary to maintain the anatase phase by preventing its transition to rutile in order to sustain high photocatalytic activity over long periods of time.

Numerous factors have been found to affect the anatase to rutile transition. Reidy and coworkers (Reidy, Holmes et al. 2006) have reported that dopants like Co, Mn and V assist the anatase-to-rutile transition, while dopants like Si, Zr and Al have the opposite effect and help maintain the anatase phase even at elevated temperatures. Similar reductions in the activation energy required for the anatase to rutile transition have been reported for various dopants by Borkar and Dharwadkar (Borkar and Dharwadkar 2004). The anatase to rutile transformation is reported to be enhanced with decrease in pH value (Suresh, Biju et al. 1998), which is believed to be due to the contributions from an intermediate brookite phase (Hu, Tsai et al. 2003-a; Hu, Tsai et al. 2003-b). Surface effects also decide the anatase to rutile critical diameter (Barnard, Saponjic et al. 2005).

Apart from the chemical environment, particle size has been suggested as one of the most significant factors to control the phase stability of TiO_2 nanoparticles. It is believed that the main reason for transformation of anatase particles to rutile upon heating is the increase in particle size during to enhanced sintering at increased temperatures. Recently, Zhang and Banfield (Zhang and Banfield 2000) reported from their experimental analysis that anatase is most thermodynamically stable at size less than 11 nm, brookite is most stable for crystal sizes between 11 and 35 nm, and rutile is most stable at sizes greater than 35 nm. Thus, brookite would directly transform to rutile while anatase may either transform directly to rutile or to brookite and then to rutile. Ranade and coworkers (Ranade, Navrotsky et al. 2002) calculated from their experiments the enthalpy relative to bulk rutile calculated at 298K, for rutile, anatase and brookite with varying surface areas (shown in Figure VI.1 (Ranade, Navrotsky et al. 2002; Navrotsky 2003)). Their results also agree with conclusions drawn by Zhang and Banfield. Similar results are obtained by using molecular dynamics simulations at 300 K in vacuum by Naicker and coworkers (Naicker, Cummings et al. 2005) and are shown in Figure VI.2.

They reported a crossover of phase stability at ~2.5 nm at 300 K in vacuum. Barnard and coworkers (Barnard, Zapol et al. 2005) also provided evidence via their *ab initio* calculations that the crossover diameter is smaller for particles in vacuum than those in water, as shown in Figure VI.3. and the consideration of the appropriate surface passivation of nanocrystal surfaces is necessary to accurately predict the size dependence of the anatase-to-rutile phase transistion

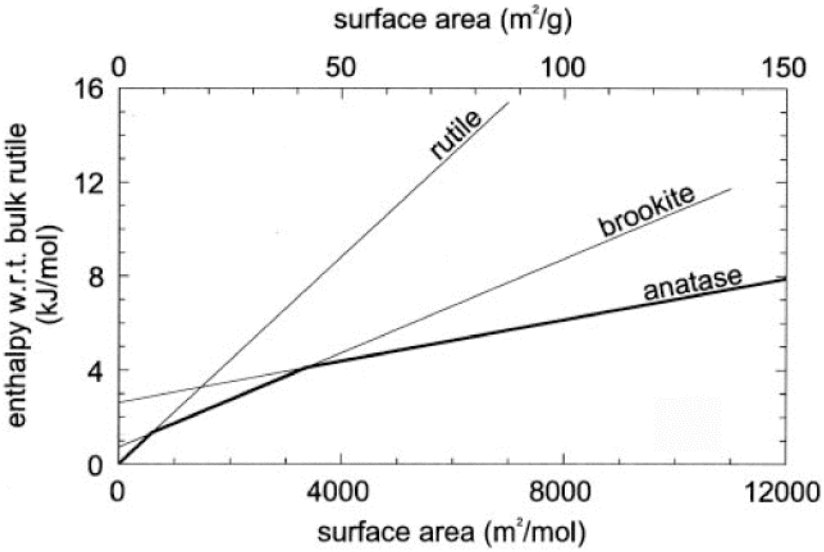

Figure VI.1 Enthapies w.r.t bulk rutile of rutile, anatase and brookite with varying surface area.

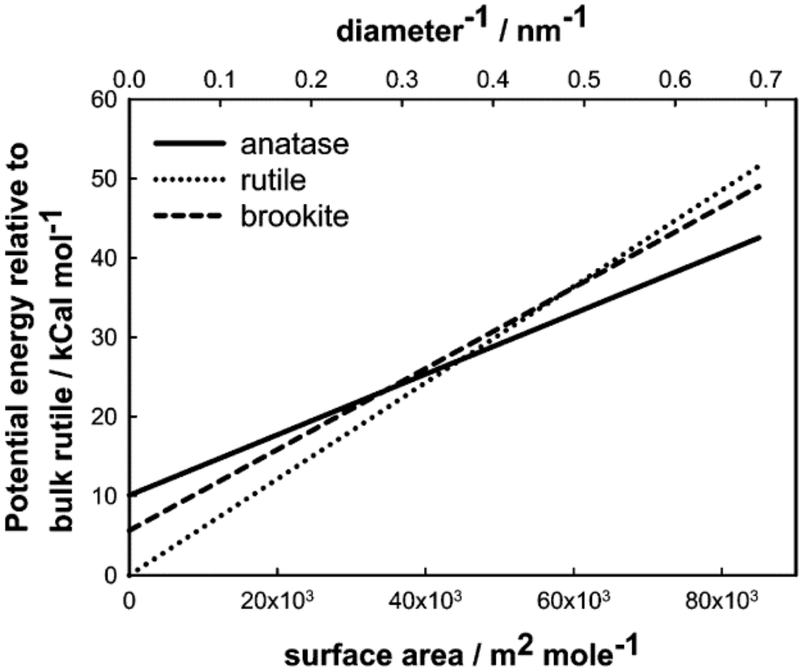

Figure VI.2 Energy of particles relative to bulk rutile as a function of surface area at 300 K from molecular dynamics simulations.

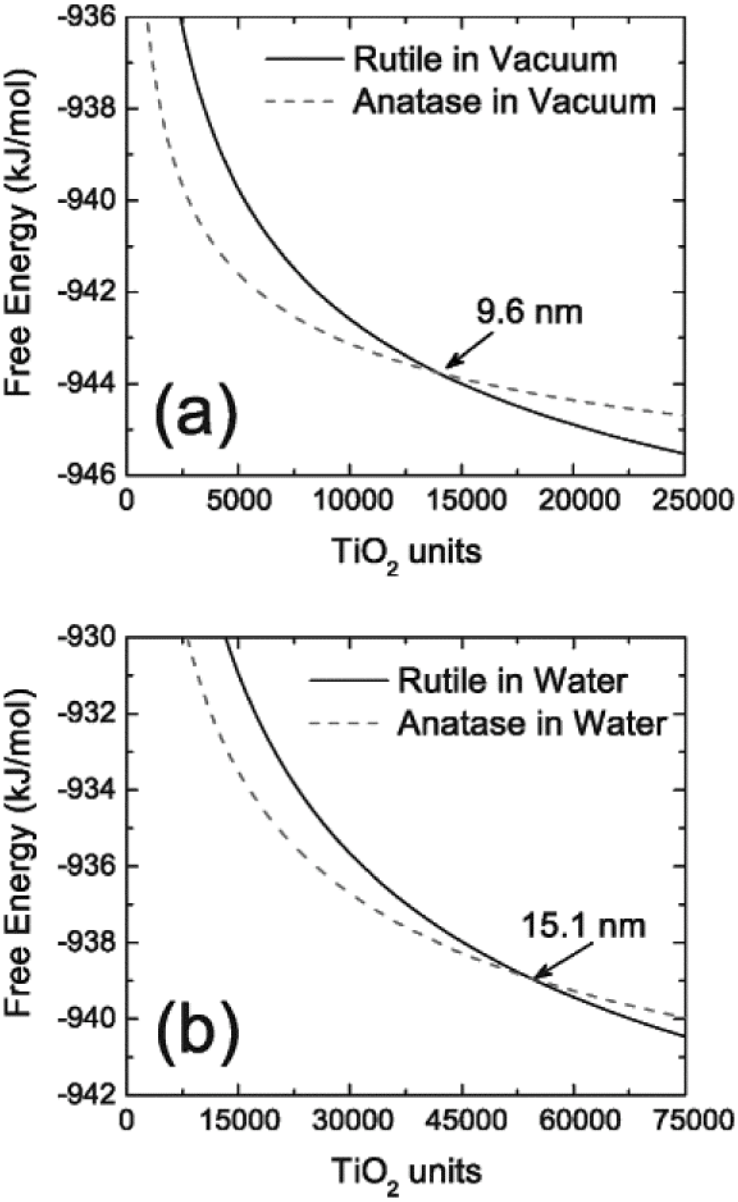

Figure VI.3 Free energy as a function of number of TiO_2 units for anatase and rutile in (a) vacuum and (b) water.

VI.2.1 Insight from Prior Simulations

An analysis of molecular dynamics simulation results, similar to those conducted by Naicker *et. al.* can be performed using the data generated from the simulations discussed in Chapter IV at 573 K. The results obtained are depicted in Figure VI.4. A linear increase in potential energy with increase in surface area (decrease in particle size) is observed. Upon extrapolation, a crossover size of ~1.7 nm can be estimated. In other words, nanoparticles smaller than ~1.7 nm have anatase as their most stable phase at 573 K in vacuum. Comparing these results to those obtained by Naicker *et. al.*, it is evident that as the temperature is increased the crossover diameter for phase stability decreases. Thus, at higher temperatures even smaller particles will be stable as rutile.

Figure VI.5 shows the variation in potential energy of 3 nm nanoparticles as the temperature is increased. The temperatures considered are comparable to the temperatures prevailing in the flame reactor during manufacturing of TiO_2 using the "chloride" process. It is observed that the gap between anatase and rutile increases with temperature thereby increasing the relative stability of rutile.

No phase transformations were observed in the simulations at higher temperatures of single particles as reported in Chapter IV. In Chapter III, sintering between like-phased nanoparticles were considered and no phase transformations were observed over the time scales considered. In this chapter, sintering between 3 nm particles of different phases is considered to examine possibility of phase transformation.

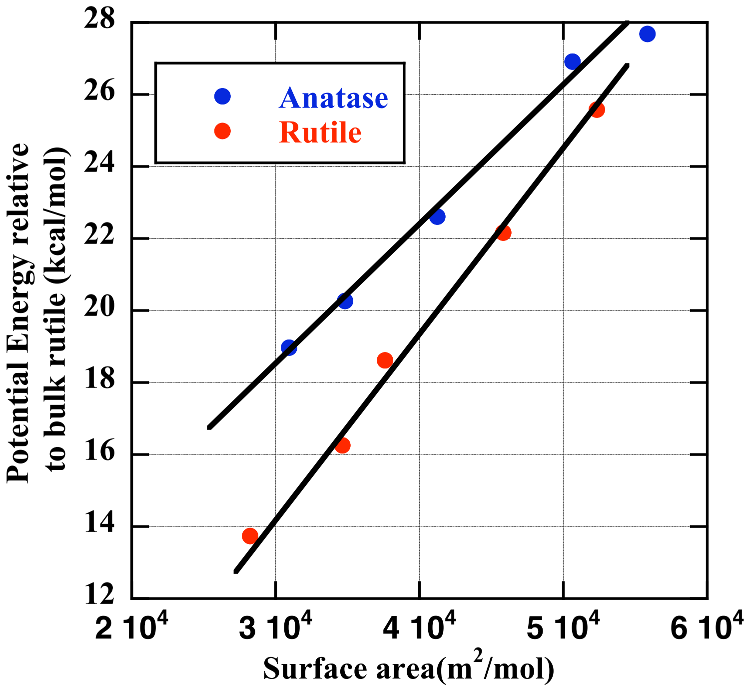

Figure VI.4 Energy of particles relative to bulk rutile as a function of surface area at 1473 K.

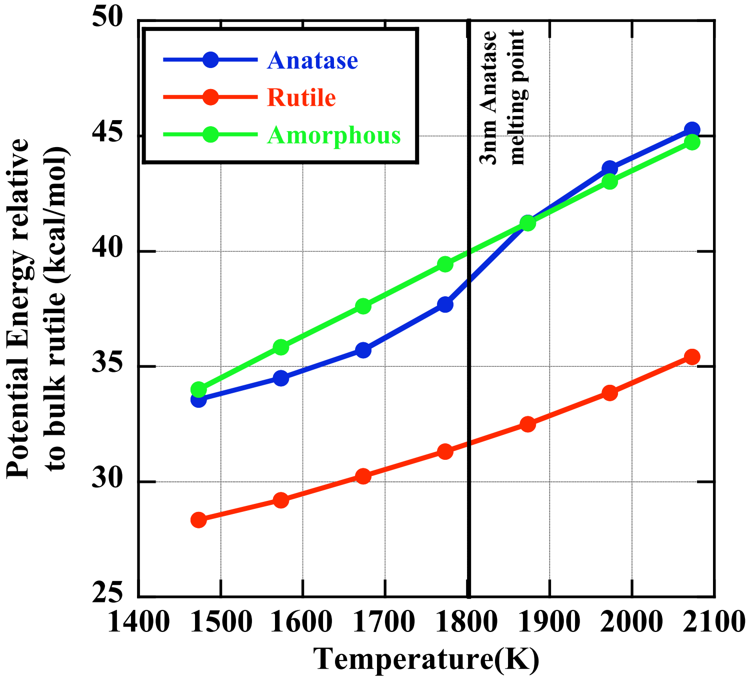

Figure VI.5 Variation of energy w.r.t bulk rutile of 3 nm anatase, rutile and amorphous particles.

VI.2 Simulation Details

VI.2.1 Forcefield Selection

The Matsui-Akaogi forcefield (Matsui and Akaogi 1991) has been selected to describe the interactions between Ti and O ions. The details and advantages of this forcefield over the other reported forcefields for TiO_2 have been listed in Chapter II. The forcefield parameters are listed in Table II.2. The Daresbury laboratory molecular dynamics simulation code, DL_POLY version 2.13 (Smith 1987; Smith and Forester 1996) has been used to perform all the simulations on a parallel architecture.

VI.2.2 Methodology

The simulation method used is exactly similar to that described in chapter III. The only difference is that the particles considered in the simulation are of different phases. The gap between the particles at the beginning of the simulation is 1 nm. All the Ti and O ions are considered for long-range force calculations. No periodic boundary conditions are used. The simulations are performed with constant volume and constant energy. The following combinations are considered:

(a) One 3 nm anatase + one 3 nm rutile starting at 1473 K,
(b) One 3 nm amorphous + one 3 nm rutile starting at 1473 K
(c) One 3 nm anatase + one 3 nm amorphous + one 3 nm rutile starting at 1473 K
(d) One 3 nm anatase + one 3 nm amorphous starting at 1473 K
(e) Various combinations at a lower temperature of 973 K

Simulated X-ray diffraction patterns are used to detect any possible phase transformations occurring during the sintering process. All simulations are conducted for extended times of at least 10ns.

VI.3 Results and Discussion

The temperature and potential energy of the various simulation systems are plotted against time in Figures VI.6 and VI.7, respectively.

VI.3.1 Anatase + Rutile

It is observed that the temperature increases initially to about 1600 K and then after about 4.5ns there is another temperature jump by ~100 K. As the sintering process continues, a rutile front is observed to be moving into the anatase nanoparticle. A gradual anatase to rutile transformation is depicted in the simulation snapshots shown in Figure VI.9. The X-ray diffraction patterns at various time intervals also suggest that the rutile phase is becoming predominant as the sintering progresses. Thus, it is believed that if the simulations are continued for very long periods of time a single rutile particle will be obtained.

VI.3.2 Rutile + Amorphous

The amorphous nanoparticle required for this case is obtained by heating a 3 nm rutile particle to 3000 K and then cooling it back to 1473 K. Upon heating at 3000 K, complete melting occurs and the crystal structure is totally lost. Cooling back to 1473 K, gives an amorphous solid TiO_2 nanoparticle. During the course of the sintering simulation, the temperature gradually rises to 1700 K in about 5ns and then remains constant. A corresponding decrease in potential energy to about -884kcal/mol is observed. The increase in height of the peaks in the X-ray diffraction patterns indicates that the amorphous particle, after necking with the rutile particle, gradually undergoes a slow phase transformation to rutile. Again, the final phase at the end of 10ns is rutile. X-ray diffraction patterns and snapshots can be found in Figure VI.10 and VI.11, respectively.

VI.3.3 Anatase + Amorphous + Rutile

Three 3 nm TiO_2 nanoparticles are placed at the vertices of an equilateral triangle to obtain the initial configuration required for this case. As the simulation proceeds, all particles neck with the other two particles in the system and the thickness of the neck gradually increases. The temperature of the system increases sharply and reaches a value above the melting point of anatase in about 2ns. Both the amorphous and the anatase particles have been found to undergo phase transformation to rutile. The final agglomerate obtained at the end of 10ns is rutile. From the snapshots in Figure VI.13, it can be observed that the final agglomerate contains two unequally sized grains of rutile. The transformation of the amorphous particle to rutile is faster than that of the anatase particle. X-ray diffraction patterns and simulation snapshots are shown in Figure VI.12.

VI.3.4 Anatase + Amorphous

All simulations discussed thus far had a 3 nm rutile particle present in the system, with rutile being the most stable phase at high temperatures, the final agglomerate obtained in all the simulations has been rutile. In this simulation, no rutile phase is present at the system at the beginning. The particles attract each other, form a neck and gradual broadening of the neck occurs. The temperature of the system increases and stays at ~1600 K for about 4ns and then increases again to close to the melting point of anatase. It is found from the simulated X-ray diffraction patterns (see Figure VI.14) that the agglomerate formed at the end of 8ns is crystalline (as seen in snapshots in Figure VI.15) and is neither anatase nor rutile. From the positioning of the X-ray diffraction peaks, the crystal phase is found to be brookite. Also, the temperature of the system does appear to be increasing even after 9ns. Thus, if run for longer periods of time another phase transformation may be observed but it is beyond the scope of the simulations reported here. To our knowledge, this is the first observed phase transformation from anatase to brookite via molecular dynamics simulations.

It should be noted that the O ions are not shown in all the simulation snapshots in Figures VI.9, VI.11, VI.13 and VI.15 for clarity. The rutile nanoparticle is colored orange, anatase is blue and amorphous particle is represented in green.

VI.3.5 Lower Temperature Simulations

All the above-mentioned sets of simulations were repeated at a lower starting temperature of 973 K. In all the lower temperature cases, the particles connected and formed necks. The system temperatures increased to about 1100 K but no phase transformation was observed over the timescales considered. The fact that the maximum system temperature is well below the melting point of 3 nm anatase is responsible for no observable phase transformation in simulations with lower starting temperatures.

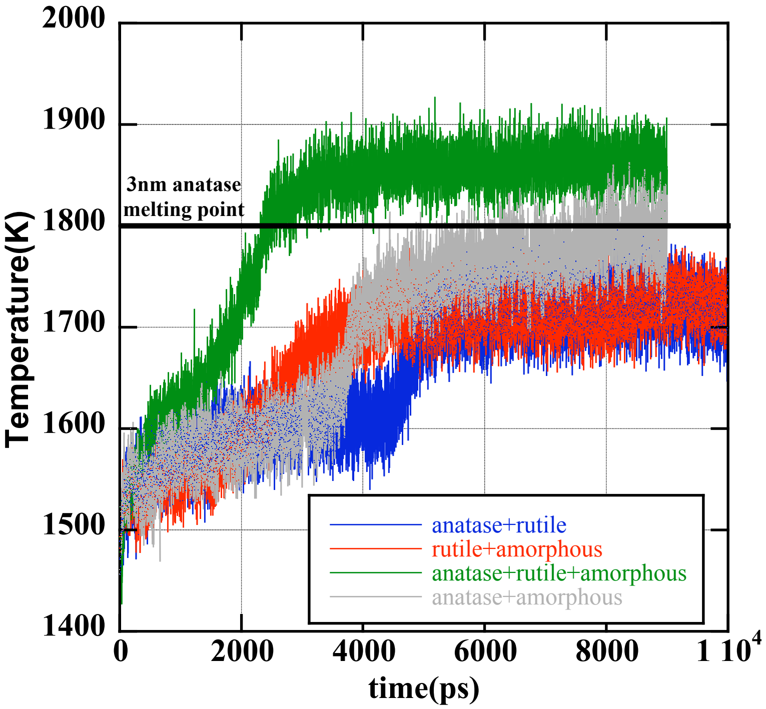

Figure VI.6 Temperature versus time for various sintering simulations.

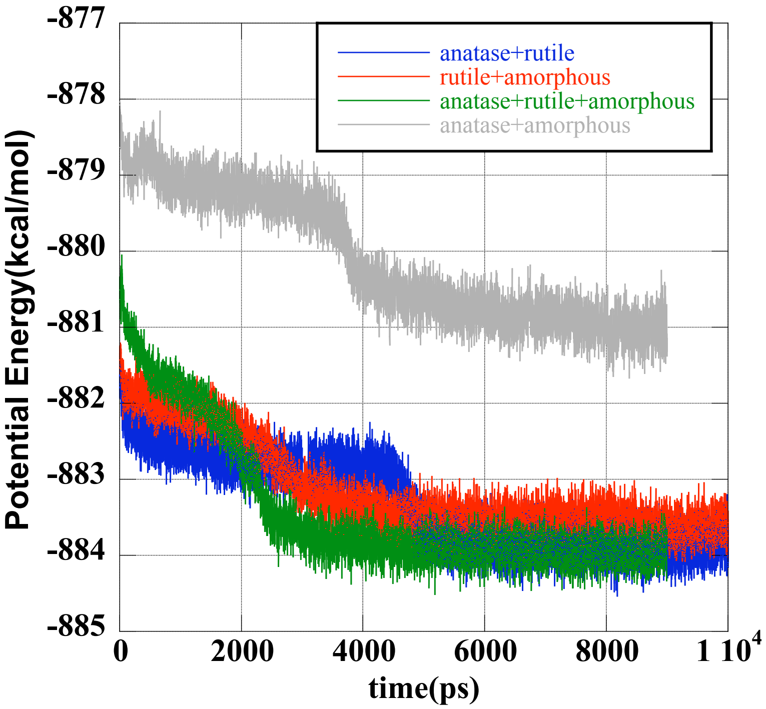

Figure VI.7 Energy profiles of various sintering simulations.

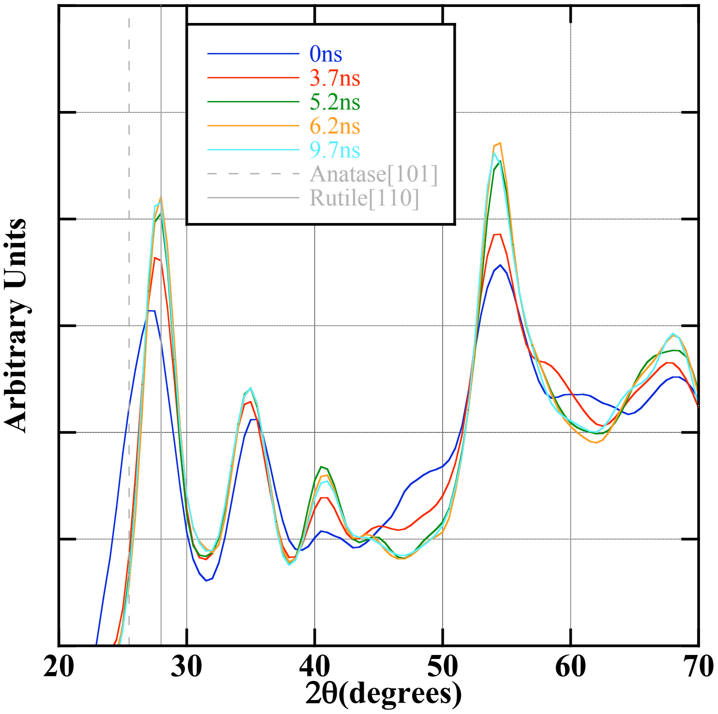

Figure VI.8 Simulated X-ray diffraction patterns of anatase + rutile nanoparticle sintering with starting temperature 1473 K.

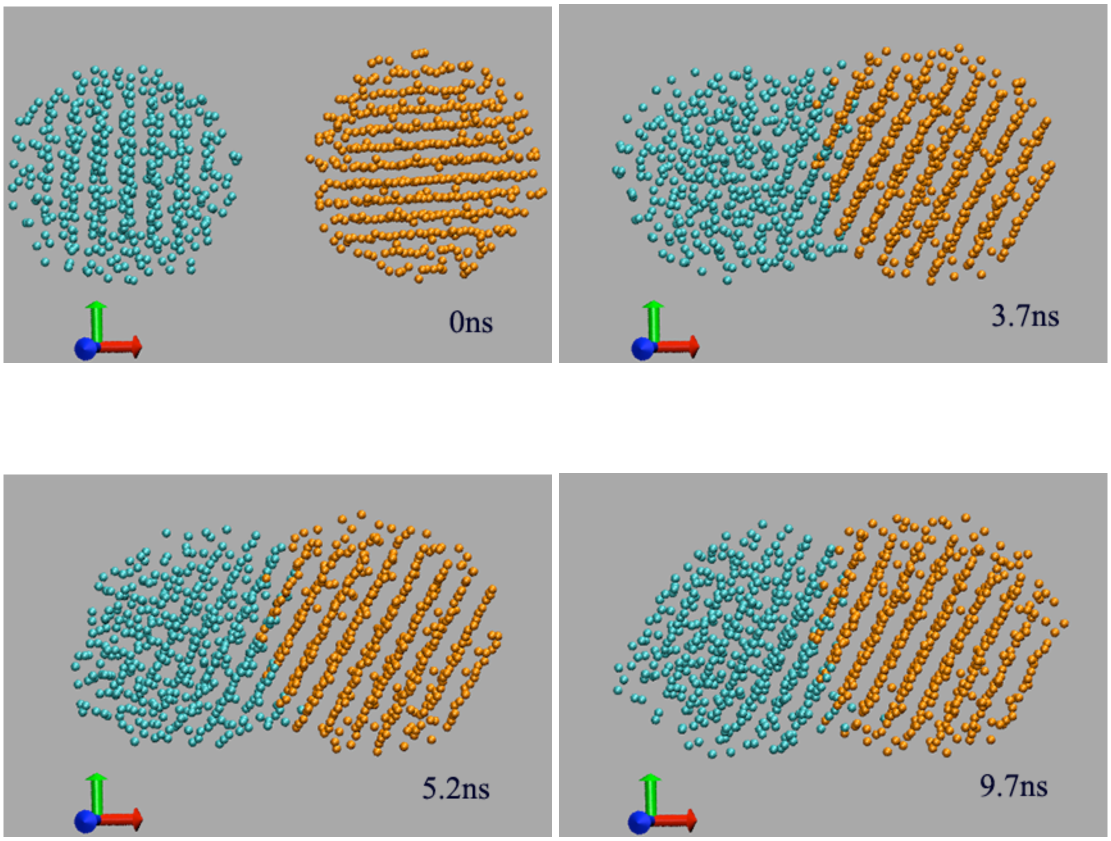

Figure VI.9 Snapshots of 3 nm anatase + 3 nm rutile sintering simulation.

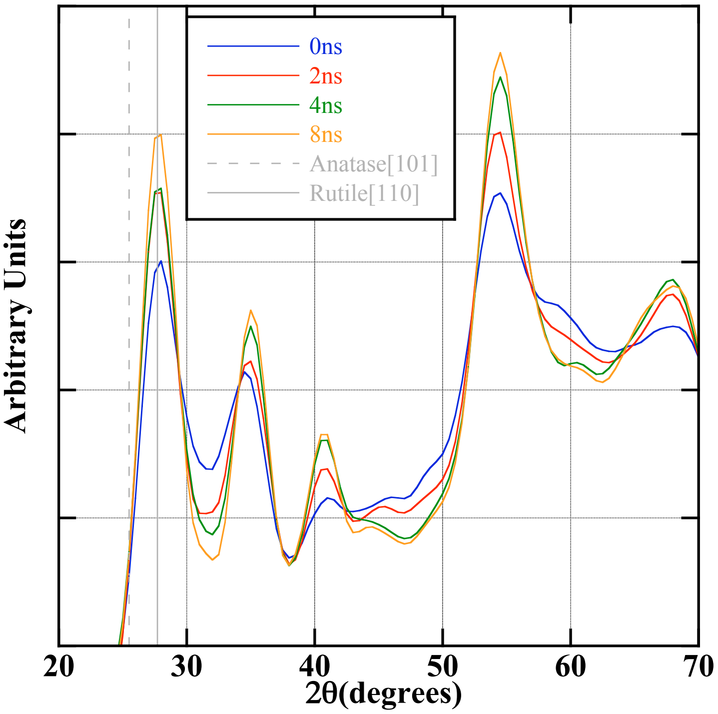

Figure VI.10 Simulated X-ray diffraction patterns of rutile + amorphous nanoparticle sintering with starting temperature 1473 K.

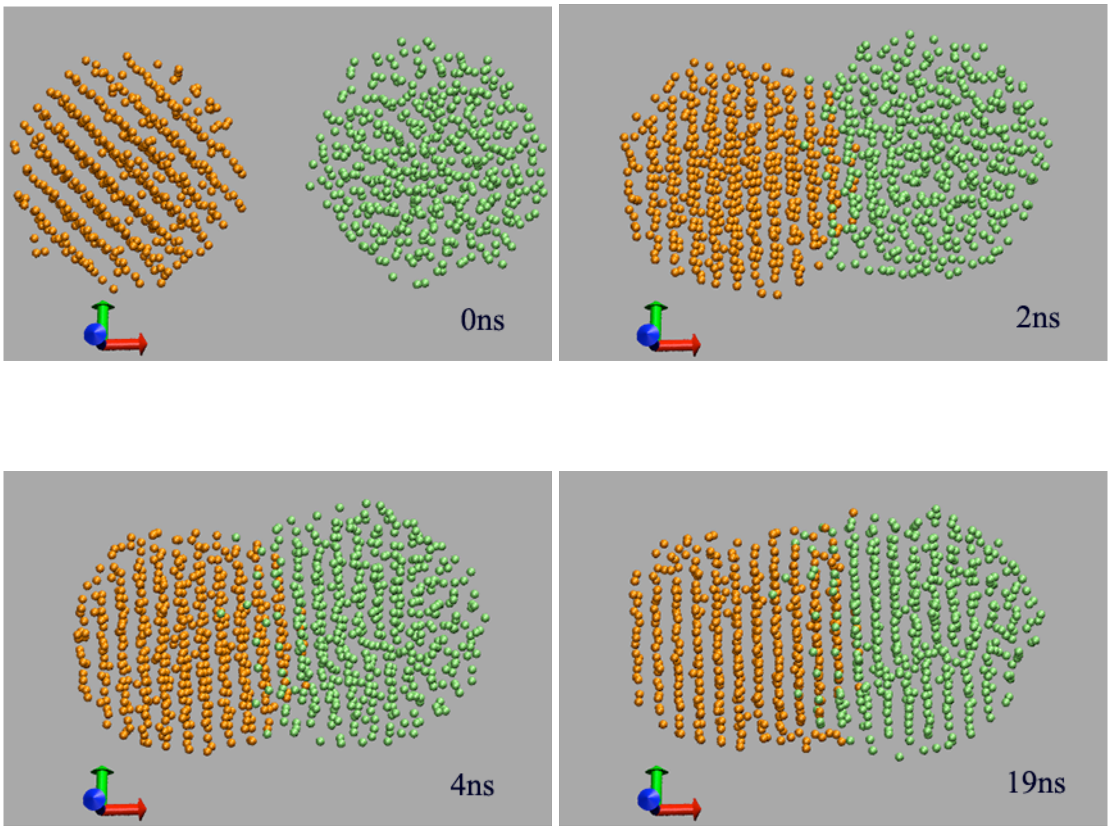

Figure VI.11 Snapshots of 3 nm rutile + 3 nm amorphous sintering simulation.

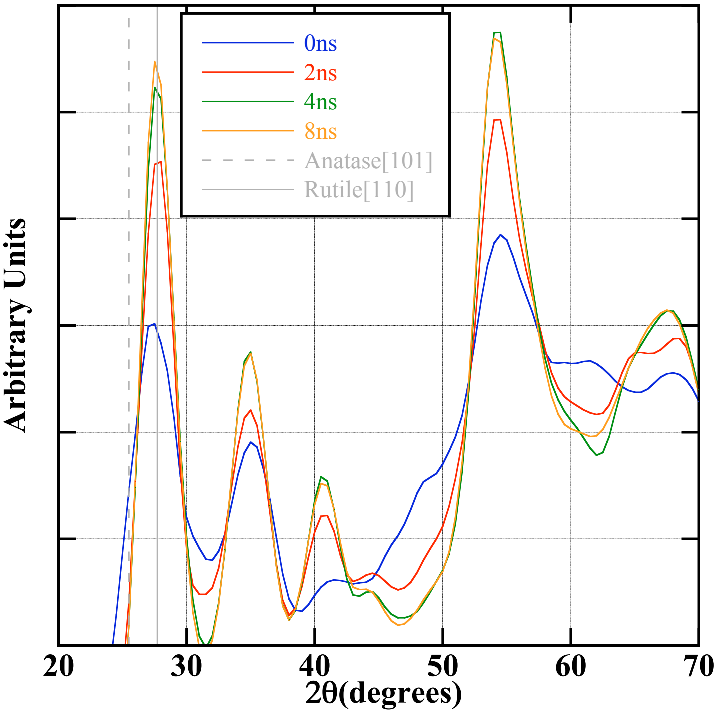

Figure VI.12 Simulated X-ray diffraction patterns of anatase + amorphous + rutile nanoparticle sintering with starting temperature 1473 K.

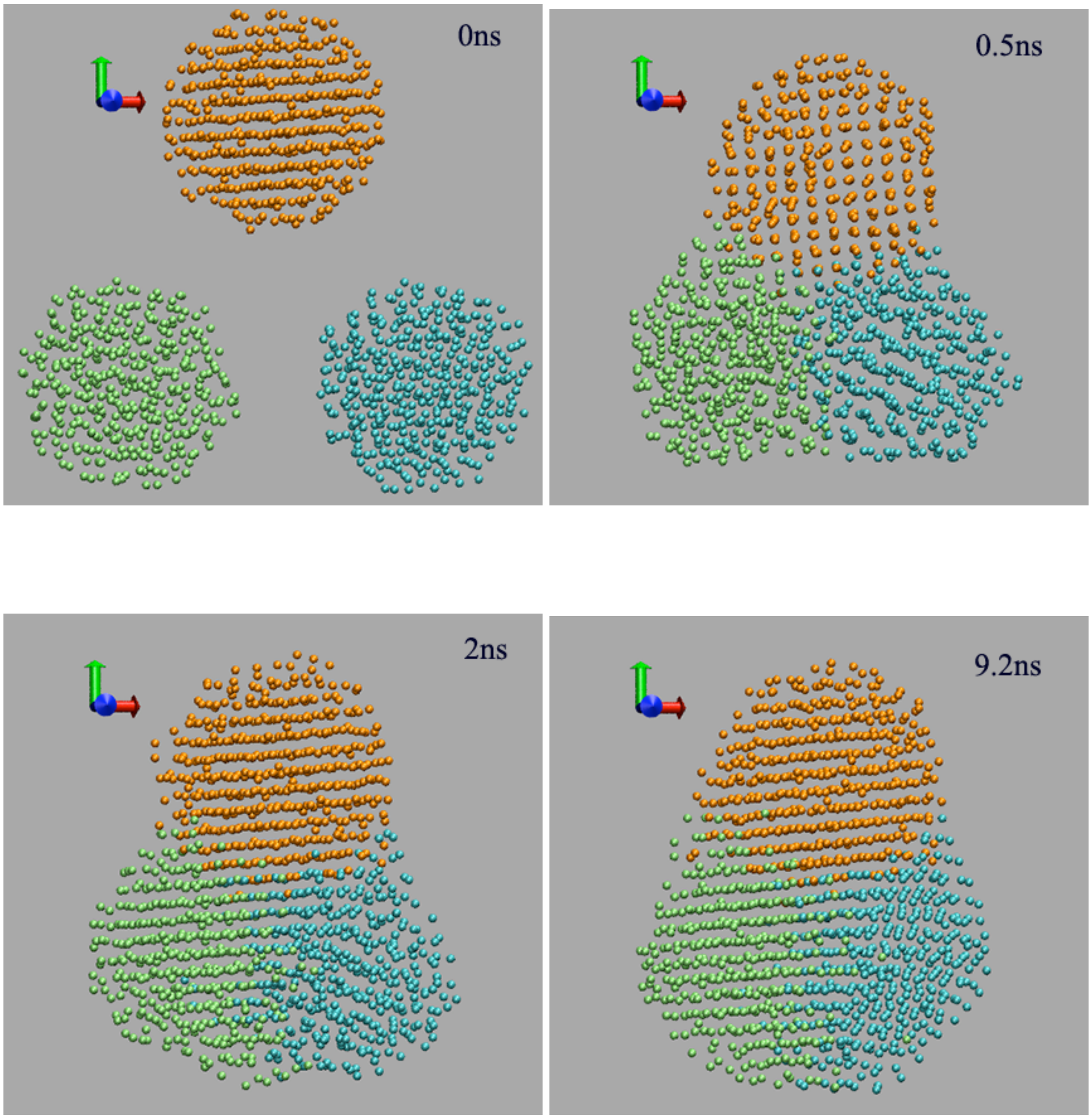

Figure VI.13 Snapshots of 3 nm anatase + 3 nm amorphous + 3 nm rutile sintering simulation.

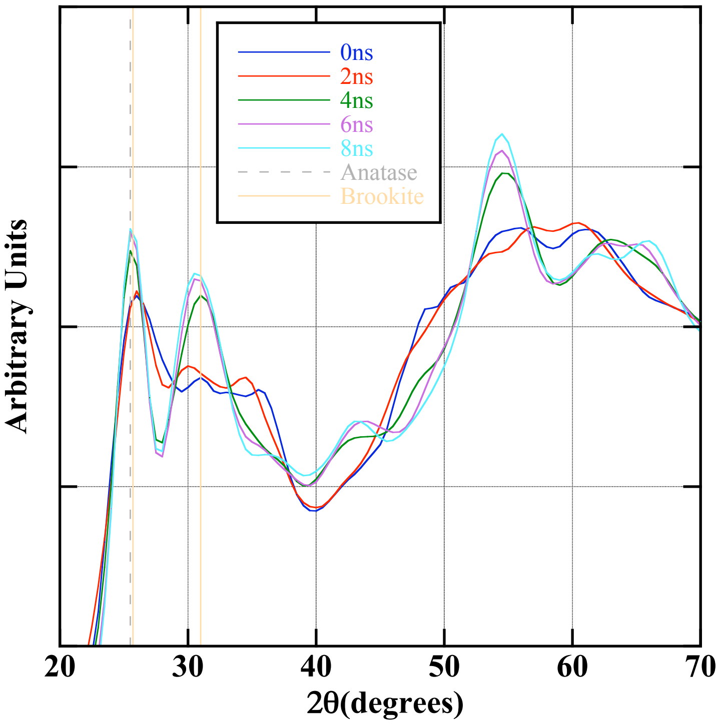

Figure VI.14 Simulated X-ray diffraction patterns of anatase + amorphous nanoparticle sintering with starting temperature 1473 K.

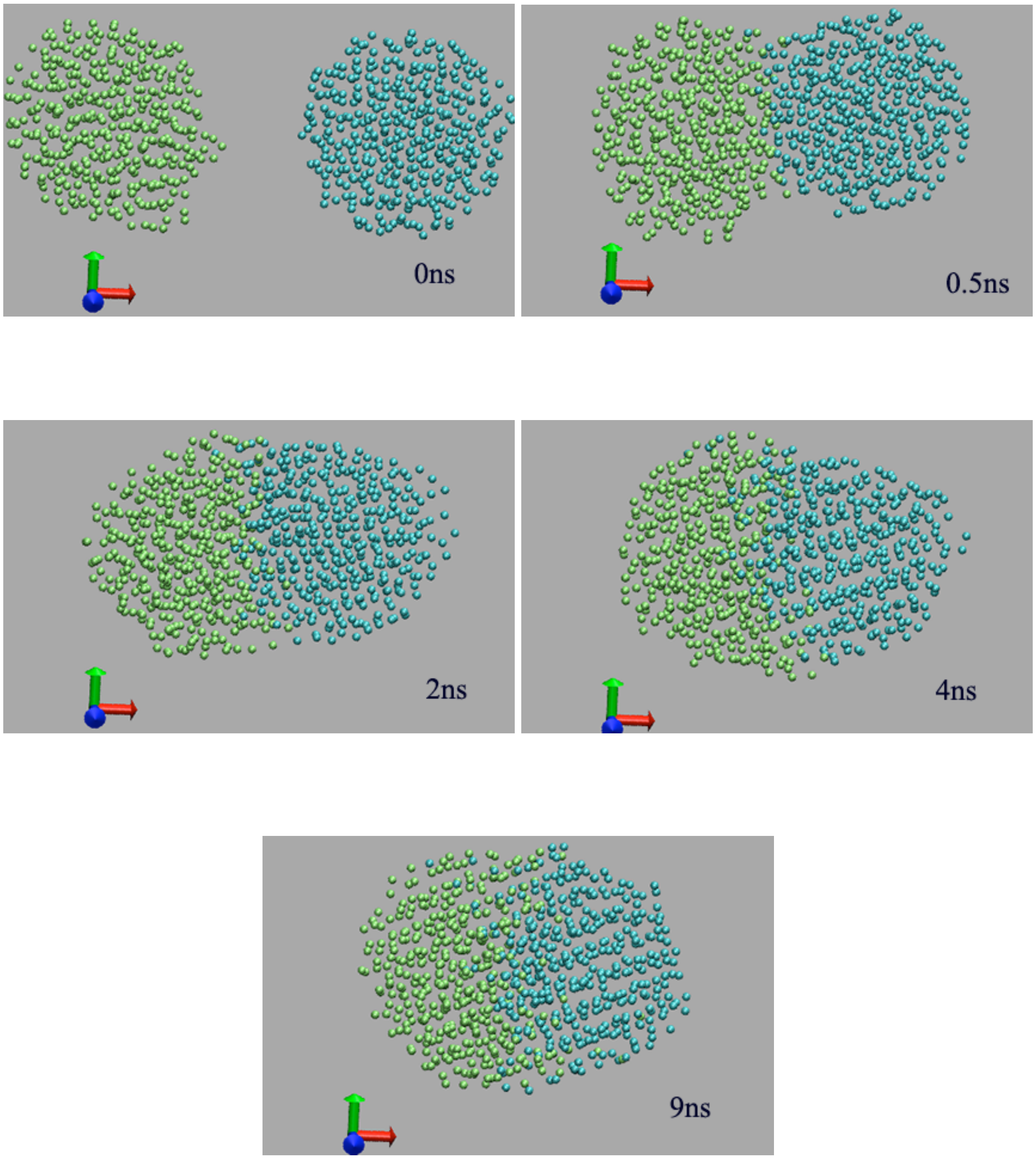

Figure VI.15 Snapshots of 3 nm anatase + 3 nm amorphous sintering simulation with a starting temperature of 1473 K.

VI.4 Conclusions

Phase stability of TiO_2 nanoparticles is different from bulk TiO_2. Anatase is the most stable form in the nanoform, while rutile is the most stable in the bulk. Factors like the chemical environment and the particle size have a huge influence on the phase stability criterion. Zhang and Banfield (Zhang and Banfield 1998) showed that particles smaller than 11 nm were stable as anatase. But it is found that this critical diameter is smaller in vacuum and becomes smaller with increase in temperature. In other words, rutile is the most stable phase in vacuum at higher temperatures.

Various sintering simulations with different phases were carried out with a starting temperature of 1473 K. All simulations showed a drop in potential energy and increase in system temperature. If one of the sintering particles is rutile, the final phase of the agglomerate formed is found to be rutile. For the anatase + amorphous simulation, the final phase at the end of 10ns was found to be brookite. It is believed that if this simulation is run for very long time periods, a brookite-to-rutile phase transformation may be observed. These appear to be the first observed phase transformations during nanoparticle sintering reported in the literature using molecular dynamics simulations. Although incomplete anatase to rutile transformations during fast sintering of 100nm particles have been experimentally observed (Bykov, Gusev et al. 1995). As reported by Rhee and coworkers in the case of Si_3N_4 particles (Rhee, Lee et al. 2000), the enhanced ionic mobility during sintering of nanoparticles plays an important role in the phase transitions.

No such phase transformations were observed in the simulations carried out with a lower starting temperature over the timescales considered (10ns). The system temperatures are remote from the melting point of 3 nm anatase unlike the simulations carried out with the starting temperatures of 1473 K. In fact, this proximity to melting point is believed to enhance the phase transformations.

CHAPTER VII

SUMMARY AND FUTURE WORK

VII.1 Summary

In the research work reported here, various aspects of TiO_2 nanoparticles, especially anatase and rutile nanoparticles, have been studied using molecular dynamics simulations. In Chapter III, the phenomenon of sintering of anatase and rutile nanoparticles is examined from atomic point of view. It is found that the initial stages of the sintering phenomena are very rapid and highly dependent on particle orientation. This research has been published in the Journal of Physical Chemistry B (Koparde and Cummings 2005). In Chapter IV, the applicability of phenomenological models developed in the past for micron-sized particle sintering to TiO_2 nanoparticle sintering has been examined. The fact that about 35-45% of the total ions of the nanoparticles reside in the surface layer is found to be very vital and hence, a linear rate law cannot successfully model area reduction during nanoparticle sintering. The phenomenon of "melting point depression" is examined for TiO_2 nanoparticles using molecular dynamics simulations to corroborate the argument that the ionic diffusion occurring during sintering is solid-state diffusion. The results shown in Chapter IV have been submitted to the Journal of Material Chemistry for publication.

In Chapter V, the orientational preference of water molecules on the surface of TiO_2 nanoparticles was determined. The water molecules in the first hydration layer are found to have two preferred orientations. The probabilistic analysis of the water orientations and their variations with particle size and phase has been compiled into a manuscript, which is being submitted to the Journal of Physical Chemistry B. In Chapter VI, the phase transformations occurring during the sintering of nanoparticles of different phases were studied using simulated X-ray diffraction patterns (see Appendix A). These are probably the first phase transformations at nanoscale, observed using molecular dynamics simulations. A manuscript with the results reported in Chapter VI is currently being prepared for Nanoletters.

VII.2 Possible Directions for Future Work

The results from Chapter III suggest that the stages before the advent of nanoparticle sintering can be modeled as a macroscopic phenomenon using spheres with fluctuating dipole moments as nanoparticles. More research can be focused in the future to examine this possibility. It has been shown in Chapter IV, that a considerable percentage of ions of the nanoparticles are on the surface. Hence, it may be a good idea to model the surface ions differently than those in the nanoparticle core. *Ab initio* methods could be combined with classical molecular dynamics methods to improve the quality of the interaction potentials. The Matsui-Akaogi forcefield (Matsui and Akaogi 1991) used in this research under-predicts the anatase-to-rutile critical diameter by a factor of ~4. The fact that the surface ions of the nanoparticle have the same charge as the ions in the core of the nanoparticle may be affecting the phase stability. Hence, a possible solution could be to direct more effects to develop an *ab initio*-derived variable-charge potential, which can be applied to the nanoparticles. As phase transformations have been observed in vacuum simulations of nano-TiO_2, it may be possible to examine for such phase transformations in aqueous environment in the future. As water is the medium for most photocatalytic applications of nano-TiO_2 and photoactivity is extremely phase-dependent, these studies will prove to be of great importance.

Upon development of applicable forcefields, similar attempts of modeling nanoparticles in vacuum and aqueous environments; and studies of phase transformations at the nanoscale can be performed for other environmentally abundant metal-oxide nanoparticles such as manganese oxides, tin oxides and zirconium oxides.

APPENDIX A

DETERMINATION OF SIMULATED X-RAY DIFFRACTION DATA

X-ray diffraction is a technique used for determination of crystal structure. X-rays are generated by bombarding a metal target (generally copper) with high-energy electrons in vacuum. The bombardment excites the electrons in copper, which upon relaxation release photons forming the X-rays. These X-rays can then be directed on to the sample whose crystal structure is to be determined. Most of the X-rays pass through the sample, but some of them are diffracted either constructively or destructively resulting in a pattern, which can be used to calculate the lattice parameters of the crystal. The fact that the wavelength of X-rays is comparable to inter-atomic distances in a variety of crystals is the main reason for the success of this technique.

As the number of electrons and the size of the atomic orbitals vary from atom to atom, different atoms have different scattering efficiencies, which are quantified using the scattering factor, *f*, as follows (McQuarrie and Simon 1998),

$$f = 4\pi \int_0^\infty \rho(r) \frac{\sin kr}{kr} r^2 dr \tag{A.1}$$

where r is the distance from the center of the atom to the volume element, $\rho(r)$ is the spherically symmetric electron number density, $k = (4\pi/\lambda)\sin\theta$, where θ is the scattering angle and λ is the wavelength of X-ray radiation. Cromer and Mann (Cromer and Mann 1968) computed from numerical *ab initio* data the scattering factors for various neutral atoms and ions, and fitted it to the analytical form,

$$f\left(\frac{\sin\theta}{\lambda}\right) = \sum_{i=1}^{4} a_i \exp\left[-b_i\left(\frac{\sin\theta}{\lambda}\right)^2\right] + c \qquad \text{(A.2)}$$

In molecular dynamics simulations, the positions of every atom can be determined at every timestep. These can be reported to a file after a certain user-defined time interval. Using these atomic coordinates, the X-ray diffraction pattern can be determined by utilizing the Debye function (Debye 1915) for total scattering intensity as described by Gnutzmann and Vogel (Gnutzmann and Vogel 1990),

$$I_N(b) = \sum_{n=1}^{N} \sum_{m=1(m\neq n)}^{N} f_n(b) f_m(b) \frac{\sin(2\pi b r_{nm})}{2\pi b r_{nm}} \qquad \text{(A.3)}$$

where $f_n(b)$ and $f_m(b)$ are the atomic scattering factors of atoms *n* and *m*, respectively. They are calculated using the data generated by Cromer and Mann. r_{nm} is the distance between the atoms *n* and *m*; $b = 2\sin\theta/\lambda$ is the length vector in the reciprocal space; λ is the wavelength and θ is the Bragg angle. In the simulated X-ray diffraction patterns reported in this work, the value of λ is taken as that of CuKα radiation (1.5418 Å). The absolute value of *I* is not important but its relative variation with the scattering angle gives as the cumulative X-ray diffraction pattern of the *N* atoms.

BIBLIOGRAPHY

Abrahams, S. C. and J. L. Bernstein (1971). "Rutile: Normal probability plot analysis and accurate measurement of crystal structure." Journal of Chemical Physics **55** (7): 3206-3211.

Ahn, J. P., J. K. Park, et al. (1998). "Effect of compact density on phase transition kinetics from anatase phase to rutile phase during sintering of ultrafine titania powder compacts." Nanostructured Materials **10** (6): 1087-1096.

Akhtar, M. K., X. O. Yun, et al. (1991). "Vapor synthesis of titania powder by titanium tetrachloride oxidation." AIChE Journal **37** (10): 1561-1570.

Alavi, S. and D. L. Thompson (2006). "Molecular dynamics simulations of the melting of aluminum nanoparticles." Journal of Physical Chemistry A **110** (4): 1518-1523.

Allen, M. P. and D. J. Tildesley (1997). Computer Simulation of Liquids, New York, Oxford University Press, Inc.

Augugliaro, V., V. Loddo, et al. (1995). "Performance of heterogeneous photocatalytic systems: Influence of operational variables on photoactivity of aqueous suspension of TiO_2." Journal of Catalysis **153** (1): 32-40.

Bakardjieva, S., V. Stengl, et al. (2006). "Transformation of brookite-type TiO_2 nanocrystals to rutile: Correlation between microstructure and photoactivity." Journal of Materials Chemistry **16** (18): 1709-1716.

Bandura, A. V. and J. D. Kubicki (2003). "Derivation of force field parameters for TiO_2-H_2O systems from ab initio calculations." Journal of Physical Chemistry B **107** (40): 11072-11081.

Banfield, J. F. and D. R. Veblen (1992). "Conversion of perovskite to anatase and TiO_2 (B) - a TEM study and the use of fundamental building-blocks for understanding relationships among the TiO_2 minerals." American Mineralogist **77** (5-6): 545-557.

Banfield, J. F., D. R. Veblen, et al. (1991). "The identification of naturally-occurring TiO_2 (B) by structure determination using high-resolution electron-microscopy, image simulation, and distance-least-squares refinement." American Mineralogist **76** (3-4): 343-353.

Barnard, A., Z. Saponjic, et al. (2005). "Multi-scale modeling of titanium dioxide: Controlling shape with surface chemistry." Reviews on Advanced Materials Science **10** (1): 21-27.

Barnard, A. S., P. Zapol, et al. (2005). "Modeling the morphology and phase stability of TiO_2 nanocrystals in water." Journal of Chemical Theory and Computation **1** (1): 107-116.

Berendsen, H. J. C., J. R. Grigera, et al. (1987). "The missing term in effective pair potentials." Journal of Physical Chemistry **91** (24): 6269-6271.

Bird, R. B., W. E. Stewart, et al. (2002). Transport Phenomena, New York, John Wiley & Sons, Inc.

Bokhimi, X., A. Morales, et al. (2001). "Local order in titania polymorphs." International Journal of Hydrogen Energy **26** (12): 1279-1287.

Bondi, A. (1964). "van der Waals volumes and radii." Journal of Physical Chemistry **68** (3): 441-451.

Borkar, S. A. and S. R. Dharwadkar (2004). "Temperatures and kinetics of anatase to rutile transformation in doped TiO_2 heated in microwave field." Journal of Thermal Analysis and Calorimetry **78** (3): 761-767.

Boskovic, S., D. Kosanovic, et al. (2001). "Densification and phase transformation of Si_3N_4 in the presence of mechanically activated $BaCO_3$-Al_2O_3-SiO_2 mixture." Powder Technology **120** (3): 194-198.

Buffat, P. and J.-P. Borel (1976). "Size effect on the melting temperature of gold particles." Physical Review A **13** (6): 2287-2298.

Bykov, Y., S. Gusev, et al. (1995). "Sintering of nanophase oxide ceramics by using millimeter-wave radiation." Nanostructured Materials **6** (5-8): 855-858.

Catlow, C. R. A., C. M. Freeman, et al. (1985). "Recent studies using static simulation techniques." Physica B & C **131** (1-3): 1-12.

Catlow, C. R. A. and R. James (1982). "Disorder in TiO_{2-X}." Proceedings of the Royal Society of London Series A-Mathematical Physical and Engineering Sciences **384** (1786): 157-173.

Cerrato, G., L. Marchese, et al. (1993). "Structural and morphological modifications of sintering microcrystalline TiO_2 - an XRD, HRTEM and FTIR study." Applied Surface Science **70-71** (1): 200-205.

Cheng, H., J. Ma, et al. (1995). "Hydrothermal preparation of uniform nanosize rutile and anatase particles." Chemistry of Materials **7** (4): 663-671.

Coblenz, W. S., J. M. Dynys, et al. (1980). "Initial stage solid state sintering models: A critical analysis and assessment." Materials Science Research **13**: 141-157.

Collins, D. R., D. J. Smith, et al. (1997). "Molecular dynamics study of the high temperature fusion of TiO_2 nanoclusters." Journal of Materials Chemistry **7** (12): 2543-2546.

Collins, D. R. and W. Smith (1996-b). "Technical report DL-TR-96-001: Evaluation of TiO_2 force fields." Council for the Central Laboratory of Research Councils, Daresbury **Research Report DL-TR-96-001**.

Collins, D. R., W. Smith, et al. (1996-a). "Molecular dynamics study of TiO_2 microclusters." Journal of Materials Chemistry **6** (8): 1385-1390.

Cromer, D. T. and J. B. Mann (1968). "X-ray scattering factors computed from numerical Hartree-Fock wave functions." Acta Crystallographica A-Crystal Physics Diffraction Theoretical and General Crystallography **24**: 321-324.

Cummings, P. T., M. Predota, et al. (2002). "Molecular-based study of the electric double layer in hydrothermal systems." Geochimica Et Cosmochimica Acta **66** (15A): A160-A160.

Debye, P. (1915). "Zerstreuung von rontgenstahlen (Scattering of X-Rays)." Annalen der Physik **46**: 809-823.

Dewdney, A. K. (1988). "Nanotechnology - Wherein molecular computers control tiny circulatory submarines." Scientific American **258** (1): 100.

Ding, X. Z. and X. H. Liu (1997). "Grain growth enhanced by anatase-to-rutile transformation in gel-derived nanocrystalline titania powders." Journal of Alloys and Compounds **248** (1-2): 143-145.

Dingwell, D. B. (1991). "The density Of titanium (IV) oxide liquid." Journal of the American Ceramic Society **74** (10): 2718-2719.

Dutt, D., J. S. Upadhyaya, et al. (2002). "Studies on cost reduction of ivory base paper without affecting quality." Journal of Scientific & Industrial Research **61** (4): 294-301.

Egorov, A. V., E. N. Brodskaya, et al. (2002). "Solid-liquid phase transition in small water clusters: A molecular dynamics simulation study." Molecular Physics **100** (7): 941-951.

Egorov, A. V., E. N. Brodskaya, et al. (2003). "The effect of ions on solid-liquid phase transition in small water clusters: A molecular dynamics simulation study." Journal of Chemical Physics **118** (14): 6380-6386.

Egorov, A. V., E. N. Brodskaya, et al. (2006). "Molecular dynamics simulations of solid-liquid phase transition in small water aggregates." Computational Materials Science **36** (1-2): 166-170.

Ehrman, S. H., S. K. Friedlander, et al. (1998). "Characteristics of SiO_2/TiO_2 nanocomposite particles formed in a premixed flat flame." Journal of Aerosol Science **29**: 687-706.

Evans, R. D. (1966). An Introduction to Crystal Chemistry, Cambridge, Cambridge University Press.

Fox, M. A. and M. T. Dulay (1993). "Heterogeneous photocatalysis." Chemical Reviews **93** (1): 341-57.

Franks, A. (1987). "Nanotechnology." Journal of Physics E-Scientific Instruments **20** (12): 1442-1451.

Frenkel, D. and B. Smit (2002). Understanding Molecular Simulation: From Algorithms to Applications, San Diego, Academic Press.

Friedlander, S. K. and M. K. Wu (1994). "Linear rate law for the decay of the excess surface-area of a coalescing solid particle." Physical Review B **49** (5): 3622-3624.

Fujihira, M., Y. Satoh, et al. (1981). "Heterogeneous photocatalytic oxidation of aromatic-compounds on TiO_2." Nature **293** (5829): 206-208.

Gavezzotti, A. (1985). "Molecular free-surface - A novel method of calculation and its uses In conformational studies and in organic-crystal chemistry." Journal of American Chemical Society **107** (4): 962-967.

Gay, J. G. and B. J. Berne (1986). "Energy accommodation in collisions of small particles." Journal of Colloid and Interface Science **109** (1): 90-100.

German, R. M. (1996). Sintering Theory and Practice, New York, Wiley-Interscience.

Gnutzmann, V. and W. Vogel (1990). "Structural sensitivity of the standard Pt/SiO_2 catalyst EuroPt-1 to H_2 and O_2 exposure by in situ X-ray diffraction." Journal of Physical Chemistry **94**: 4991-4997.

Gooding, J. J. (2005). "Nanostructuring electrodes with carbon nanotubes: A review on electrochemistry and applications for sensing." Electrochimica Acta **50** (15): 3049-3060.

Gouma, P. I. and M. J. Mills (2001). "Anatase-to-rutile transformation in titania powders." Journal of the American Ceramic Society **84** (3): 619-622.

Gribb, A. A. and J. F. Banfield (1997). "Particle size effects on transformation kinetics and phase stability in nanocrystalline TiO_2." American Mineralogist **82** (7-8): 717-728.

Gruy, F. and M. Pijolat (1992). "Kinetics of anatase TiO_2 surface-area reduction in a mixture of HCl, H_2O, and O_2 .1. Experimental-study." Journal of the American Ceramic Society **75** (3): 657-662.

Heinisch, L. (1996). Synthesis and Processing of Nanocrystalline Powder, TMS Press.

Hotsenpiller, P. A. M., J. D. Bolt, et al. (1998). "Orientation dependence of photochemical reactions on TiO_2 surfaces." Journal of Physical Chemistry B **102** (17): 3216-3226.

Hu, Y., H. L. Tsai, et al. (2003-a). "Effect of brookite phase on the anatase-rutile transition in titania nanoparticles." Journal of the European Ceramic Society **23** (5): 691-696.

Hu, Y., H. L. Tsai, et al. (2003-b). "Phase transformations of precipitated TiO_2 nanoparticles." Materials Science & Engineering A-Structural Materials Properties Microstructure and Processing **344**: 209-214.

Ikemiya, N., J. Umemoto, et al. (1993). "Surface tensions and densities of molten Al_2O_3, Ti_2O_3, V_2O_5 and Nb_2O_5." ISIJ International **33** (1): 156-165.

Impey, R. W., P. A. Madden, et al. (1983). "Hydration and mobility of ions in solution." Journal of Physical Chemistry **87** (25): 5071-5083.

Jackson, J. D. (1975). Classical Electrodynamics, New York, John Wiley & Sons Inc.

Jang, H. D. (1997). "Effects of H_2O on the particle size in the vapor-phase synthesis of TiO_2." AIChE Journal **43** (11): 2704-2709.

Jang, H. D. and J. Jeong (1995). "The effects of temperature on particle-size in the gas-phase production of TiO_2." Aerosol Science and Technology **23** (4): 553-560.

Jedlovszky, P., A. Vincze, et al. (2002). "New insight into the orientational order of water molecules at the water/1,2-dichloroethane interface: A Monte Carlo simulation study." Journal of Chemical Physics **117** (5): 2271-2280.

Ju, S. P. (2005). "A molecular dynamics simulation of the adsorption of water molecules surrounding an Au nanoparticle." Journal of Chemical Physics **122** (9): art. no. 094718.

Kerisit, S., D. J. Cooke, et al. (2005). "Molecular dynamics simulations of the interactions between water and inorganic solids." Journal of Materials Chemistry **15** (14): 1454-1462.

Kim, D. W., N. Enomoto, et al. (1996). "Molecular dynamic simulation in titanium dioxide polymorphs: Rutile, brookite, and anatase." Journal of the American Ceramic Society **79** (4): 1095-1099.

Kim, J. Y., D. W. Kim, et al. (2005). "Influence of anatase-rutile phase transformation on dielectric properties of sol-gel derived TiO_2 thin films." Japanese Journal of Applied Physics Part 1-Regular Papers Brief Communications & Review Papers **44** (8): 6148-6151.

Kobata, A., K. Kusakabe, et al. (1991). "Growth and transformation of TiO_2 crystallites in aerosol reactor." AIChE Journal **37** (3): 347-359.

Koch, W. and S. K. Friedlander (1990). "The effect of particle coalescence on the surface-area of coagulating aerosol." Journal of Colloid and Interface Science **140** (2): 419-427.

Koparde, V. N. and P. T. Cummings (2005). "Molecular dynamics simulation of titanium dioxide nanoparticle sintering." Journal of Physical Chemistry B **109** (51): 24280-24287.

Kraft, T. and H. Riedel (2004). "Numerical simulation of solid state sintering: Model and application." Journal of the European Ceramic Society **24** (2): 345-361.

Kruis, F. E., K. A. Kusters, et al. (1993). "A simple-model for the evolution of the characteristics of aggregate particles undergoing coagulation and sintering." Aerosol Science and Technology **19** (4): 514-526.

Kumar, K. N. P. (1995). "Growth of rutile crystallites during the initial-stage of anatase-to-rutile transformation in pure titania and in titania-alumina nanocomposites." Scripta Metallurgica Et Materialia **32** (6): 873-877.

Kumar, K. N. P., K. Keizer, et al. (1992). "Densification of nanostructured titania assisted by a phase-transformation." Nature **358** (6381): 48-51.

Laurvick, C. A. and B. Singaraju (2003). "Nanotechnology in aerospace systems." IEEE Aerospace And Electronic Systems Magazine **18** (9): 18-22.

Lee, Y. J., E. K. Lee, et al. (2001). "Effect of potential energy distribution on the melting of clusters." Physical Review Letters **86** (6): 999-1002.

Lee, Y. J., R. M. Nieminen, et al. (2001). "Universal melting behavior of clusters." Computer Physics Communications **142** (1-3): 201-205.

Legrand, S. M. and K. M. Merz (1993). "Rapid approximation to molecular-surface area via the use of boolean logic and look-up tables." Journal of Computational Chemistry **14** (3): 349-352.

Lehtinen, K. E. J., R. S. Windeler, et al. (1996). "A note on the growth of primary particles in agglomerate structures by coalescence." Journal of Colloid and Interface Science **182** (2): 606-608.

Lehtinen, K. E. J. and M. R. Zachariah (2001). "Effect of coalescence energy release on the temporal shape evolution of nanoparticles." Physical Review B **63** (20): art. no.-205402.

Lehtinen, K. E. J. and M. R. Zachariah (2002). "Energy accumulation in nanoparticle collision and coalescence processes." Journal of Aerosol Science **33** (2): 357-368.

Li, Y. L. and T. Ishigaki (2002). "Thermodynamic analysis of nucleation of anatase and rutile from TiO_2 melt." Journal of Crystal Growth **242** (3-4): 511-516.

Lu, H. M., W. X. Zhang, et al. (2003). "Phase stability of nanoanatase." Advanced Engineering Materials **5** (11): 787-788.

Machado, N. and V. S. Santana (2005). "Influence of thermal treatment on the structure and photocatalytic activity of TiO_2-P25." Catalysis Today **107-08**: 595-601.

Martin, S. T., A. T. Lee, et al. (1995). "Chemical mechanism of inorganic oxidants in the TiO_2/UV process: Increased rates of degradation of chlorinated hydrocarbons." Environmental Science & Technology **29** (10): 2567-2573.

Matsui, M. and M. Akaogi (1991). "Molecular dynamics simulation of the structural and physical properties of the four polymorphs of TiO_2." Molecular Simulation **6**: 239-244.

McQuarrie, D. A. and J. D. Simon (1998). Physical Chemistry: A Molecular Approach. Sausalito, University Science Books.

Meyer, A. Y. (1988). "Molecular mechanics and molecular shape. V. On the computation of the bare surface area of molecules." Journal of Computational Chemistry **9** (1): 18-24.

Mostoller, M. and J. C. Wang (1985). "Ionic potential models in insulators having the rutile structure." Physical Review B **32** (10): 6773-86.

Naicker, P. K., P. T. Cummings, et al. (2005). "Characterization of titanium dioxide nanoparticles using molecular dynamics simulations." Journal of Physical Chemistry B **109** (32): 15243-15249.

Nair, J., P. Nair, et al. (1999). "Microstructure and phase transformation behavior of doped nanostructured titania." Materials Research Bulletin **34** (8): 1275-1290.

Navrotsky, A. (2003). "Energetics of nanoparticle oxides: Interplay between surface energy and polymorphism." Geochemical Transactions **4** (6): 34-37.

Oakley, B. A. and D. M. Hanna (2004). "A review of nanobioscience and bioinformatics initiatives in North America." IEEE Transactions On Nanobioscience **3** (1): 74-84.

Ogata, S., H. Iyetomi, et al. (2000). "Role of atomic charge transfer on sintering of TiO_2 nanoparticles: Variable-charge molecular dynamics." Journal of Applied Physics **88** (10): 6011-6015.

Ohtani, B., Y. Okugawa, et al. (1987). "Photocatalytic activity of titania powders suspended in aqueous silver nitrate solution: Correlation with pH-dependent surface structures." Journal of Physical Chemistry **91** (13): 3550-3559.

Oliver, P. M., G. W. Watson, et al. (1997). "Atomistic simulation of the surface structure of the TiO_2 polymorphs rutile and anatase." Journal of Materials Chemistry **7** (3): 563-568.

Ovenstone, J. (2001). "Preparation of novel titania photocatalysts with high activity." Journal of Materials Science **36** (6): 1325-1329.

Panpranot, J., K. Kontapakdee, et al. (2006). "Effect of TiO_2 crystalline phase composition on the physicochemical and catalytic properties of Pd/TiO_2 in selective acetylene hydrogenation." Journal of Physical Chemistry B **110** (15): 8019-8024.

Penn, R. L. and J. F. Banfield (1998). "Oriented attachment and growth, twinning, polytypism, and formation of metastable phases: Insights from nanocrystalline TiO_2." American Mineralogist **83** (9-10): 1077-1082.

Perrot, G., B. Cheng, et al. (1992). "MSEED - A program for the rapid analytical determination of accessible surface-areas and their derivatives." Journal of Computational Chemistry **13** (1): 1-11.

Post, J. E. and C. W. Burnham (1986). "Ionic modeling of mineral structures and energies in the electron gas approximation: TiO_2 polymorphs, quartz, forsterite, diopside." American Mineralogist **71** (1-2): 142-51.

Pratsinis, S. E. (1998-a). "Flame aerosol synthesis of ceramic powders." Progress in Energy and Combustion Science **24** (3): 197-219.

Pratsinis, S. E. and P. T. Spicer (1998-b). "Competition between gas phase and surface oxidation of $TiCl_4$ during synthesis of TiO_2 particles." Chemical Engineering Science **53** (10): 1861-1868.

Predota, M., A. V. Bandura, et al. (2004). "Electric double layer at the rutile (110) surface. 1. Structure of surfaces and interfacial water from molecular dynamics by use of ab initio potentials." Journal of Physical Chemistry B **108** (32): 12049-12060.

Predota, M., Z. Zhang, et al. (2004). "Electric double layer at the rutile (110) surface. 2. Adsorption of ions from molecular dynamics and X-ray experiments." Journal of Physical Chemistry B **108** (32): 12061-12072.

Preining, O. (1998). "The physical nature of very, very small particles and its impact on their behaviour." Journal of Aerosol Science **29** (5-6): 481-495.

Qin, Y. and K. A. Fichthorn (2003). "Molecular-dynamics simulation of forces between nanoparticles in a Lennard-Jones liquid." Journal of Chemical Physics **119** (18): 9745-9754.

Ranade, M. R., A. Navrotsky, et al. (2002). "Energetics of nanocrystalline TiO_2." Proceedings of the National Academy of Sciences of the United States of America **99** (supp. 2): 6476-6481.

Raut, J. S., R. B. Bhagat, et al. (1998). "Sintering of aluminum nanoparticles: A molecular dynamics study." Nanostructured Materials **10** (5): 837-851.

Reck, E. and S. Seymour (2003). "The effect of surface-coated TiO_2 pigments on the performance of paratoluene sulphonic acid-catalysed paint systems." Surface Coatings International Part B-Coatings Transactions **86** (4): 253-258.

Reidy, D. J., J. D. Holmes, et al. (2006). "The critical size mechanism for the anatase to rutile transformation in TiO_2 and doped-TiO_2." Journal of the European Ceramic Society **26** (9): 1527-1534.

Rhee, S. H., J. D. Lee, et al. (2000). "Effect of alpha-Si_3N_3 initial powder size on the microstructural evolution and phase transformation during sintering of Si_3N_4 ceramics." Journal of the European Ceramic Society **20** (11): 1787-1794.

Roux, H. l. and L. Glasser (1997). "Transferable potentials for the Ti-O system." Journal of Materials Chemistry **7** (5): 843-851.

Sahoo, S. K. and V. Labhasetwar (2003). "Nanotech approaches to delivery and imaging drug." Drug Discovery Today **8** (24): 1112-1120.

Sawatari, H., E. Iguchi, et al. (1982). "Formation energies of point defects in rutile (TiO_2)." Journal of Physics and Chemistry of Solids **43** (12): 1147-1155.

Schweigert, I. V., K. E. J. Lehtinen, et al. (2002). "Structure and properties of silica nanoclusters at high temperatures." Physical Review B **65** (23): art. no. 235410.

Siegel, R. W. (1993). "Exploring mesoscopia - The bold new-world of nanostructures." Physics Today **46** (10): 64-68.

Silva, G. A. (2004). "Introduction to nanotechnology and its applications to medicine." Surgical Neurology **61** (3): 216-220.

Smith, W. (1987). "CCP5: a collaborative computational project for the computer simulation of condensed phases." Journal of Molecular Graphics **5** (2): 71-74.

Smith, W. and T. R. Forester (1996). "DL_POLY_2.0: A general-purpose parallel molecular dynamics simulation package." Journal of Molecular Graphics **14** (3): 136-141.

Stark, W. J. and S. E. Pratsinis (2002). "Aerosol flame reactors for manufacture of nanoparticles." Powder Technology **126** (2): 103-108.

Stumm, W. (1992). Chemistry of the Solid-Water Interface, John Wiley & Sons, Inc.

Sun, J., L. Gao, et al. (2003). "Synthesis of nanocrystalline rutile titania by co-thermal hydrolysis of $TiCl_4$ and $TiCl_3$ solutions." Journal of Inorganic Materials **18** (5): 1123-1126.

Sun, J., L. Gao, et al. (2003). "Synthesizing and comparing the photocatalytic properties of high surface area rutile and anatase titania nanoparticles." Journal of the American Ceramic Society **86** (10): 1677-1682.

Suresh, C., V. Biju, et al. (1998). "Anatase to rutile transformation in sol-gel titania by modification of precursor." Polyhedron **17** (18): 3131-3135.

Swamy, V. and J. D. Gale (2000). "Tranferable variable-charge interatomic potential for atomistic simulation of titanium oxide." Physical Review B **62** (9): 5406-5412.

Swamy, V., J. D. Gale, et al. (2001). "Atomistic simulation of the crystal structures and bulk moduli of TiO_2 polymorphs." Journal of Physics and Chemistry of Solids **62**: 887-895.

Trung, T., W. J. Cho, et al. (2003). "Preparation of TiO_2 nanoparticles in glycerol-containing solutions." Materials Letters **57** (18): 2746-2750.

Tsukagoshi, K., N. Yoneya, et al. (2002). "Carbon nanotube devices for nanoelectronics." Physica B-Condensed Matter **323** (1-4): 107-114.

Tsuruta, K., A. Omeltchenko, et al. (1996). "Early stages of sintering of silicon nitride nanoclusters: A molecular-dynamics study on parallel machines." Europhysics Letters **33** (6): 441-446.

Wahi, R. K., W. W. Yu, et al. (2005). "Photodegradation of Congo Red catalyzed by nanosized TiO_2." Journal of Molecular Catalysis A-Chemical **242** (1-2): 48-56.

Wu, M. M., J. B. Long, et al. (1999). "Microemulsion-mediated hydrothermal synthesis and characterization of nanosize rutile and anatase particles." Langmuir **15** (26): 8822-8825.

Xing, Y. and D. E. Rosner (1999). "Prediction of spherule size in gas phase nanoparticle synthesis." Journal of Nanoparticle Research **1** (2): 277-291.

Yang, H. T., G. T. Yang, et al. (1998). "Densification and alpha/beta phase transformation of Si_3N_4 containing MgO and CeO_2 during sintering." Materials Chemistry and Physics **55** (2): 164-166.

Yang, J., S. Mei, et al. (2000). "Hydrothermal synthesis of nanosized titania powders: Influence of peptization and peptizing agents on the crystalline phases and phase transitions." Journal of the American Ceramic Society **83** (6): 1361-1368.

Yang, J., S. Mei, et al. (2001). "Hydrothermal synthesis of nanosized titania powders: Influence of tetraalkyl ammonium hydroxides on particle characteristics." Journal of the American Ceramic Society **84** (8): 1696-1702.

Yang, J., S. Mei, et al. (2001). "Hydrothermal synthesis of TiO_2 nanopowders from tetraalkylammonium hydroxide peptized sols." Materials Science & Engineering C-Biomimetic and Supramolecular Systems **15** (1-2): 183-185.

Yang, J., S. Mei, et al. (2002). "Hydrothermal synthesis of well-dispersed TiO_2 nano-crystals." Journal of Materials Research **17** (9): 2197-2200.

Ye, W. Y., T. F. Cheng, et al. (2003). "Preparation and tribological properties of tetrafluorobenzoic acid-modified TiO_2 nanoparticles as lubricant additives." Materials Science & Engineering A-Structural Materials Properties Microstructure and Processing **359** (1-2): 82-85.

Yin, S., R. X. Li, et al. (2002). "Low temperature synthesis of nanosize rutile titania crystal in liquid media." Materials Chemistry and Physics **75** (1-3): 76-80.

Zachariah, M. R. and M. J. Carrier (1999). "Molecular dynamics computation of gas-phase nanoparticle sintering: A comparison with phenomenological models." Journal of Aerosol Science **30** (9): 1139-1151.

Zachariah, M. R., M. J. Carrier, et al. (1996). "Properties of silicon nanoparticles: A molecular dynamics study." Journal of Physical Chemistry **100** (36): 14856-14864.

Zeng, P., S. Zajac, et al. (1998). "Nanoparticle sintering simulations." Materials Science & Engineering A-Structural Materials Properties Microstructure and Processing **252** (2): 301-306.

Zhang, H. and J. F. Banfield (1998). "Thermodynamic analysis of phase stability of nanocrystalline titania." Journal of Materials Chemistry **8** (9): 2073-2076.

Zhang, H. Z. and J. F. Banfield (2000). "Understanding polymorphic phase transformation behavior during growth of nanocrystalline aggregates: Insights from TiO_2." Journal of Physical Chemistry B **104** (15): 3481-3487.

Zhang, H. Z., B. Gilbert, et al. (2003). "Water-driven structure transformation in nanoparticles at room temperature." Nature **424** (6952): 1025-1029.

Zhang, Z., P. Fenter, et al. (2004). "Ion adsorption at the rutile-water interface: Linking molecular and macroscopic properties." Langmuir **20** (12): 4954-4969.

Zhou, Y., M. Karplus, et al. (2002). "The distance fluctuation criterion for melting: Comparison of square well and Morse potential models for clusters and homopolymers." Journal of Chemical Physics **116** (5): 2323-2329.

Zhou, Y. Q. and M. Karplus (1997). "Folding thermodynamics of a model three-helix-bundle protein." Proceedings of the National Academy of Sciences of the United States of America **94** (26): 14429-14432.

Zhou, Y. Q., M. Karplus, et al. (1997). "Equilibrium thermodynamics of homopolymers and clusters: Molecular dynamics and Monte Carlo simulations of systems with square-well interactions." Journal of Chemical Physics **107** (24): 10691-10708.

Zhou, Y. Q., D. Vitkup, et al. (1999). "Native proteins are surface-molten solids: Application of the Lindemann criterion for the solid versus liquid state." Journal of Molecular Biology **285** (4): 1371-1375.

Zhu, H. L. and R. S. Averback (1995). "Molecular dynamics simulations of densification processes in nanocrystalline materials." Materials Science & Engineering A-Structural Materials Properties Microstructure and Processing **204** (1-2): 96-100.

Zhu, H. L. and R. S. Averback (1996-a). "Sintering processes of two nanoparticles: A study by molecular dynamics." Philosophical Magazine Letters **73** (1): 27-33.

Zhu, H. L. and R. S. Averback (1996-b). "Sintering of nano-particle powders: Simulations and experiments." Materials and Manufacturing Processes **11** (6): 905-923.